1 2 9 0

UNIVERSIDADE Đ
COIMBRA

Mariana Isabel Caria Reis

CHEMICAL COMPOSITION OF SUPER-MASSIVE PLANET HOSTS: THE CLUE TO THEIR FORMATION

VOLUME 1

Dissertação no âmbito do Mestrado em Astrofísica e Intrumentação para o Espaço, orientada pelo Doutor Vardan Adibekyan e pelo Professor Doutor Nuno Santos e pelo Professor Doutor Alexandre Correia e apresentada ao Departamento de Física da Faculdade de Ciências e Tecnologia.

Outubro de 2021

UNIVERSIDADE Đ
COIMBRA

Chemical composition of super-massive planet hosts: the clue to their formation

Mariana Isabel Caria Reis

A thesis submitted for the degree of
Master in Astrophysics and Space Instrumentation

Supervisors:
Dr. Vardan Adibekyan
Prof. Nuno C. Santos
Prof. Alexandre Correia

Departamento de Física
Faculdade de Ciências e Tecnologias
Universidade de Coimbra
October 2021

Resumo

Interligar os processos físicos dos planetas e das suas estrelas pode revelar detalhes essenciais sobre as condições ambientais da formação dos planetas. Existe uma relação conhecida entre a ocorrência de planetas gigantes e a metalicidade das suas estrelas, favorecendo a formação destes planetas pelo modelo de "acreção do núcleo" (core-accretion). No entanto, alguns trabalhos recentes sugeriram que pode haver uma quebra na massa planetária em cerca de 4 massas de Júpiter a cima e abaixo da qual os canais de formação planetária são diferentes: os planetas tipo Júpiter formam-se via "acreção do núcleo", enquanto que os planetas super-massivos formam-se por "instabilidade gravitacional". O argumento-chave para tal conclusão é que os planetas super-massivos foram maioritariamente detectados em volta de estrelas pouco metálicas, o que contradiz a previsão da teoria de "acreção do núcleo".

Uma limitação importante dos trabalhos mencionados é usarem a abundância do ferro como uma aproximação da metalicidade global, o que pode ser pouco preciso para estrelas com pouco ferro. Isto é maioritariamente porque estrelas hospedeiras com pouco ferro têm mostrado estar enriquecidas noutros metais o que pode compensar pela falta de ferro nestas estrelas.

Realizámos uma análise espectroscópica detalhada de 113 FGK estrelas hospedeiras de 96 planetas com massas abaixo de 4 M_{jup} e 39 planetas com massas superiores a 4 M_{jup} para determinar as abundâncias dos metais (C, O, Mg e Si) importantes para a formação de exoplanetas. De seguida, um modelo estequiométrico foi usado para estimar a soma da percentagem de massa de metais (Z) no disco protoplanetário onde os planetas foram formados. Adicionalmente, usámos a massa das estrelas hospedeiras como uma aproximação para o disco protoplanetário e ao multiplicá-la com o Z estimámos a quantidade total de metais no disco relevantes para a formação de planetas massivos. Ao realizar um teste de Kolmogorov-Smirnov mostrámos que os sistemas com planetas gigantes e super-gigantes têm distribuições semelhantes de $Z \times M_\star$ o que sugere um mecanismo de formação comum para as duas populações de planetas. Adicionalmente, encontramos que o Z é significativamente maior em sistemas com qualquer tipo de planeta gigante quando comparado com estrelas sem planetas detectados. Este resultado leva-nos a sugerir que o mecanismo de formação mais provável para a formação de planetas massivos e super-massivos é a "acreção do núcleo".

Abstract

Linking the physical properties of planets and their host stars can reveal essential details about the environmental conditions for planet formation. There is a known relationship between giant planets occurrence and metallicity of their host stars, which favors the formation of these planets via so called core-accretion model. However, some recent works suggested that there might be a planetary mass breakpoint at about 4 Jupiter masses above and below which planet formation channels are different: the Jupiter-like planets form via core-accretion, while the super-massive planets form through gravitational instability. The key argument for such a conclusion is that super-massive planets are mostly detected around metal-poor stars, which goes against the predictions of core-accretion theory.

An important limitations of the aforementioned works is that iron abundance was used as a proxy for overall metallicity, which might be inaccurate for stars with low iron content. This is mostly because iron-poor planet host stars have been shown to be enhanced in other metals which could compensate for the lack of iron in these stars.

We performed a detailed spectroscopic analysis of 113 FGK-type stars hosting 96 planets with masses below 4 M_{jup} and 39 planet with masses above 4 M_{jup} to determine the abundances of the metals (C, O, Mg, and Si) important for exoplanet formation. A stoichiometric model was then used to estimate the summed mass percentage of metals (Z) in the protoplanetary discs where these planets formed. Additionally we used the mass of the host stars as a proxy for protoplanetary disk and by multiplying it with Z we estimated the total amount of metals in the disk relevant for the formation of massive planets. By performing a Kolmogorov–Smirnov test we showed that the systems with giant and super-giant planets have similar distributions of $Z \times M_\star$ which suggest a common formation mechanism for the two populations of planets. Additionally, we found that Z is significantly larger in systems with any type of giant planets when compared with stars without detected planets. This result led us to suggest that the most probable mechanism for the formation of massive and super-massive planets is core-accretion.

Acknowledgments

First, I would like to express my gratitude to my supervisors Dr. Vardan Adibekyan, Prof. Dr. Nuno Santos and Prof. Dr. Alexandre Correia for the opportunity to work in this project and dwell in this fascinating area of study. I would also like to acknowledge and give my warmest thanks to Dr. Vardan Adibekyan who made this work possible and whose guidance and advice carried me throughout all the stages of executing and writing this project.

To everybody in IA planetary group that showed interest in this work, with special regards to Dr. Sergio Sousa, Dr. Elisa Delgado Mena and my colleague Barbara Soares.

I would like to deeply thank my parents for encouraging me in my chosen course, despite not completely understanding my area of study. Also for their incredible supporte in me changing cities for my Master's degree, and overall for believing in me throughout my whole life.

A massive thanks to my best friends, Joana, Mariana and Ana for being one of my main sources of emotional support in the last few years.

To Ginpong squad and my friends in BIF for supporting me and giving me a great academic life filled with so many good times and adventures together.

I'd like to acknowledge all the people that came into my life and shaped me into who I am today, specifically everyone who made my academic life so full of fun experiences.

And finally I'd like to thank my cats, Biscoito and Pudim, for staying by my side throughout the quarantines, unintentionally appearing in meetings and overall keeping me company and bringing me so much joy and cuddles in the past few years.

Index

List of Figures

List of Tables

Abbreviations

RV - Radial velocity
BD - Brown Dwarfs
CA - Core-accretion
GI - Gravitational instability
TD - Tidal downsizing
KDE - Kernel Density Estimate
SNR - Signal-to-noise ratio
LTE - Local Thermodynamical Equilibrium
NLTE - non Local Thermodynamical Equilibrium
EW - Equivalength width
HARPS - High Accuracy Radial velocity Planet Searcher
HR - Hertzsprung-Russell
FWHM - Full width at half maximum
ML - Machine Learning
AI - Artificial intelligence
RF - Random forest
APOGEE - Apache Point Observatory Galactic Evolution Experiment
RGB - red-giant branch
$\boldsymbol{R^2}$ - coefficient of determination
$\boldsymbol{f_{iron}}$ - Iron-to-silicate mass fraction
$\boldsymbol{w_f}$ - Water mass fraction
$\boldsymbol{Z}$ - summed mass percentage of all heavy elements expected for the planetary building blocks
KS - Kolmogov-Smirkov
HSWNP - Harps Stars With No Planets

Chapter 1

Introduction

An exoplanet, which is short for extrasolar planet, is a planet that orbits a star other than the Sun. Most exoplanets orbit a star, but there have been detected free floating massive exoplanets, which are usually called rogue planet (Rebolo et al., 2000). The first exoplanet orbiting around a solar-type star was discovered in 1995 (Mayor and Queloz, 1995). This object had about half the mass of Jupiter and an orbital period of 4 days, surrounding a solar type star, 51 Pegasi (Mayor and Queloz, 1995). The companion of the 51 Peg was not predicted by any of the giant planet models of the time, and its detection prompt the search of diversity in planetary formation sites. This finding was significant enough to earn the authors a Nobel Prize in 2019, and it sparked a whole new field of research in astrophysics: the study of exoplanets, which includes numerous branches ranging from detection to characterisation.

1.1 Exoplanet detection methods

As of April 2021, there are 4718 planets discovered (3489 planetary systems and 772 multiple planet systems) and 2489 candidates awaiting for validation (Schneider et al., 2011)[1]. There are several methods of detecting exoplanets. Detecting exoplanet via direct observations is very difficult, as such the majority of the planets have been detected via indirect methods.

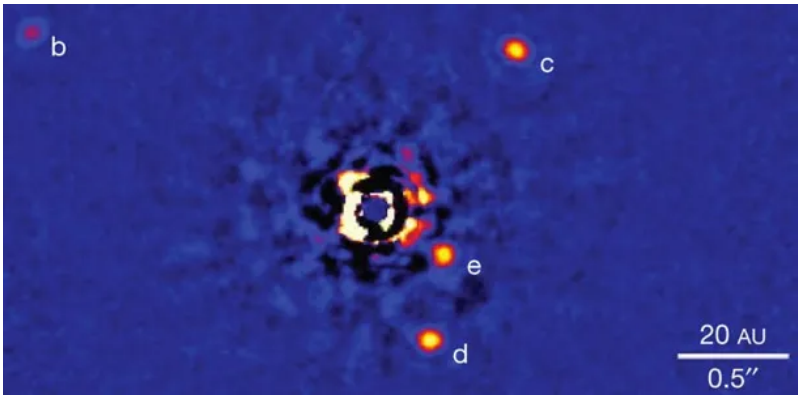

Figure 1.1: Direct imaging exoplanets detections surrounding HR8799 obtained with Hale telescope. SOURCE: Marois et al. (2010)

An example of direct method is imaging, which corresponds to blocking the light from the star, using coronagraphs, leaving the planet visible, in order to try and get an image of

---

[1] `http://exoplanet.eu/`

the planet's own light source, by thermal emission. The difficulty in this method is that the exoplanet hosts are million of times brighter than their planet, and given their small size and dim light, exoplanets are easily lost in its stellar glare (Wright and Gaudi, 2013). This method is more efficient in finding giant exoplanets with wide orbits surrounding faint stars, but overall this technique is not very effective in detecting exoplanets. An example of exoplanets found through this method are the planets detected around the star HR8799, figure 1.1.

One of the most used indirect method is the Doppler Radial Velocity (RV) method.

Stars and planets move in regard to a common center of mass. The star's 'wobble' movement and velocity varies in consequence to the planet's mass and proximity to the star (Wright, 2018). The RV method measures the displacement of the star's spectral lines due to the Doppler effect, enabling the possibility to confirm the presence of a planet or system and some of its characteristics, for instance the planets minimum mass (Lindegren and Dravins, 2003). A visual representation of the method is shown in figure 1.2, where we see the movement and respective spectra received by ground-based spectrographs on Earth.

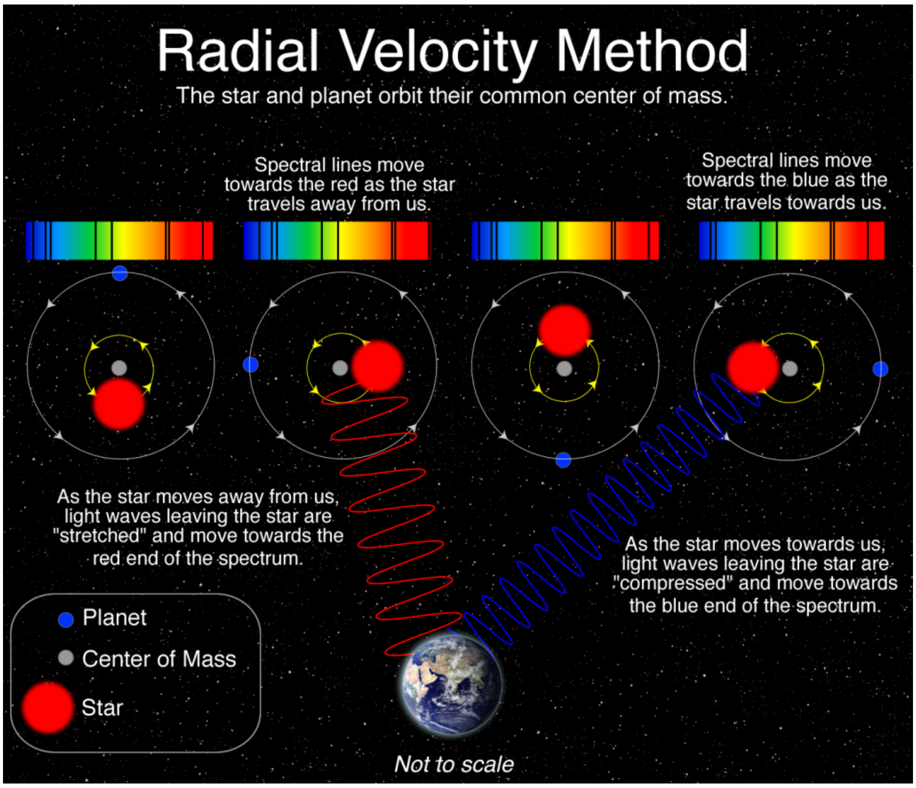

Figure 1.2: Radial velocity method diagram. SOURCE: Las Cumbres Observatory

Another widely used and efficient indirect method is the so called Transiting method. A transit occurs when a celestial body passes in between a larger stellar object and the observer. As the planet passes in front of the star, the light curve will show a dip in brightness, dependent on the size of the star and planet (see Figure 1.3). This method is only possible when the Earth, the planet and the star are in near-perfect alignment, as the angle of the orbital planet can have a few degrees and still get detected (Henry et al., 2000), which makes the probability of seeing a planet in this condition low. Observing a transiting planet makes it possible to obtain some parameters of the planet, such as the radius of the planet and if for instance there is information of the full transit, the orbital period (Charbonneau et al., 2000).

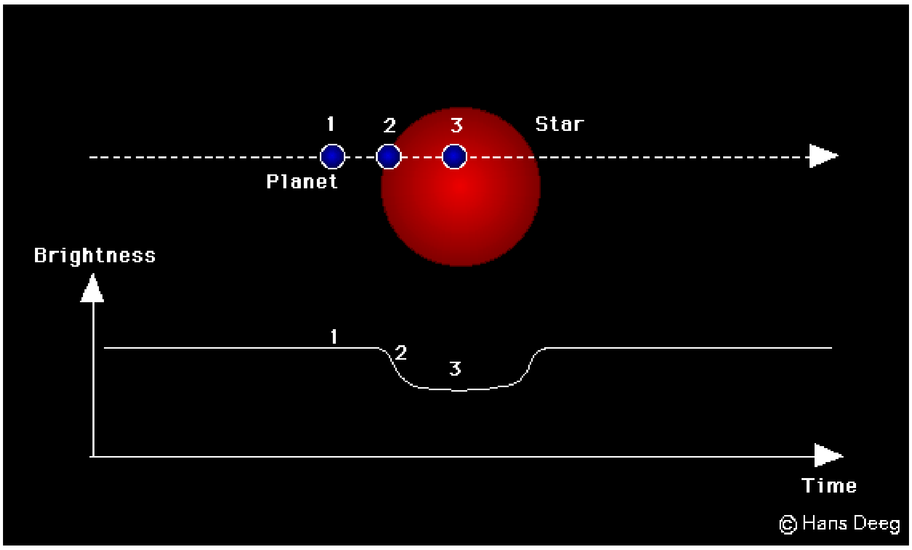

Figure 1.3: Representation of a transiting exoplanet and the respective light curve. SOURCE: Deeg and Garrido (2002)

Another detection method worth mentioning is the Astrometric method. While the number of exoplanets detected via astrometry - which consists in the measurements of the positional change of the star due to the gravity of exoplanet (see Figure 1.4) - is not large, the GAIA mission (Gaia Collaboration et al., 2016) is expected to detect thousands exoplanets with this method (Perryman et al., 2014). This technique requires a high level of precision in order to obtain accurate parallax measurements, which is extremely difficult to obtain from the ground, making this mission necessary to detect exoplanet in this means.

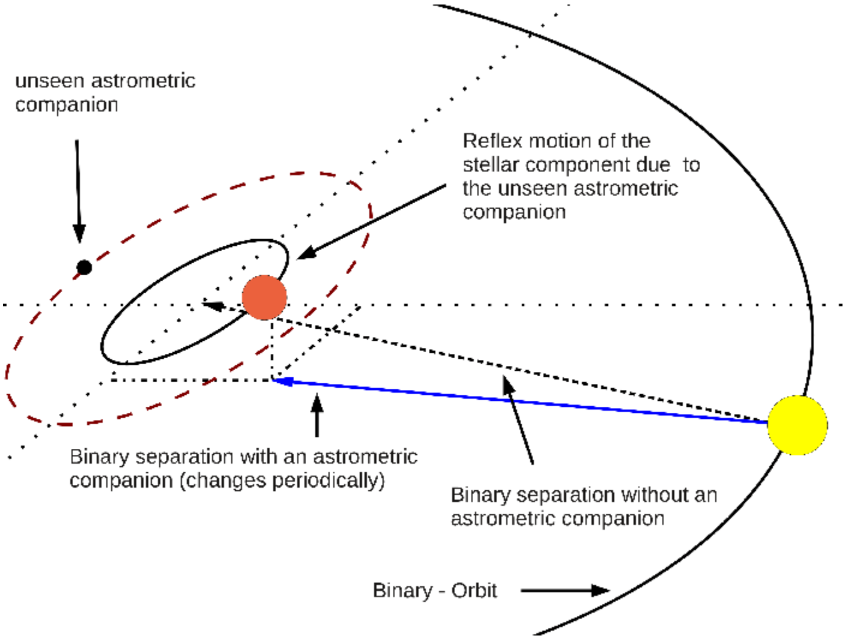

Figure 1.4: Schematic of how the astrometric detection method works. SOURCE: Astrophysical Institute and University Observatory

There are several other methods for detecting exoplanets, but the RV and Transiting methods correspond to the majority of exoplanets detection methods discovered until today.

In figure 1.5 there are two visual representation of the exoplanets discovered up until 2021 and their respective detection method, per year (left panel) and in mass-period diagram (right panel).

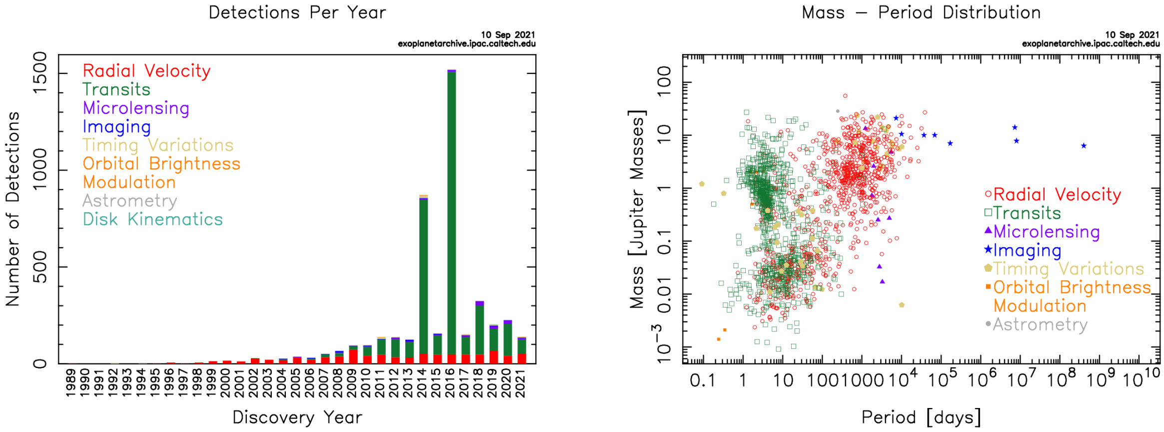

Figure 1.5: LEFT PANEL: Histogram with the number of exoplanets detections per year differentiated by each detection technique. RIGHT PANEL: Mass-period diagram of the exoplanets discovered specified by each detection method. SOURCE: Pre-generated exoplanet plots from the NASA exoplanet archive.

From the left panel of Figure 1.5 we notice a clear effectiveness toward transits and radial velocity detection methods for the discovery of most exoplanets, until now. The mass-period diagram (right panel) contains valuable clues about the formation and evolution processes of the detected planets, despite the figure having selection effects and observational biases. From that diagram we can see that the planets are clustered in three main clusters: hot super-Earths (planets with low masses and short periods), the Hot-Jupiters (planets with high mass and short period) and ice giants, (massive planets with long orbital periods). We can also notice a lack of giants planets in between hot-Jupiter and ice giants with periods ranging from 10 to 100 days. The gap in the Mass-Period diagram is called 'Period Valley', the origin of which is thought to be related with disk migration of relatively massive planets (Udry et al., 2003) or selection effects (Wittenmyer et al., 2010).

1.1.1 Characterization of exoplanets

One of the main characteristics of planets is their mass. If the host mass is known, the Radial Velocity method allows to determine $M \sin i$ i.e. the minimum mass of the planet. In the case of transiting planets, the orbital inclination (i) of the system can be estimated which together with the RV measurements allows to determine the true mass (Cumming et al., 2008). Unfortunately, the number of planets with both RV and transiting observations is not large, and for most of the so far detected planets only the minimum mass is available. The true mass of planets can also be determined for multi-planetary systems with the so called Transit Timing Variation technique (e.g. Nesvorný and Morbidelli, 2008). However, the number of such systems is not large as well.

The radius is another very relevant propriety of exoplanets. As previously mentioned, when the planet is discovered through transits methods, the planet radius can be measured from the dip in brightness seen in the light curve. The dip is proportional to the star to planet radius ratio. If the radius of the host star is known, the planetary radius can be determined from the light curves.

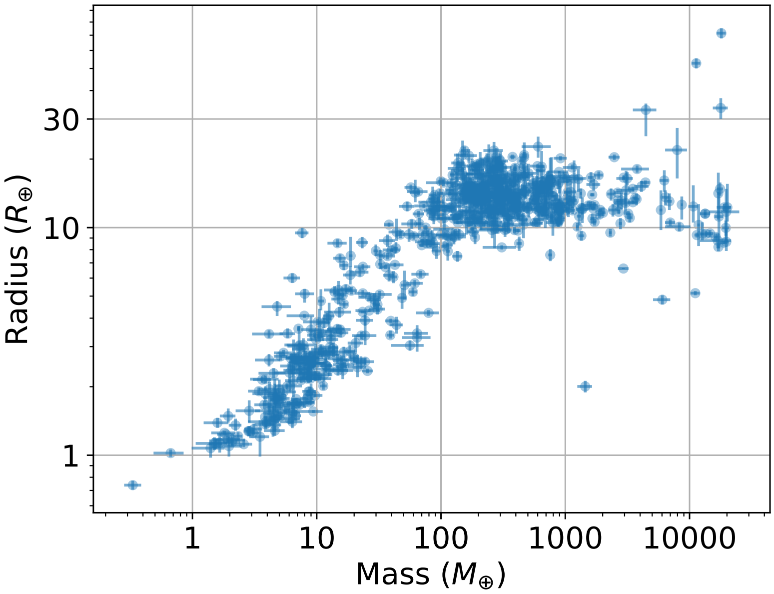

Figure 1.6: A mass-radius diagram of the discovered exoplanets from exoplanet.eu database with the mass and radius determination better than 30%.

The mass-radius relation displayed on Figure 1.6 shows two different behaviours, up until around 100 $M_\oplus$, the mass and radius increase more or less in proportion with each other. On the other hand, from 100 $M_\oplus$ on we notice that the radius stays mainly constant despite the mass growth. In other words, we notice a transition mass where there is a change in the functional form of the mass-radius relation.

Different works adopt different mass limit to group exoplanets (e.g. Russell, 2013). We refer the reader to Russell (2021) for an interesting discussion about the categorization of planets by their composition. However, in most cases planets are grouped into low mass planets, giant planets, and super-massive planets. The low mass planets are the planets with Earth-like compositions (sometimes called super-Earths) or planets similar to Neptune in mass. The giant planets are the large ones predominantly made of gas or ice and have masses of around the Jupiter mass. Finally, the super-massive ones are the planets with mass significantly higher than Jupiter, but are less massive than 13 M_{jup} which is the lower mass limit for Brown Dwarfs (BD) (e.g. Saumon et al., 1996). Interestingly, the occurrence rate of these three groups of planets show different dependences on the metallicity of their host stars (e.g. Adibekyan, 2019).

Besides their mass and radius, there are many other properties that characterize exoplanets, for instance, the eccentricity, the orbital period, the semi-major axis. All of this properties together provide valuable information about the exoplanet itself and the system. The exoplanet community, in particular exoplanet formation modelers are aimed at reproducing the aforementioned statistical properties of planets.

1.1.2 Planet formation scenarios

Exoplanet research is fairly recent. The recent advancement of exoplanet-detecting technology allowed for the detection of a much greater diversity (Figure 1.5 and 1.6) of exoplanet properties than was previously expected. These discoveries prompted the need to revise and improve planet formation theories. There are two main theories proposed to explain the formation of exoplanets: core-accretion (CA) and gravitational instability (GI).

1.1.2.1 Core-Accretion

In the classical core-accretion paradigm, low-mass planets and cores of massive planets are formed from the accretion of solid planetesimals (Pollack et al., 1996). This planetesimals are made by the sedimentation and coagulation of small dust grains in the protoplanetary disks (Wetherill and Stewart, 1989; Lissauer, 1993). In the core-accretion scenario, if a protoplanet acquires enough solid mass to be able to undergo runaway accretion of gas while the protoplanetary disk is still not dissipated, then a giant plant is formed. If the protoplanet grows slowly, it will not have enough time to accrete gas and will remain a low-mass rocky planet. This critical mass for the cores of giant planets is about 5-10 $M_{\oplus}$ (Ikoma et al., 2000; Mordasini et al., 2014; Hasegawa and Pudritz, 2014), at this point the pressure gradient in the atmosphere of the planet cannot hold its own gravity and collapses (Ida and Lin, 2004a). Then the core suffers accretion of disk gas and giant planets are formed. Gas accretion is a relatively quick process and can happen before the gas in the disk is depleted, either globally or locally (Ida and Lin, 2004a). The protoplanetary disk lifetime is of 1-10 Myr, which is about the same as the estimated timescale of giant planet formation in this scenario (Alibert et al., 2005). The timescale is therefore a potential issue for this theory, where the formation of the core is what conditions such high timeline. In the core-accretion models, the formation efficiency of giant planets depends on the metallicity of the protoplanetary disk. This is because the higher the amount of dust particles (metals) in the disk, the faster the growth of the cores to reach the critical mass for giant planet formation. The lack of planets observed in Figure 1.6 with masses between 10-100 $M_{\oplus}$, 'planetary desert', is explained in this theory. Since the runaway gas accretion is relatively quick, planets that reach the critical mass of about 10 $M_{\oplus}$ very quickly increase their masses to greater than 100 $M_{\oplus}$ (Ida and Lin, 2004a). The recent core-accretion models also take into consideration the migration of planets in the disks and the formation of gaps (Mordasini et al., 2012).

1.1.2.2 Gravitational Instability

Gravitational instability being thought to have a contribution for the formation of massive planets, was first introduced by (Kuiper, 1951). In this theory, the stellar disk had to be massive and cool enough to become gravitational unstable (Boss, 1998). The instabilities lead to the formation of self-gravitating clumps of gas and dust (Boss, 1998). This process of disk fragmentation is fast and can operate even in short-lived disks (Boss, 1998). It was thought that gravitational instability in more metallic environments could actually "suffocate" the growth of the planet formation clumps (Boss, 2002). The reason for this being that the higher metallicity implies higher optical depths, more efficiency at capturing radiation, and consequently higher temperature (Boss, 2002). However the results of Boss (2002) do not show a dependence on the stellar metallicity.

Tidal Downsizing (TD) (e.g., Nayakshin et al., 2011; Nayakshin, 2014) is a variation of the classical gravitational instability model with some elements (e.g. disk migration) traditionally used in the CA models. Per TD the clumps of gas formed in the outer region of the disk by gravitational fragmentation, migrate inward, accumulating solid cores in their interior (Vorobyov and Elbakyan, 2018). As they migrate, they start losing some or even all of its gas atmosphere and overall mass due to stellar tidal torque (Vorobyov and Elbakyan, 2018). The final output of this process depends on many factor and can lead to the formation a giant planet, an ice planet or even a terrestrial planet (Nayakshin, 2017).

The CA model of Mordasini et al. (2012) and the TD/GI model of Nayakshin (2016) are already able to reproduce many observed properties of the detected exoplanets. However, current exoplanet formation hypotheses still leave a lot of issues unresolved.

1.2 Exoplanet host stars and their metallicities

Planets and their host stars are formed in the same molecular clouds, therefore many of their properties are related to the environmental properties where they are formed. An example of this being the chemical composition of some mineralogical abundance ratios, for instance the [Fe/Si] or [Mg/Si] that are expected to be similar in rocky planets and their host stars (Bond et al., 2010; Thiabaud et al., 2014; Dorn et al., 2015). Studying and characterizing the planet host stars allows for the characterization of the planets (Adibekyan et al., 2018) as well as provides information about their formation and evolution (Mayor et al., 2014).

Based only on a sample of a few giant planets, Gonzalez (1997) found that these planets are mostly orbiting around metal-rich stars. Now known as the giant planet - metallicity correlation (e.g., Santos et al., 2001, 2004; Fischer and Valenti, 2005; Johnson et al., 2010; Sousa et al., 2011; Buchhave et al., 2012; Mortier et al., 2013). This correlation is important because it shows a intimately relation between the frequency of giant planets and metallicity which is apparently not the case for low-mass planets (see Figure 1.8) (e.g. Sousa et al., 2011)

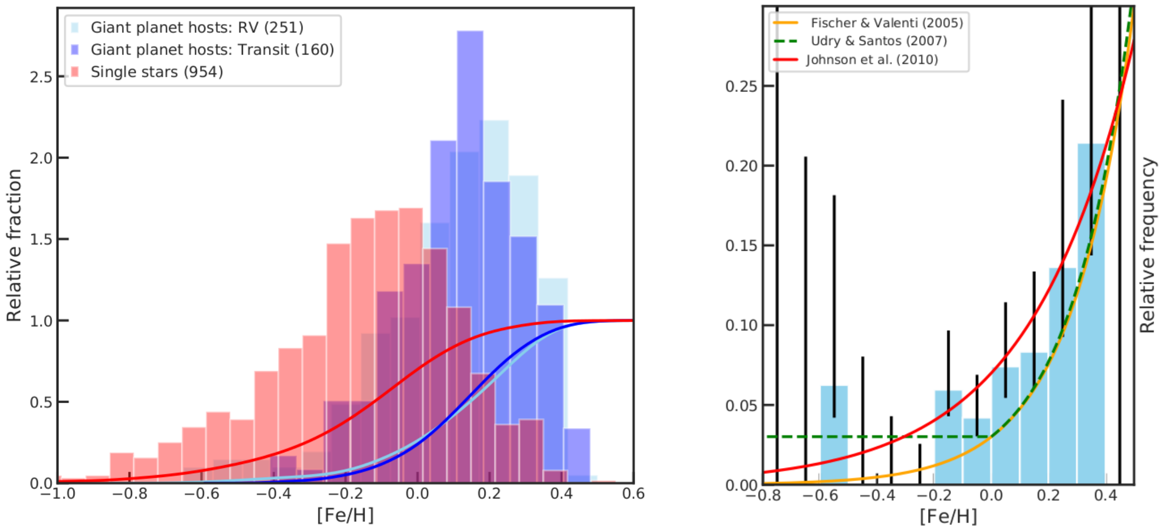

Figure 1.7: LEFT PANEL: metallicity distribution of giant planet hosts detected by RV (light blue) and Transit methods (dark blue) and stars with no planets (red) with the respective KDE fits of the cumulative distribution of the metallicities. RIGHT PANEL: Giant planet frequency dependence on the stellar metallicity with different functional forms of planet occurrence - metallicity relation. SOURCE: Adibekyan (2019)

The left panel of Figure 1.7 shows the metallicity distribution of giant planet hosts detected through transit (dark blue) and RV (light blue) planet detection methods and stars with no planets (red). This graph clearly shows that stars with no planets are on average less metallic than host of giants planets. Another interesting factor is that the different detection method do not affect the metallicity relation. The right panel shows the dependence of giant planets with the stellar metallicities with the functional form of the planet occurrence and metallicity of different works (Fischer and Valenti, 2005; Udry and Santos, 2007; Johnson et al., 2010).

The figure shows a clear exponential increase of giant planet frequency with metallicity for stars with metallicities above about -0.2 dex. Bellow that metallicity there is still a question on the metallicity - planet occurrence functional form, being it constant or exponential.

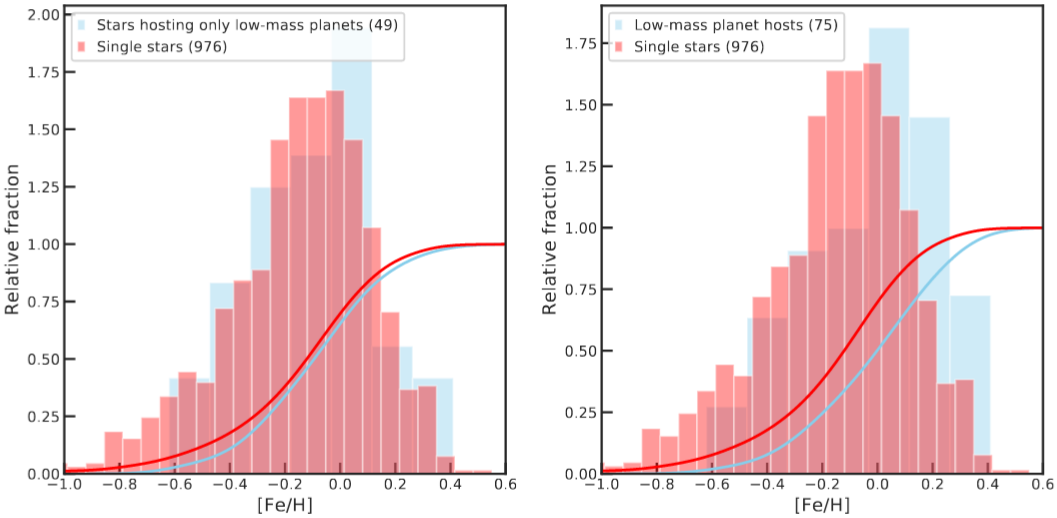

Figure 1.8: Metallicity distribution of low-mass planet hosts stars (light blue) and stars with no planets (red) with the respective KDE fits of the cumulative distribution of the metallicities. On the left panel there is only represented the stars that host only low-mass planet, on the right panel all hosts with low-mass planets. SOURCE: Adibekyan (2019)

On the Figure 1.8, there are two similar plots that show the fraction of low-mass planets hosts with metallicity. On the left panel, there are only plotted stars that only host low-mass planets and field stars (star without planets) and we notice that there is not a statistically difference between their metallicities. On the right panel, it is also included hosts that have bigger mass planets, and now we notice a slighter higher average metallicity when compared to the field stars. These plots reinforce that the giant planet occurrence and metallicity relation does not appear to hold for low-mass planets hosts.

There have been two main hypothesis to explain the origin of the metal excess in massive planet hosts. The first one being the *self-enrichment scenario*, also know as pollution (e.g., Murray et al., 2001), where the material from outside the disk is sweep into it polluting the outer convective envelope of the star (Gonzalez, 1997). The cause for this possibly being that during the inward migration of giant planet, the metal-rich material was dragged along. The second, and currently accepted scenario is *primordial origin* (e.g., Santos et al., 2004), where the high metallicity in the host stars simply implies a higher efficiency of giant planet formation.

The aforementioned correlation between metallicity and giant planet occurrence rate suggests that the core accretion hypothesis is the most likely explanation for the planets discovered.

1.3 Characterization of planet host stars

To analyse the stellar properties of a star, from getting the stellar parameters to attaining its chemical composition, one can make use of spectroscopic methods. The physical processes behind and a spectroscopic procedure are explained further in this section.

1.3.1 Spectroscopic methods of determining stellar parameters and abundances

In order to obtain the chemical composition of a star with a spectroscopic analysis there is a need to establish some basic principles first. Stellar parameters or chemical abundances are obtained from the examination of the absorption lines of the relevant chemical elements in the stellar spectrum. Absorption lines are the result of bound-bound transitions between discrete energy levels in atoms and molecules, which absorb photons with a defined energy therefore decreasing the intensity of the radiation field (blocking the light) at specific wavelengths (Allende Prieto, 2016). Chemical abundances are influenced by line formation and stellar atmosphere, given the two are tightly bound. Spectral lines influence the atmosphere structure by blocking and redistributing the radiation, and in contrast the atmosphere structure is what controls the properties (shape and strength) of the spectral lines (Allende Prieto, 2016).

In order to acquire precise stellar parameters and abundances from the measurement of absorption lines, high resolution spectra and high SNR (signal-to-noise ratio) are required. One of the reasons being that with high resolution, the instrumental broadening of the lines is less prominent from other widening effects, allowing for the disentangling of blending lines and better placement of the continuum (Nissen and Gustafsson, 2018). The strength of the absorption lines is impacted by the temperature and pressure. At the same time, for a given temperature and pressure, the strength of a unsaturated line is proportional to the number of absorbers. Therefore by measuring unsaturated absorption lines, we can reckon the column number density of the absorber, which is what caused the line to be formed in the first place (Allende Prieto, 2016). Thus the aim is to derive the number of absorbing atoms responsible for a given line in order to then be able to compute the total abundance of such element (Allende Prieto, 2016).

In deep layers, stellar atmospheres are optically thick, where Local Thermodynamic Equilibrium (LTE) holds, which allows to know the radiation field from the gas temperature (Allende Prieto, 2016). In LTE it is assumed that each volume element is thermally at equilibrium at a certain temperature Teff. However, the volume elements are not closed systems, since there are photon interactions, but as long as the photon absorption does not disrupt the equilibrium, LTE remains valid. In LTE each upward transition and radiative excitation and ionization, has the opposite process taking place at the same rate, to achieve equilibrium, also known as detailed balance (Allende Prieto, 2016). Under LTE, the stellar line strength and shape, that depends on the thermodynamic structure, influences the ionization and excitation of the atoms and molecules, as well as the thermal and collisional broadening (Allende Prieto, 2016).

In order to evaluate the radiation field, one has to calculate the radiative transfer and determine its role in the energy balance, this being crucial for computing model atmospheres (Allende Prieto, 2016). The most widely used types of model of atmospheres are the 1D-LTE models. The more realistic models - the 3D-nLTE (non-LTE, departures from LTE) models - are being developed recently. 1D models of atmospheres can have a plane-parallel or spherical geometry for each layer of the atmosphere (Jofré et al., 2019). NLTE models are especially relevant to use when working with hot or metal-poor stars, in order to acquire accurate results.

Given that matter and radiation are coupled locally in LTE, the level population of a given element in LTE may be easily calculated from the local gas temperature using Boltzmann and Saha distributions, which considerably simplifies the matter (Asplund, 2005).

1.3.1.1 Determination of stellar parameters and abundances

There are two primary approaches that are often employed to obtain spectroscopic stellar parameters. The first one called *spectral synthesis method*, in which a synthetic theoretical spectra is produced and compared against the observed spectrum, where the best fit determines the final parameters. The second technique is the *Equivalent Width (EW) method*, which is based on a line-by-line analyses of the observed spectra. In the later method, the EW of spectral lines are measured and converted into abundances. In this work, we used the ARES[2] tool (Sousa et al., 2007a), more specifically ARES v2 (Sousa et al., 2015) to measure the EWs of the spectral lines automatically. ARES stands for Automatic Routine for line Equivalent widths in stellar Spectra (Sousa et al., 2007b; Sousa, 2014; Sousa and Andreasen, 2018).

The EW method is only viable in the case that the individual lines can be accurately isolated otherwise the results may be unreliable for those lines. ARES recent version (ARES v2) takes into account the radial velocity (RV) correction, so it is not necessary for the user to correct the RV of the spectra beforehand (Sousa et al., 2015). Another advantage of ARES is the automatic parameterization of the continuum level which is relevant in order to get consistent and reliable results. For the measurements of the EW, the definition of the profile function to better fit the lines takes into account the strength of the line. A Gaussian profile fits better weak absorption lines, however with stronger lines it is usually preferred a Lorentzian profile or even a Voigt profile, but these latter type lines should be avoided (Sousa, 2014; Nissen and Gustafsson, 2018). ARES employs a Gaussian fit to the spectral lines (Sousa et al., 2015), which are latter studied with a radiative transfer calculation and a model of atmospheres as described in Jofré et al. (2019).

Iron is a very important element which has many lines and high abundance in solar-type stars (Nissen and Gustafsson, 2018). Using the EW method on the Fe lines allows to obtain the stellar parameters, which are the effective temperature (Teff), surface gravity ($\log g$), and metallicity ([Fe/H]). For 1D plane-parallel model of atmosphere, there is the need to account for the micro-turbulence (v_{tur}) of the stellar atmosphere, specially when using partially saturated lines (Nissen and Gustafsson, 2018). The reason for this being that this small scale turbulence motion of particles can induce excessive line broadening (Jofré et al., 2019).

The EW measurement obtained from ARES are transformed into individual line abundances with the use of a radiative transfer code MOOG[3] (Sneden, 1973). MOOG makes use of stellar atmospheric models that can assume or not an LTE approximation. MARCS models[4] (Gustafsson et al., 2008) and ATLAS9[5] (Kurucz, 1993) are the two primary 1D atmospheric models that consider LTE approximation. For this work, we made use of MARCS model, which is a 1D grid of hydrostatic, plane-parallel and spherical LTE model atmosphere.

To acquire the final parameters, there is the need look into the atomic data of the spectral lines. The choice of the lines and the respective parameters to use, can heavily influence the result. When doing the line selection for each element, it is wise to select lines that have different wavelengths and excitation potentials spread in a wide range of the spectrum, as well as lines in different ionization stages (Jofré et al., 2019). The line list consists of EWs, the

---

[2] `https://github.com/sousasag/ARES`

[3] `https://www.as.utexas.edu/~chris/moog.html`

[4] `https://marcs.astro.uu.se/`

[5] `https://www.stsci.edu/hst/instrumentation/reference-data-for-calibration-and-tools/astronomical-catalogs/kurucz-1993-models`

excitation potential (E.P.) and the oscillator strengths ($\log gf$), which are necessary for MOOG to calculate the individual line abundances. The oscillator strengths are hard to accurately constraint, consequently, its uncertainty can propagate and heavily influence the precision of the spectroscopic parameters and/or abundances derived (Sousa, 2014). The use of a differential analysis approach can assist in overcoming the $\log gf$ uncertainties. This method compares stars of similar kind with well-known parameters, for FGK dwarfs stars it is usually the Sun, and recomputes the $\log gf$ using an inverse analyses (Sousa, 2014). When done correctly, this method decreases atomic parameters and EW measurement errors, but, when the stars diverge from the benchmark star, the results degrade (Sousa, 2014).

Getting the stellar parameters from the EW method is an iterative process where each parameter is adapted until there is reached an excitation and ionization balance and there are no correlation present. This process can be made automatic by using a proper minimization method. The iteration starts with a model of atmospheres being formed with semi-arbitrary stellar parameters, from which, together with the EW measurements of the Fe lines, MOOG computes them to get the individual lines abundances. If ionization and excitation balance is not reach, the loop continues with new input parameters being chosen in relation to the MOOG output. The final Teff is chosen in a way to not have the iron abundance being dependent on the excitation potential, while the $\log g$ is chosen so that there is agreement between the FeI and FeII lines (Nissen and Gustafsson, 2018). $\log g$ has a smaller effect on the spectrum when compared to the Teff, which makes it more difficult to constraint spectroscopically, however it can be obtained through other methods if needed (Jofré et al., 2019). The v_{tur} is related with the saturation of the stronger iron lines (Sousa, 2014), and is derived in such a way that the iron abundance is independent of the line strength (Jofré et al., 2019). When excitation and ionization balance is achieved, the final input parameters used for the model of atmosphere correspond to the final stellar parameters for the star. For more details with an example and explanation on how to change each parameter to achieve the final stellar parameter I refer the reader to the practical example of Sousa (2014).

The approach to get the final abundance is simpler than the one used to calculate the stellar parameters as no iteration loop is needed. The line list contains information about the spectral lines of the selected elements. The model of atmosphere is calculated with the stellar parameters that have to be previously determined. Based on the input parameters (line-list and model of atmospheres) the abundances of the individual elements can be determined by using MOOG. In case of elements with several spectral lines, the average abundance is usually considered.

1.3.2 Metallicity in astronomy

In astronomy the term 'metallicity' is widely used, for instance, in a star composition a 'metal' is any element that is not hydrogen or helium. To be precise, metallicity corresponds to the mass fraction of all metals heavier than helium, Z (McWilliam, 1997).

Because the atomic abundances of diverse metals in stars differs by several orders of magnitude, a logarithmic scale is more convenient to depict. Atomic abundances are usually defined in terms of H, which is set as $\log \epsilon(H) \equiv 12$. This implies that the atomic abundance of a certain element M is 1.1 where the M and H represent the number of atoms of a certain element M and hydrogen, respectively.

$$\log(\epsilon(M)) = \log_{10}(M/H) + 12 \tag{1.1}$$

Considering X and Z the mass fraction of hydrogen and metals, respectively, the metallicity of a given star $[m/H]$ can be determined using equation (1.2), which by definition is calculated in regards to the solar's metallicity.

$$[m/H] = \log\left(\frac{Z}{X}\right)_\star - \log\left(\frac{Z}{X}\right)_\odot \tag{1.2}$$

Deriving the atomic abundances of all metals for a given star is very difficult, because such data is not available for all elements. Therefore in stellar astrophysics, the iron content [Fe/H] is used as a proxy of the overall metallicity, equation 1.3.

$$[m/H] = [Fe/H] = \log\left(\frac{Fe}{H}\right)_\star - \log\left(\frac{Fe}{H}\right)_\odot \tag{1.3}$$

Iron is used because solar-type stars present multiple strong iron lines making it easier to measure it effectively, despite it not being the most abundant 'metal'. It is important to note that using iron abundance as a tracer for the overall metallicity assumes that other metal abundances change in the same proportion as iron content. In other words, it assumes that the heavy metal distribution of a star is the same as the sun, which is well justified for solar type stars. Metal-poor stars, on the other hand, do not necessarily follow this distribution as they are usually enhanced in α elements (Aller and Greenstein, 1960; Wallerstein, 1962; Fuhrmann, 1998; Reddy et al., 2006; Adibekyan et al., 2012, 2013; Recio-Blanco et al., 2014) and therefore the metallicity has to account for an α-enrichment correction (Yi et al., 2001). α-elements are elements whose most abundant isotopes are integer multiples of 4, which is the mass of helium nucleus (the α particle).

Chapter 2

Motivation

In this thesis, we will conduct a spectroscopic investigations of giant planet hosts with the goal of understanding how they are formed. In particular, the goal of this work is to understand whether the super-massive planets can be able to form with the CA model. This work is motivated by the two recent works that obtained somehow contradictory results about the formation of very massive planets. Below, we present the main findings of these two works: Santos et al. (2017b) and Adibekyan (2019).

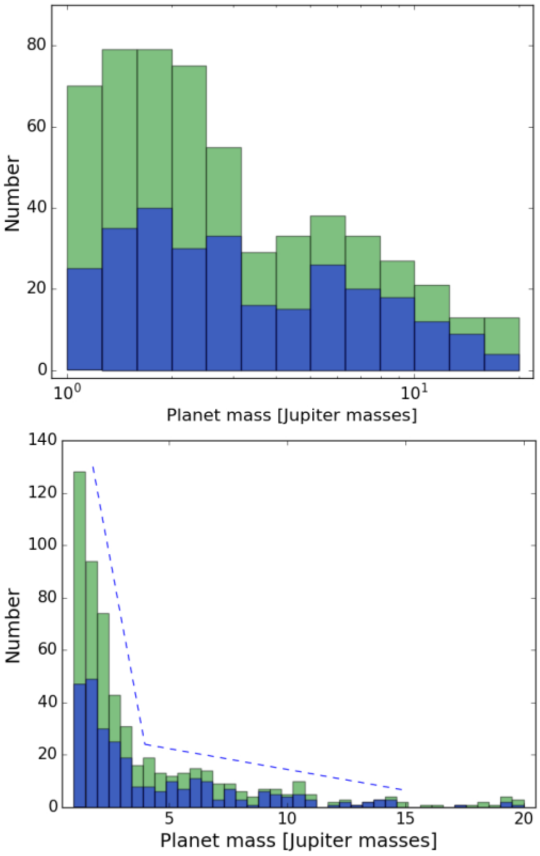

Figure 2.1: Mass distribution of giant planets with solar type-stars hosts, in linear (BOTTOM PANEL) and logarithmic (TOP PANEL) scale. The blue includes only the study sample and the green corresponds to all the planets in exoplanet.eu database. SOURCE: Santos et al. (2017b)

In the work of Santos et al. (2017b), the characteristics of the mass distribution of giant planet with solar-type hosts were examined in search for more hints into their formation process. The authors selected stars that have the Teff, $\log g$, [Fe/H] and mass listed in SWEET-Cat and visual magnitudes lower than 13. Hosts with effective temperature in between 4000K and 6500K were selected. Also they selected the planets with mass between 1 and 15 M_{jup} with orbital periods between 10 days and 5 years. The reasoning behind this selection is detailed in the paper, but in summary, the authors aimed at selecting massive planets orbiting around FGK stars with precisely determined stellar properties.

When analysing the distribution of the mass of giant planets (see Figure 2.1), Santos et al. (2017b) noticed a possible mass breakpoint at about 4 M_{jup}. This was seen both when looking only at the restricted sample and at the full sample of planets extracted from the exoplanet.eu[1] database (Schneider et al., 2011). In logarithmic scale this breakpoint in mass is seen as two maxima separated by a valley, while in the linear scale it is observed as a change of the slope of the distribution.

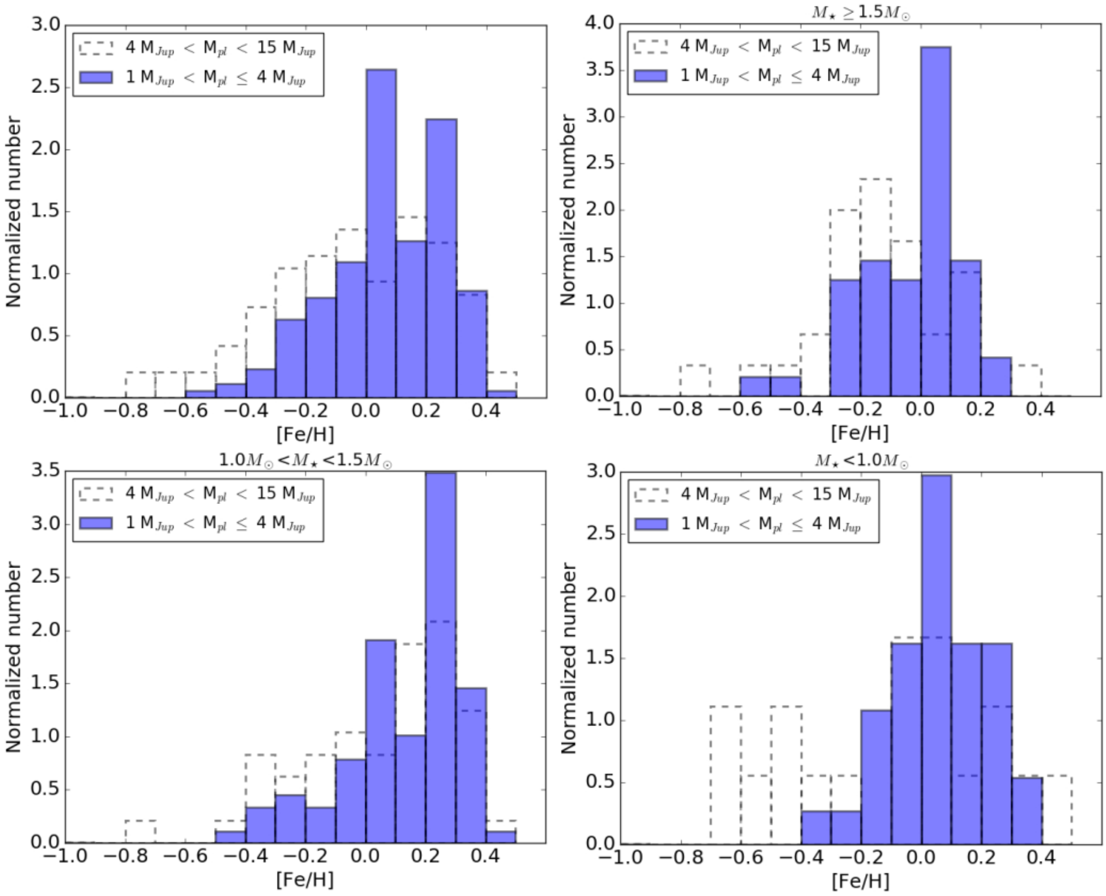

Figure 2.2: Metallicity distribution for stars with giant planets in different mass regimes, separated by 4 different stellar masses regimes (all stars, $M_\star \geqslant 1.5M_\odot$, $1.0M_\odot < M_\star < 1.5M_\odot$ and $M_\star < 1.0M_\odot$). SOURCE: Santos et al. (2017b)

The author then compared the metallicity distribution of the planets hosts dividing then into host of planets with masses above and bellow 4 M_{jup}. They also divided the hosts into 3 stellar mass groups: low-mass stars with $M_\star < 1.0M_\odot$, intermediate stars with $1.0M_\odot < M_\star < 1.5M_\odot$ and massive-stars with $M_\star \geqslant 1.5M_\odot$. As the authors found, and as showed in in Figure 2.2, in all the mass regimes the stars hosting super-massive planets had on average lower metallicity than the stars hosting Jupiter-like planets. Another interesting thing the authors

---

[1] `http://exoplanet.eu/catalog/`

noted is the hosts of massive planets ($M_{pl} > 4M_{jup}$) span a wider range of metallicity regardless of the stellar mass regime studied.

The authors then performed a clustering analysis between planet mass and metallicity, with the assumption of two distinct clusters using a Gaussian mixture (see Figure 2.3). The algorithm split the data into two categories: higher and lower mass planets, with lower mass giants having a narrower range of mass and metallicity when compared to massive planets hosts. An offset of 0.14 dex between the center of the clusters was observed, making the lower mass giant planets hosts more metallic on average.

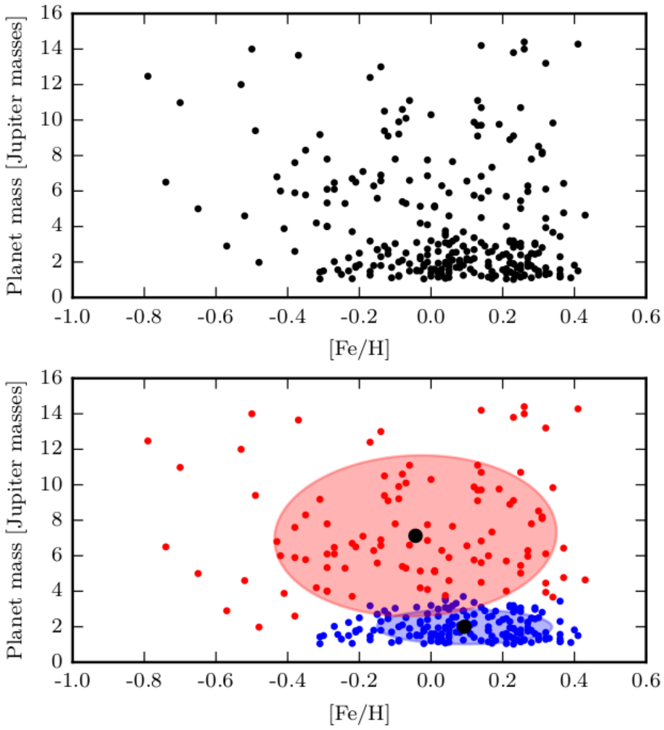

Figure 2.3: Planet mass against the stellar metallicity of the study sample, and the plot repeated after a Gaussian mixture is applied (BOTTOM PANEL). SOURCE: Santos et al. (2017b)

The authors proceeded to do some statistical tests in between the planetary mass regimes, for different stellar mass regimes and also provided a comparison with field stars (i.e. stars without planets) in the solar neighbourhood. They found a statistically significant difference between the lower mass giant hosts and the field stars, however, when comparisons are made in between the massive planets hosts and field stars they found similar results.

Based on the observed correlations, the authors concluded that up until 4 M_{jup}, given the increase of planet formation with metallicity, core-accretion is most likely to be the mechanism responsible for the formation of these planets. As mentioned in the introduction, the core-accretion paradigm predicts a clear dependence between metallicity and giant planet formation, since the more metallic the disk is, the more likely a giant planet to be formed in CA. On the other hand, as the planetary mass increases, there is not as clear dependence on metallicity, which may point towards gravitational instability being the main formation mechanism of these planets. These results imply that there is a planetary mass limit ($\sim 4M_{jup}$) above which core-accretion no longer dominates the formation of giant planets. However, there is likely an overlap of the two different population.

The author also suggested that core-accretion could still be responsible for the formation of massive planets $M_{pl} > 4M_{jup}$, simply by bigger disks being able to form higher mass planets, despite the lower metal content. However, they also denote that in such case, the model would then have to explain the change in regime at around the break-point mass and furthermore explain how hosts of massive planets are compatible with field dwarf distribution, which is not seen for lower mass giants.

In summary, Santos et al. (2017b) provided an observational evidence for the existence of two different population of giant planets with a break point mass of $\sim 4M_{jup}$ above and below which the planet formation scenarios might be different.

Schlaufman (2018), also looked at the issue of the formation of massive planets via CA. The author reached to a conclusion similar to the one of Santos et al. (2017b) i.e. giant planet with masses below 4 M_{jup} are formed via CA, and the planets with masses $>\sim 10M_{jup}$ are formed via gravitational instability.

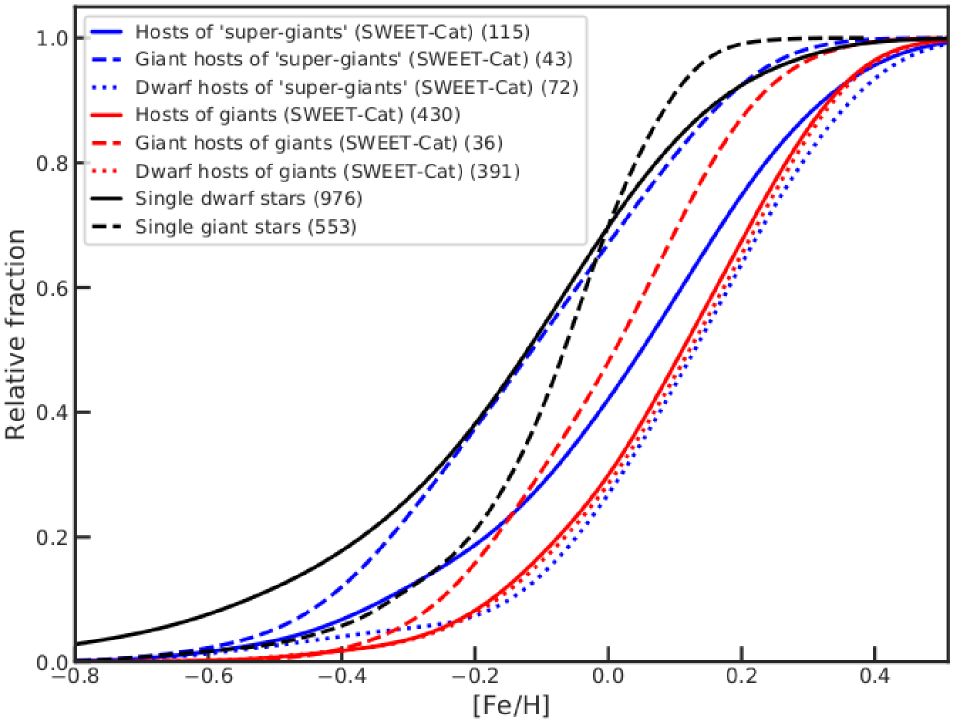

Figure 2.4: KDE fit of the cumulative metallicity distributions of hosts of giant planets ($50M_{\oplus} < M_{pl} < 4M_{jup}$) (red) and hosts of 'super-giants' ($4M_{jup} < M_{pl} < 20M_{jup}$) (blue) and field stars on the solar neighbourhood (black). Dwarf hosts ($M_{\star} < 1.5M_{\odot}$) correspond to the dotted lines and giant hosts ($M_{\star} > 1.5M_{\odot}$) to the dashed lines. SOURCE: Adibekyan (2019)

In a different analyses, Adibekyan (2019) examined the metallicity distribution of giant and super-giant planet hosts (see Figure 2.4) by separating the mass of hosts stars into giant ($M_{\star} > 1.5M_{\odot}$) and dwarf ($M_{\star} < 1.5M_{\odot}$) hosts. The author found that on average the field dwarf stars (without planets) have the lowest metallicities, while the hosts of 'super-giant' planets, and especially, hosts of giant planets are more metallic. However, these differences were not statistically significant. When comparing the metallicity of single giant stars to that of giant hosts of 'super-giants' planets, it is interesting to note that single giant stars have a slightly higher average metallicity than giant hosts of 'super-giants' planets, with giant hosts of giant planets being the most metallic of the bunch. Finally analysing the dwarf stars, there is a statistically significant difference between dwarfs without planets and dwarf stars hosting any type of giant planets. There is not a significant difference between the dwarf host of 'super-giant' and giant planets. This result suggests that metallicity, regardless of planet mass, may play an essential role in the formation of giant planets.

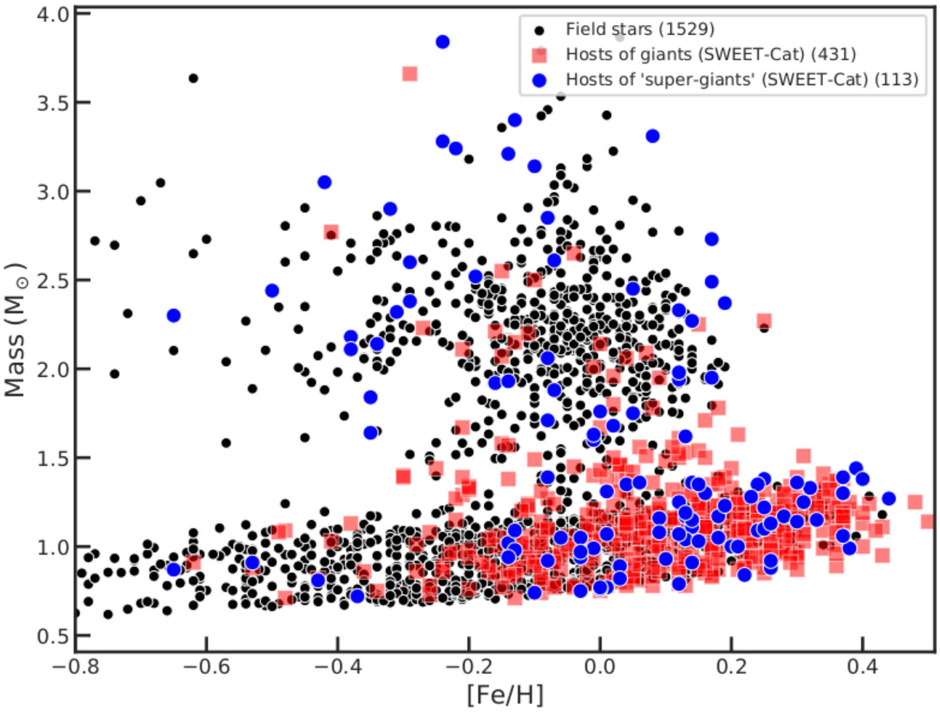

Figure 2.5: Stellar mass and metallicity dependence of hosts of giants (red) and super-giants (blue) and solar neighbourhood field stars (black). SOURCE: Adibekyan (2019)

Figure 2.5 shows the distribution of the stars with and without planets on the stellar mass - stellar metallicity diagram. Everything previously stated can be seen in the graph, where there is a clear behaviour change between dwarf stars and giants stars. We denote that there is a metallicity maximum at around 0.2 dex for giant stars (with and without planets). Dwarf field stars have on average significant lower metallicity when compared to dwarf hosts.

Summarizing the aforementioned finding, the works of Santos et al. (2017b) and Schlaufman (2018), suggest that giant planet up until $\sim 4M_{jup}$ appear to have been formed through core-accretion, while planets with higher masses are preferentially formed via GI. In contrast, the analyses of Adibekyan (2019) does not sustain the claims of a break point mass above which the planet formation channels change.

In all these studies, iron content was used as a proxy of the overall metallicity. However, as mentioned in the introduction, especially for metal-poor stars, this approximation is not accurate as these stars are usually enhanced in α elements (including O, Mg, and Si which are important for planet formation), which could compensate for the lack of iron.

The goal of this work is to perform a spectroscopic analyses to giant planet hosts and derive the chemical composition of several elements in order to get a complete view on the metal content of the stars and the protoplanetary disks. In this thesis we will calculate the summed mass percentage of all heavy elements in the disk based on the abundances of C, O, Mg, Si, and Fe, using the model from Santos et al. (2015) and Santos et al. (2017a). From this calculations we will conclude whether the protoplanetary disks where the massive and super-massive planets are formed might have enough heavy elements to be able to form the planets via CA.

Chapter 3

Sample Selection

In order to obtain the study sample for this work we made use of SWEET-Cat[1]: a catalog of stellar parameters for stars with planets (Santos et al., 2013b) and Exoplanet.eu[2]: The Extrasolar Planets Encyclopedia (Schneider et al., 2011). To avoid mismatching problems of a star having different names in each database, a code was utilized which allowed to cross-match the datasets by stellar name and by coordinates[3]. This cross-matching lead us to a sample of 4040 star-planet systems.

We then selected 444 planets with masses between 1 and 13 Mjup. This planetary mass range was chosen to ensure there were only giant planets in the sample, and the upper limit of 13 M_{jup} was to make sure there were not brown dwarfs. The later value corresponds to the deuterium-burning mass limit for brown dwarfs at solar metallicity (Saumon et al., 1996; Spiegel et al., 2011). 13 M_{jup} is commonly used as a boundary between giant planets and sub-stellar objects with significant central deuterium burning (Caballero, 2018). However, it is important to mention that the mass limit of the deuterium burning is dependent on several parameters of the object (Chabrier et al., 2014). It is also important to add that there is a mass region where massive planets and low-mass brown dwarfs overlap (Schneider et al., 2011; Baraffe et al., 2010).

We also restricted our sample only to the host stars for which SWEET-Cat provides homogeneously derived stellar parameters (see Santos et al., 2013a; Sousa et al., 2018, 2021). This leave us with a sample of 335 objects. In addition, we selected only FGK type hosts with temperatures between 4500K and 7500K (317 planets). The reason for this restriction was to guarantee the highest possible precision in the determination of the stellar parameters, as well as abundances of the elements.

Once the aforementioned constraints have been enforced we were left with 272 stars. 200 of these stars are hosting planets with masses between 1 and 4 M_{jup} (225 planets) and 89 are hosting planets with masses between 4 and 13 M_{jup} (92 planets). There are 17 stars hosting planets with masses both lighter and heavier than 4 M_{jup}.

Since our goal is to perform a homogeneous chemical analysis of the planet host stars and because the sample size allows, we decided to constrain the sample to only stars for which there are available spectra obtained with the HARPS and HARPS-N (HARPS north) spectrographs (Mayor et al., 2003; Cosentino et al., 2012). The choice of HARPS and HARPS-N is based on the simple facts that these spectrographs have a very high resolution (R ∼ 100000) and that

---

[1] `https://www.astro.up.pt/resources/sweet-cat/`

[2] `http://exoplanet.eu/catalog/`

[3] `https://github.com/B-Soares/NASA_EU_databases`

more than half of the stars have publicly available spectra obtained with these spectrographs (table 3.1). This left us with 139 different stars with 163 planets with masses between 1 and 13 M_{jup}. At this point, the sample had 47 stars with 48 planets with masses over 4 M_{jup} and 102 stars with 115 planets with masses under 4 M_{jup}. The sample contains 10 stars which have planets with masses over and bellow 4 M_{jup}. We should note that by imposing this constrain on spectrographs, we are not biasing the sample toward any particular sort of star or planet.

Spectrograph	**Number of stars**
ESPADONS	14
FEROS	28
FIES	4
HARPS	1
HARPSN	29
HARPSS	109
NARVAL	13
SARG	2
SOPHIE	37
UVES	35

Table 3.1: Table with the number of stars per spectrograph from which the spectra had been obtained.

From the aforementioned HARPS sample of planet hosts, we further selected those which have spectra with signal-to-noise (SNR) ratio above 200. High quality (high resolution and high SNR) spectra is crucial for precise characterization of stars with planets (Sousa et al., 2008; Santos et al., 2013a). We also decided to remove a few hottest (Teff > 6400 K) and coolest (Teff < 4700 K) stars from the sample because the precision of the abundances determined for these stars was measurable lower than for the rest of the stars. Finally, the main sequence stars ($\log g > 4.0$ dex) with the effective temperature below 5300 have been removed from the sample. The reason behind this choice was the difficulty in deriving the carbon and oxygen abundances for these stars spectroscopically.

These latter restrictions left the sample with 113 stars and 134 planets. Over 4 M_{jup} we had 38 different stars with 39 planets and bellow 4 M_{jup} there was 83 different stars with 96 planets. 8 stars have planets with both bellow and above the $4M_{jup}$ mass limit. The main characteristics of the sample stars are presented in table A.1.

The distributions of the stellar mass, Teff, metallicity, as well as the mass of the planets are shown in Figure 3.1. The histogram of the stellar mass (top left panel), shows that for either planet mass regimes, most stars have masses of around 1.2 $M_{\odot}$. However, the stellar masses for the massive planet hosts spans a larger range when compared to the one for giant planets hosts. The effective temperature graph in Figure 3.1 unveils that the sample has a few cooler stars, however most stars have a higher temperature. Finally, we can see that most stars actually have near solar or super-solar (> 0.2 dex) metallicities. On average the stars hosting planets with $M_{pl} < 4M_{jup}$ are on average less metallic than those hosting super-massive planets. This is in agreement with the results presented in Santos et al. (2017b)).

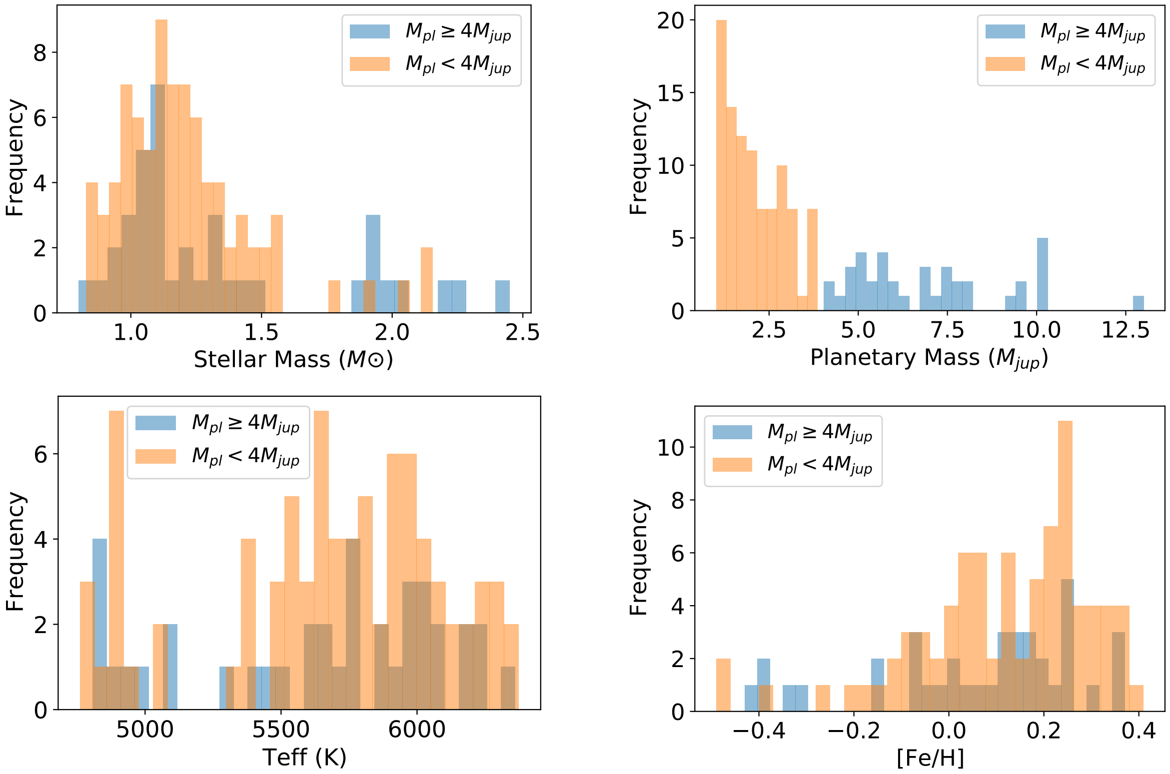

Figure 3.1: The distribution of stellar and planetary mass, Teff, [Fe/H] of the sample stars. Stars hosting planets with masses below and above 4 M_{jup} are presented in orange and blue colors, respectively.

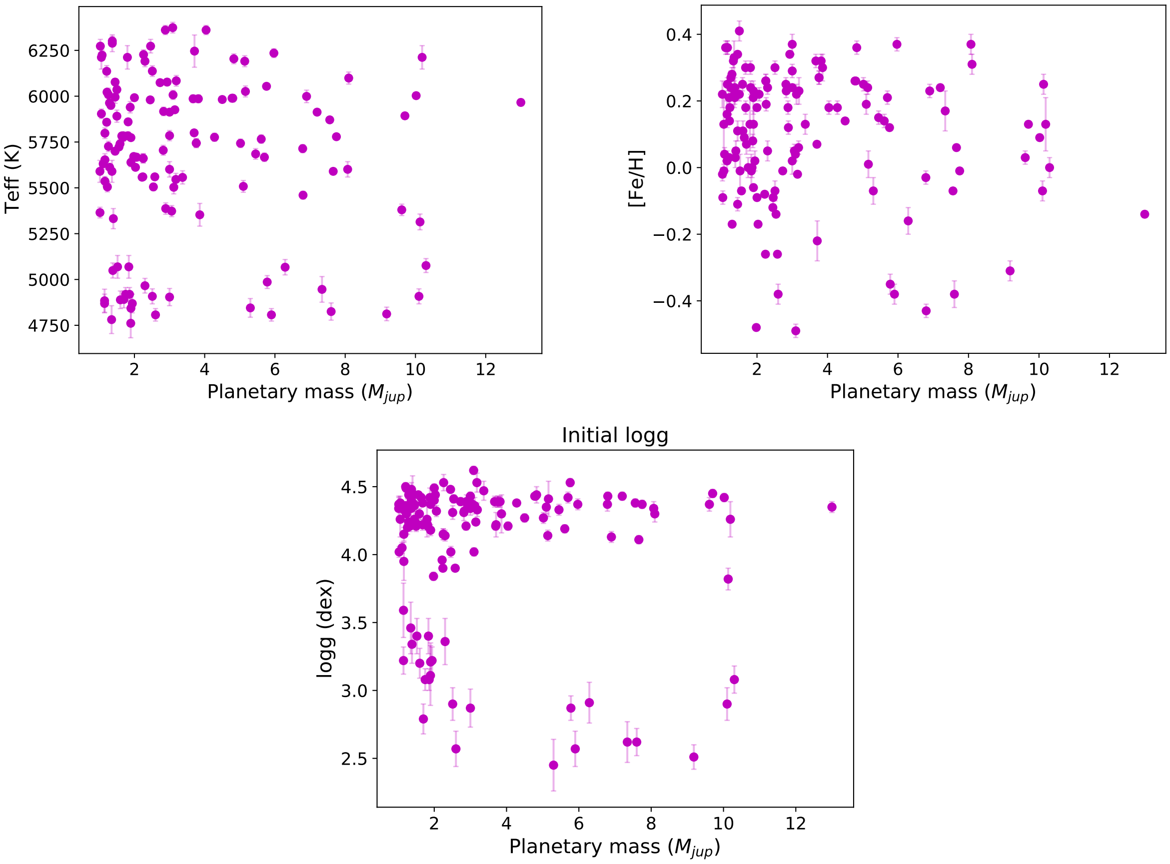

Figure 3.2: Relation between planetary mass and stellar properties: Teff, [Fe/H], and $\log g$.

In Figure 3.2 we show the dependence of planetary mass on the stellar Teff, [Fe/H], and $\log g$. The figure shows no clear correlation between stellar effective temperature and planetary mass. The top right panel shows that most of the giant planet hosts, below 4 M_{jup}, have higher metallicities, with only some stars having sub-solar (< 0.0 dex) metallicities. The figure also does not reveal a correlation between planetary mass and surface gravity. Most of the hosts have $\log g > 4.0$ dex meaning that they are in the main sequence i.e. dwarf stars.

In Figure 3.3 we show the spectroscopic Hertzsprung-Russell (HR) diagram i.e. dependence of $\log g$ on Teff. The stars of our sample are represented in magenta color and the HARPS GTO sample of Adibekyan et al. (2012) are shown in grey.

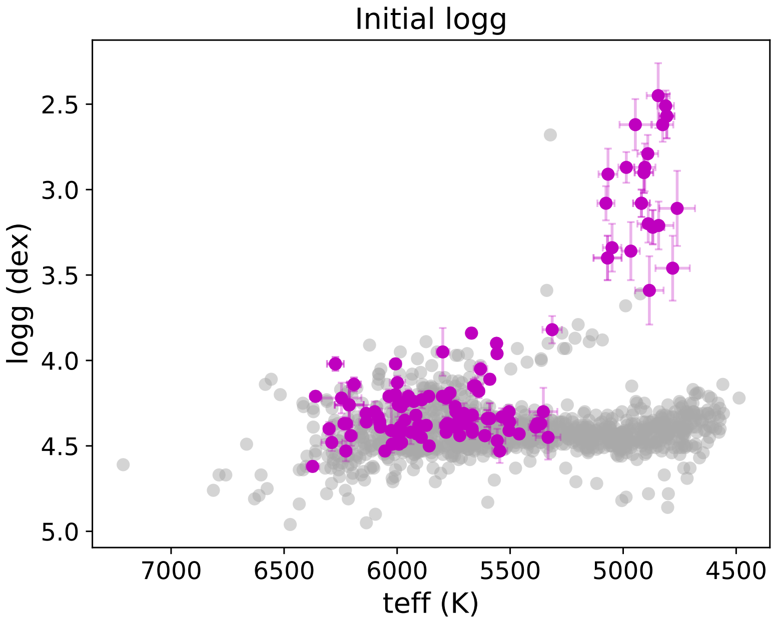

Figure 3.3: Hertzsprung-Russell (HR) diagram of the sample stars (magenta) with HARPS stars with no planets from Adibekyan et al. (2012) (grey)

Finally, in Figure 3.4 we show the dependence of stellar masses on the metallicity of the planet host stars. In grey, the field stars correspond to the CORALIE giant stars without planets (Alves et al., 2015) and dwarf HARPS stars with no planets (Adibekyan et al., 2012). It is important to note that both samples of field stars have been searched for planets and none was found. Since the masses of the planet host stars have been determined using the empirical correlation of Torres et al. (2010), the masses of the field stars were re-determined using the same methodology. This minimizes the potential systematic errors between the samples of stars with and without planets.

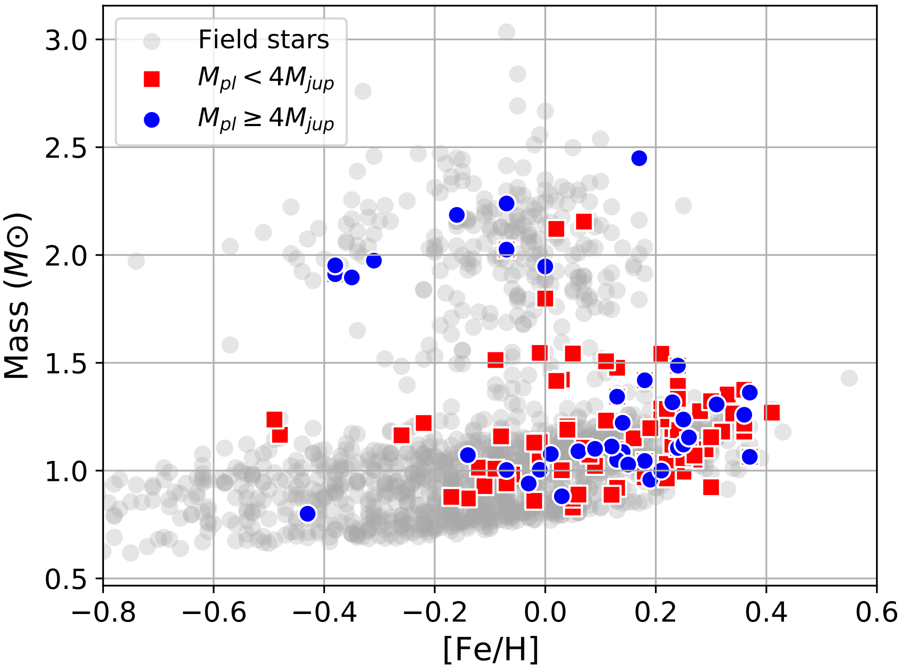

Figure 3.4: Stellar mass as a function of metallicity for the stars hosting giant (red squares) and super-giant (blue circles) planets. Field stars are shown as semi-transparent grey circles.

Chapter 4

Methods

In this chapter we describe the techniques and methodologies used in this work. We start by describing the method of determination of the chemical abundances of stars and we explain the choice of the elements. Sequentially, analyse the problem with the carbon and oxygen and disclose what was required to predict them. Finally, after getting all the abundances necessary, it was time to estimate the building blocks parameter. This parameter shall be further investigated and interpreted in this chapter.

4.1 Determination of the abundances

After defining the sample which is presented in Table A.1, we aimed at determining chemical abundances of the sample stars. The stellar parameters of the stars were taken from the SWEET-Cat database (Santos et al., 2013b). For this research project, we derived the abundances of carbon (C), oxygen (O), magnesium (Mg), silicon (Si), titanium (Ti) and nickel (Ni).

The first 4 elements together with iron (Fe) are the major contributors for the rocky planetary building blocks. The abundance of Ti was derived as well in the interest of getting an idea of another α-element content for the sample. α-elements are know to not necessarily follow the iron abundance, when the [Fe/H] is at sub-solar values. At these metallicities the [α/Fe] abundance ratio increases with the decrease of iron abundance (e.g. Aller and Greenstein, 1960; Wallerstein, 1962). At solar and super-solar metallicities, usually the [α/Fe] ratio is close to zero i.e. is solar (Adibekyan et al., 2013). Lastly, the abundance of Ni was derived because one of the oxygen lines (at 6300Å) is blended with a Ni line, and the determination of O abundance required the knowledge of the Ni abundance (Bertran de Lis et al., 2015).

The ARES (Sousa et al., 2015) code automatically measures the EWs of spectral lines from so-called 1D spectra. The code determined the SNR of the spectrum and based on it performs a local continuum normalization for each line. ARES also automatically measures the radial velocity of the stars and corrects for it. Then for the provided list of lines it identifies the lines and measures their line properties (EW, FWHM, strength) by fitting a Gaussian. The code also identifies blends and performs multi-Gaussian fits.

In order to be able to run MOOG (Sneden, 1973) which is a radiation transfer code, we need to provide the list of lines in a specific format. This line list includes the wavelength, the atomic number of the element, the excitation potential, the oscillator strength, the damping parameters and finally the EW derived from ARES. As input, MOOG also requires the model of atmospheres. In our computations we adopted the MARCS (Gustafsson et al., 2008) models of atmospheres. These models of atmospheres for each star was created by using the stellar atmospheric parameters taken from SWEET-Cat.

Based on the aforementioned information, MOOG determines the chemical composition for each spectral line for each element. To calculate the abundance of elements with several spectral lines we adopted the method described in Adibekyan et al. (2015a). This method was developed to minimise the impact of outlier lines on the final abundances. For elements with three or more lines, the method calculates the weighted mean and the weighted standard deviation using the inverse of the distance from the median value as a weight. The weighted average becomes the new abundance value and the weighted standard deviation is taken into account for the final error, together with the error due to the uncertainties of stellar atmospheric parameters. The later is calculated by varying the stellar parameters by the amount equal to their uncertainties and estimating the variation of the individual abundances. Finally in order to get the values derived compared to the sun, from the abundances we subtract the abundance determined for the Sun. As a solar reference abundances we took those determined from the solar spectra reflected from Vesta.

It is relevant to note, for this worked we used the ARES V2.0[1] (Sousa et al., 2015) and MOOG 2019[2] (Sneden, 1973). We note that using different version of MOOG may result in non-negligible variations on the final abundances. However, since our aim is to perform a relative analysis of stars hosting giant and super-giant planets, the impact of the version of MOOG is minimal as long as we always use the same version for all the stars.

4.1.1 Abundance difference using the initial and corrected surface gravity

Before going any further, we are going back a few steps. As mentioned in the Sample Selection chapter, a few cool stars were removed, for different reasons, one of them being the difference between the abundances obtained using the initial and the corrected surface gravity.

The need for precise and accurate stellar parameters together with the lack of well-constrained surface gravity using spectroscopy, lead to the use of the surface gravity correction from the work of Mortier et al. (2014), replicated in equation 4.1. In the study, what in this work is $\log g_{cor}$ corresponds to the asteroseismic surface gravity that takes into account the effective temperature and the spectroscopic surface gravity, in this work nominated $\log g_{ini}$. This simple correction will allow to derive more precise chemical abundances spectroscopically, which is one of the main goals of this thesis. The errors of the $\log g_{cor}$ considered are the same ones as on the SWEET-Cat database.

$$\log g_{cor} = -3.89 \times 10^{-4} \cdot Teff + 2.10 + \log g_{ini} \tag{4.1}$$

In Figure 4.1 we show how the correction of $\log g$ impact the abundance determinations of Mg, Ti, Si, and Ni. We show the difference in the abundances determined with the initial and corrected $\log g$ values as a function of Teff. The figure clearly shows that the impact of $\log g$ is strongest for the hottest and coolest stars for Si and Mg. Abundances of Ni and Ti are not significantly affected by the change of $\log g$ for stars hotter than about 5300K. For all the elements, the largest difference is observed for stars with Teff < 4700K. These stars are removed from the sample.

---

[1] `http://www.astro.up.pt/~sousasag/ares/`

[2] `http://www.as.utexas.edu/~chris/moog.html`

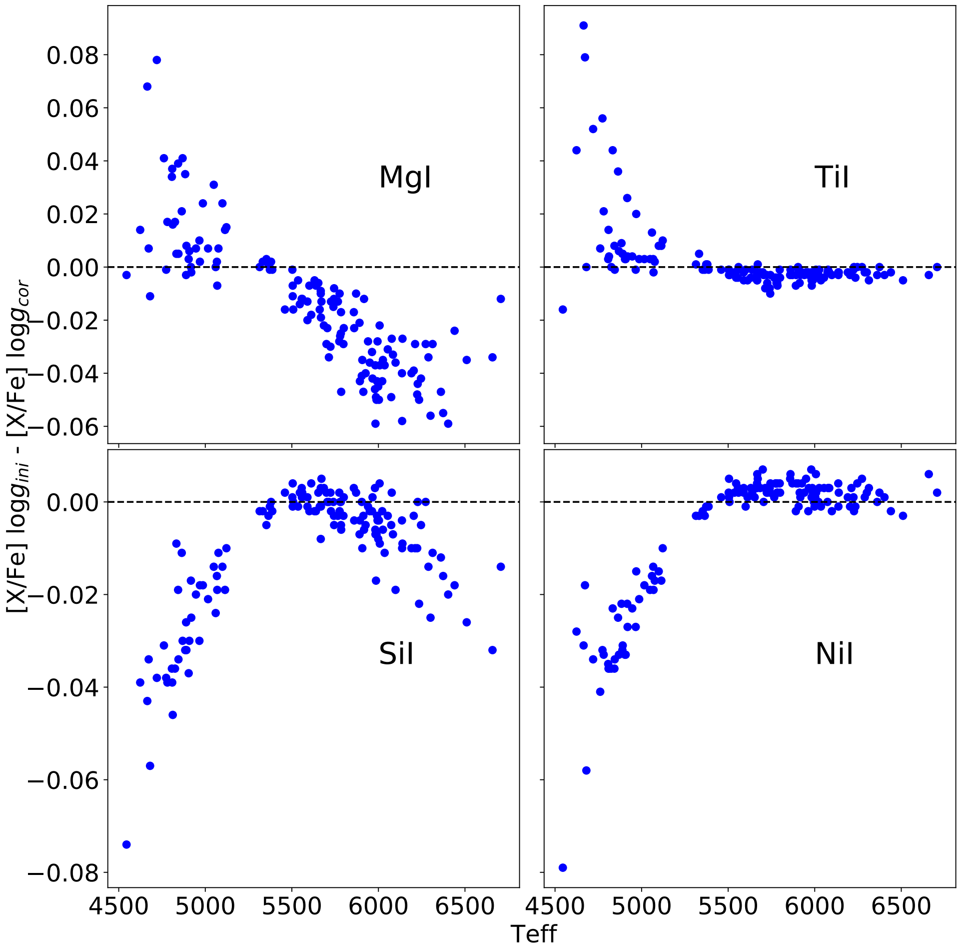

Figure 4.1: The difference between the abundances of Ni, Si, Ti and Mg obtained using ARES+MOOG using the initial log and the corrected vs effective temperature, for the sample stars after the cut of only HARPS spectrograph.

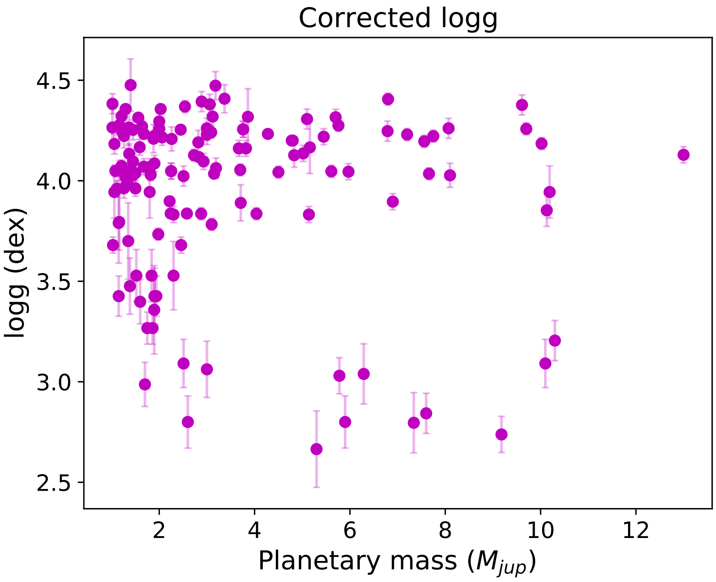

Figure 4.2: Corrected $\log g$ using the relation from Mortier et al. (2014) (equation 4.1) with planetary mass.

In Figures 4.2 and 4.3 we replicated the graphs from Sample Selection chapter with the surface gravity after applying its correction.

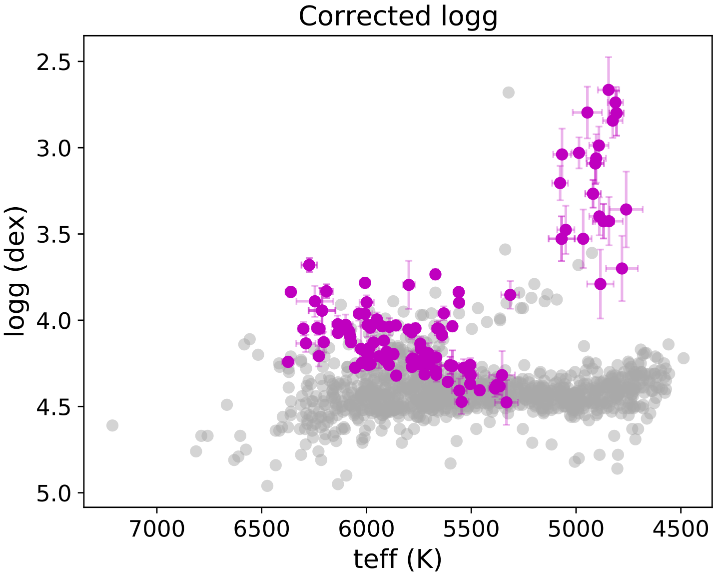

Figure 4.3: HR diagram of the sample (magenta) with a comparison with the HARPS stars with no planets Adibekyan et al. (2012) (grey) after correcting the surface gravity using the relation 4.1 from Mortier et al. (2014)

4.1.2 Derivation of Mg, Si, Ti and Ni

Although we determined the abundances of Mg, Si, Ti, and Ni, the ones that are most relevant for the current work are Mg and Si. The abundances of Ti and Ni were derived in a semi-automatic way. Since both these elements have significant number of spectral lines (22 for Ti and 40 for Ni) we simply removed the outlier lines i.e. spectral lines that delivered abundances significantly different from the mean abundance. Silicon has 14 lines and Magnesium only has 3, as such, we performed a careful visual analysis of all the spectral lines of these elements.

For Silicon, since we have a good amount of lines, it is easier to detect an outlier, a line that delivers an abundance significantly different from the mean value. Opposite to what we have done for the derivation of Ti and Ni abundances, for Si we did not remove any line, but re-measured the EWs manually (see the next section for details on manual EW measurements). The lines that showed an abundance difference from the mean value larger than 0.1 dex were re-measured manually. This could mean that out of the 14 silicon lines, for a star, we could need to remeasure 7 of the lines or, in most cases, 1-4 of the lines. In the last effort, if the spectral line is not possible to be effectively measure and disturbs highly the final result, it would be removed.

Since Mg has only three lines available in the spectra, the identification of possible outliers is practically impossible. In addition to that two of the lines are very complicated to measure manually with high confidence. For the aforementioned two lines, overall ARES measurements can be considered more reliable then the manual ones. The third Mg line at 5711.09Å is more isolated and can be measured manually with a higher confidence. Therefore, for Mg, to check the abundance, we measured the Mg line at 5711.09Å for all the stars and compared with the automatic EW measurements by ARES. For cases of substantial differences (not many cases) the automatically measured EW was replaced with the re-measured value.

4.1.3 Manual EW measurements

Up until fairly recent, it was actually not possible to get EW automatically and programs that allow for manual measurement of the EW were used for the entire process. An example of such program is IRAF[3] (Image Reduction and Analysis Facility). Fortunately, in the latest version of ARES a new feature was added that gives the user the possibility to measure the EW manually as the task "splot" of IRAF does. In order to be able to measure lines manually, ARES needs the stellar spectra, the wavelength of the lines to be measured and ARES input parameters file (mine.opt).

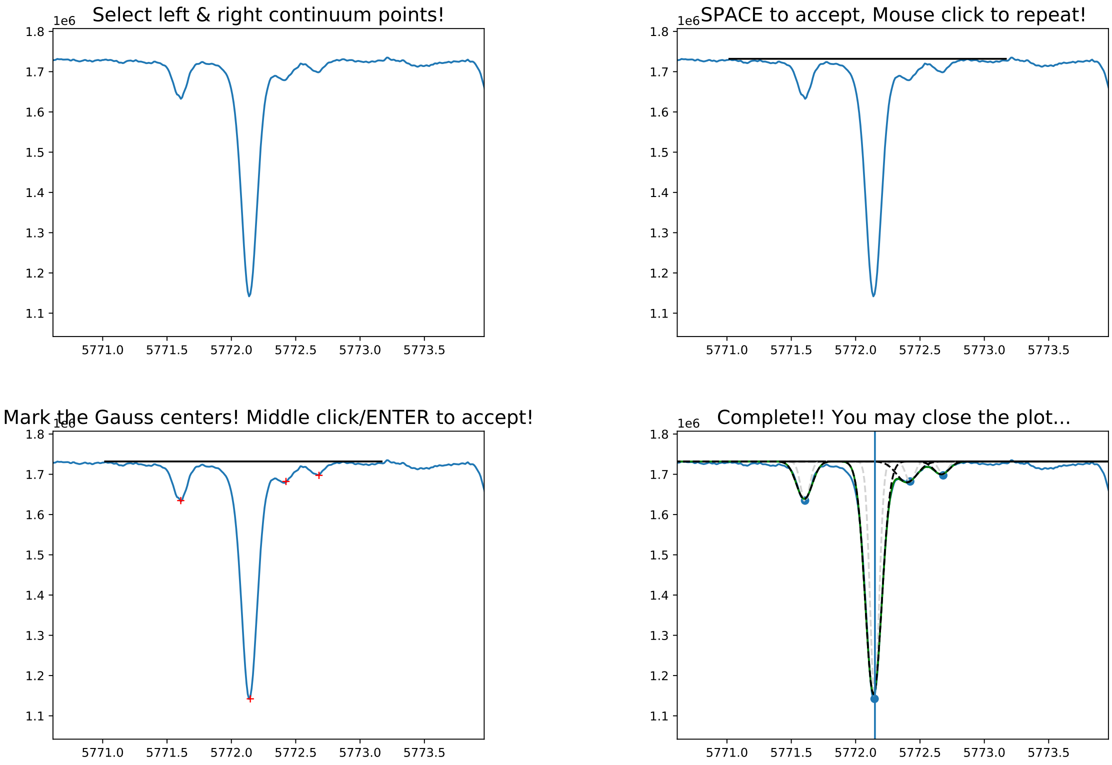

Figure 4.4: Step by step tutorial print screens of how to measures the EW by hand using ARES. In the example the silicon line 5772.150Å in the spectrum of Vesta (reflected from the Sun) is shown.

Figure 4.4, which are print screens from ARES taken in between each step, illustrates how the manual measurement of spectral lines is done with ARES. In order to do so, we select a small wavelength region, but keeping in mind we need to have continuum on both ends of the region. After that, we choose the left and right regions for the continuum placement. Then, the user indicates the centers of the spectral lines to be fitted with Gaussian profile. On the bottom right panel of the Figure 4.4 we see printed in grey and black a few of the iteration needed before the final one in green that follows the same behaviour as of the spectra. In the terminal, ARES provides with more information of the calculation, for instance it displays the EW and respective error and the number of iterations needed.

---

[3] `https://iraf.net/`

4.1.4 Offset in abundances

After measuring the EWs (automatically and manually) and using the tools and methods mentioned earlier, we determined abundances of the elements. These abundances were derived relative to the Sun. The solar reference values were obtained using the Vesta spectrum (Adibekyan et al., 2016). In Figure 4.5 we show the distribution of the abundances determined for the sample stars. The same figure also shows the abundances of the HARPS GTO sample of stars without planets (Adibekyan et al., 2012) and evolved star CORALIE sample (Adibekyan et al., 2015b).

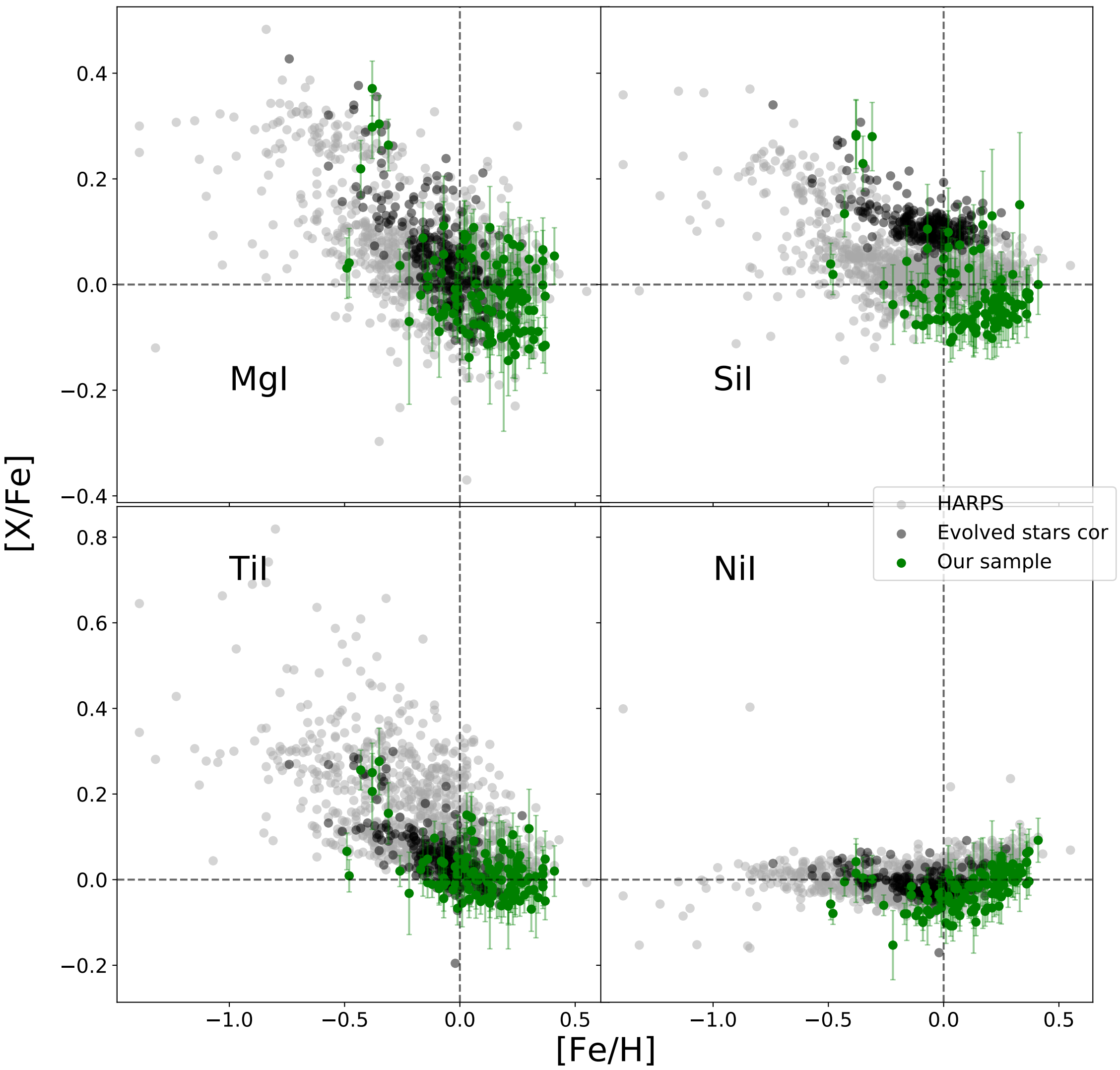

Figure 4.5: Comparison of [X/Fe] obtained with the corrected log g after the lines correction of our sample (green) with evolved stars from Adibekyan et al. (2015b) (black) and HARPS stars with no planets from Adibekyan et al. (2012) (grey) against the iron content ([Fe/H]).

The Figure 4.5 clearly shows an offset in the Si abundance determined for the stars of the current sample, the HARPS dwarf sample, and the evolved sample of CORALIE. The offset (visible e.g. at solar metallicities) is less apparent for Mg, Ti, and Ni. The 'Evolved stars cor' from the label, corresponds to the abundances of the evolved stars after a correction to the effective temperature was done as explained in the work (Adibekyan et al., 2015b).

We found it unlikely that the main reason of the observed offset was the EW measurements since the offset was mostly observed for one element. Alternatively, the difference could come from i) usage of different models of atmospheres (MARCS in this work and ATLAS9 in the previous works), ii) the usage of different version of MOOG (MOOG 2019 in the current work and MOOG 2014/2009 in the previous works), and iii) from the fact that the reference abundances of the Sun used in this work were derived with MOOG2014 and ATLAS9 models of atmospheres, while the abundances of the stars are derived by using MARCS models of atmospheres and MOOG 2019 code, and finally iv) from the usage of corrected surface gravities in the current work when compared to the spectroscopic $\log g$ values used in the previous works.

We determined the composition of the Sun (using Vesta spectrum) by using MOOG2019 code and MARCS models of atmospheres after correcting the $\log g$ value as explained above. The stellar parameters used for Vesta were: Teff = 5770 ± 10 K; $\log g_{corr} = 4.39 \pm 0.02$ dex; $V_{tur} = 0.95 \pm 0.02$ Km/s; [Fe/H] = 0.02 ± 0.01 dex. Since we used the same EWs as in the previous works, all the differences in Vesta abundances should be related either to the choice of the model of atmospheres or the version of the MOOG code. The correction of $\log g$ for the Sun is very small (4.44 vs 4.39 dex). In table 4.1 we show the composition of the Sun determined in this work and in the previous works. The table shows that the largest abundance difference among the four elements represented in 4.5 is observed for Si.

Our test suggest that the main source of the observed offset is the choice of the models of atmospheres and the version of MOOG. In any case, it is important to note that this observed offset or any systematic errors is irrelevant for our analysis since our goal is to compare the abundances of the stars hosting giant and super-giant planets all derived using the same models and tools.

Element	**Vesta (old)**	**Vesta (this work)**	**Difference**
C	8.490 ± 0.016	8.382 ± 0.025	-0.108
O	8.656 ± 0.071	8.738 ± 0.031	0.082
Mg	7.603 ± 0.020	7.559 ± 0.014	-0.044
Si	7.579 ± 0.020	7.524 ± 0.029	-0.055
Ti	5.007 ± 0.016	4.993 ± 0.021	-0.014
Ni	6.265 ± 0.013	6.229 ± 0.015	-0.036

Table 4.1: The composition of Sun (derived from the reflected spectrum of Vesta) determined in the previous works and in the current work.

4.1.5 Spectroscopic determination of the C and O abundances

Both Carbon and Oxygen have two weak lines in the visible that are not always easy to measure automatically. However, as a first step we run ARES to measure the EWs of these lines automatically and using the aforementioned spectroscopic tools and models of atmospheres we determined their abundances. The results are shown in Figure 4.6.

The Figure 4.6 shows that the C abundances of our sample stars, overall, have a similar distribution to the HARPS dwarf stars with planets (Delgado Mena et al., 2021), nonetheless a few clear outliers are seen. However, looking closely, we notice that our sample, specially for lower metallicities has lower [C/Fe] even bellow the HARPS, which could be because of the offset not having been perfectly adjusted. The right panel of the figure shows the [O/Fe] as a function of [Fe/H] for our sample stars (in green) and for the HARPS dwarf stars (Bertran de

Lis et al., 2015). One can see the large error bars for many of the stars that point towards those lines having been badly measured.

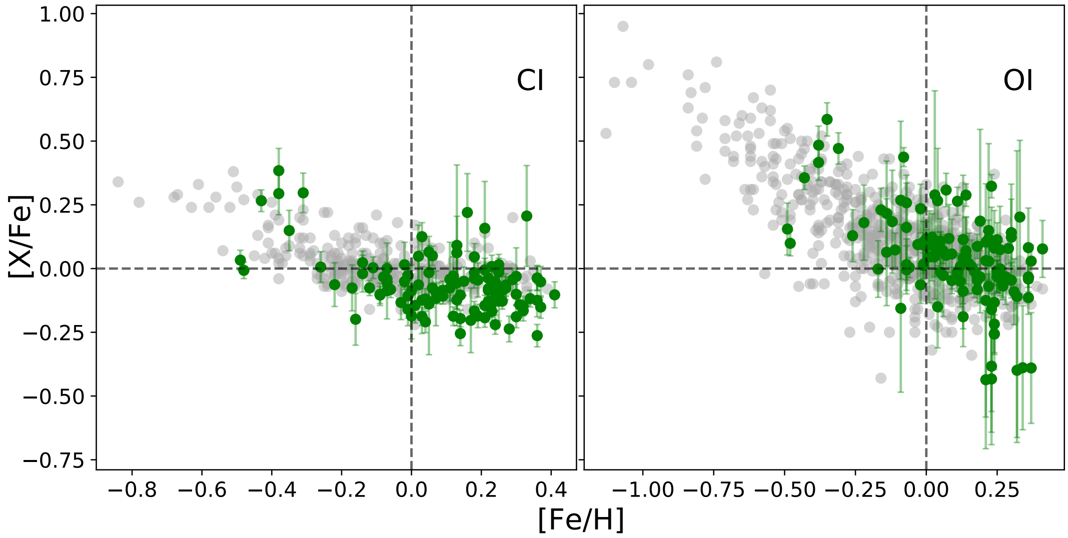

Figure 4.6: [X/Fe] vs [Fe/H] of our sample straight from ARES+MOOG, after the Vesta correction (green), together with the HARPS stars with no planet (grey)

To explore further where the large dispersion observed in C and O abundances come from we looked at the abundances determined from each individual line separately. Carbon has 2 lines at 5380.32Å and 5052.15Å. In Figure 4.7, we show these two lines abundances plotted for our sample stars as a function of stellar parameters. In the figure we also plot the HARPS stars with no planets (Delgado Mena et al., 2021). We notice that apparently, the 5052.15Å line seems to deliver lower abundances than the 5380.32Å. The systematic difference in the abundance determinations from these two lines lead to the large scatter observed in Figure 4.6.

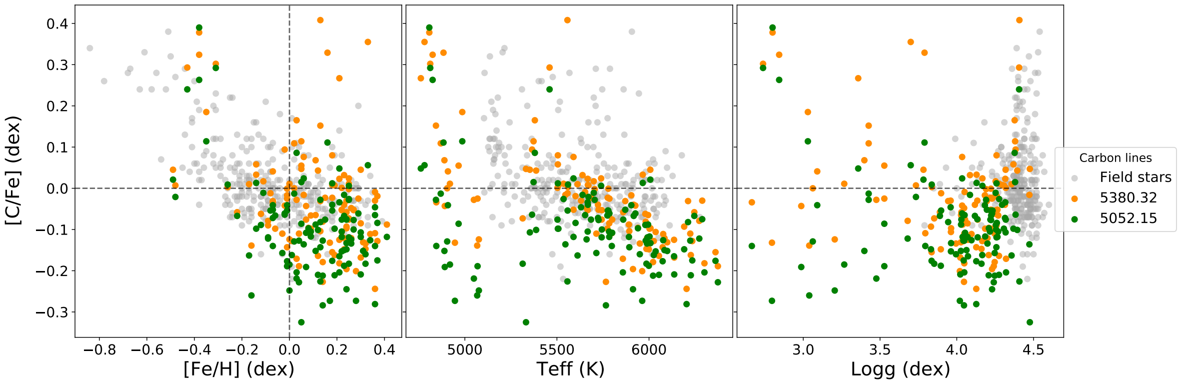

Figure 4.7: Comparison of HARPS field stars (Delgado Mena et al., 2021) carbon abundances (grey) with our sample stars for which the C abundances are determined from the EWs of the lines measured automatically by ARES. The abundances are shown as a function of stellar parameters.

Looking into the middle and left panels of 4.7 we see that the cool stars of our sample, that correspond to the ones with lower $\log g$, have very dispersed carbon values, ranging from -0.3 < [C/Fe] < 0.4. On the other hand, the dwarf stars of our sample actually tend to be carbon poor, mostly having sub-solar [C/Fe] abundances, especially when analysing the 5052.15Å line.

In the figure 4.8 we show a similar plot to Fig. 4.7, but for two Oxygen lines. The 6300.39Å line is blended with Ni which contributes heavily to the EW measurement. Since the Nickel impact on that line changes with temperature and other parameters it is very difficult to properly account for it (Bertran de Lis et al., 2015). The 6158.71Å oxygen line was measured only for 52 stars (out of 113 stars): mostly in hot dwarf stars. For the 52 stars that have both lines, we see that the abundances derived for each line are rather distinct, which explains the large error bars seen on the right panel of Figure 4.6.

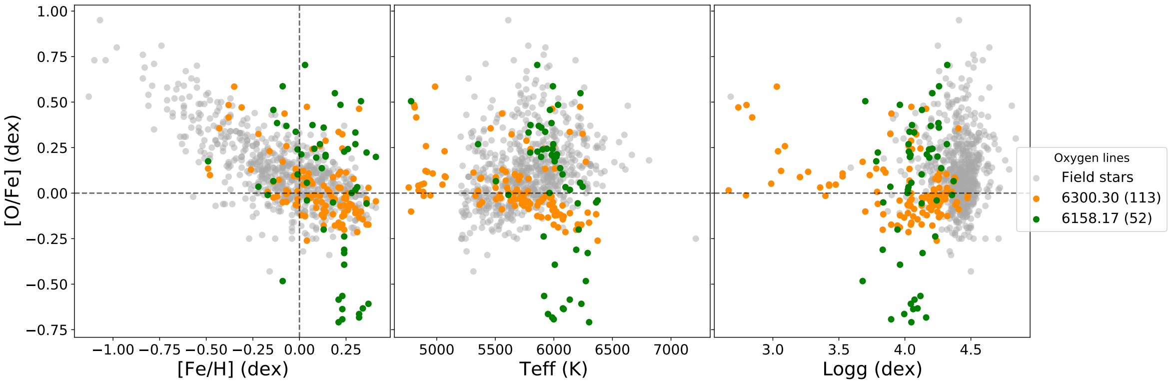

Figure 4.8: Comparison of HARPS field stars (Bertran de Lis et al., 2015) oxygen abundances (grey) with our sample stars for which the O abundances are determined from the EWs of the lines measured automatically by ARES. The abundances are shown as a function of stellar parameters.

Our general conclusion from the performed tests was that the it is not possible to determine reliable C and O abundances for all the sample stars using our standard spectroscopic technique. Even if we remove the contribution of Ni from the 6300Å oxygen line and measure the EWs of all these lines manually, we would not be able to determine the abundances (reliably) for the coolest stars. As such, we decided to use a machine learning (ML) method to estimate the abundances of C and O. The method is described in the next section.

4.2 Prediction of the Carbon and Oxygen Abundances

Machine learning (ML) is a branch of artificial intelligence (AI) and computer science that makes use of data and algorithms in order to identify patterns and make decisions with minimal human intervention. ML replicates the way humans learn and improves its accuracy gradually, making use of data analysis that allows for the creation of automated analytic models. There are many algorithms that allow such end, which of course, are chosen in response to what the work requires, in our case, we make use of random forests (RF) (Breiman, 2001). Here we will be feeding the method datasets to train the algorithm in order to predict an accurate outcome.

4.2.1 Random Forest (RF)

Random forest (Breiman, 2001) is a supervised form of ML. Random forests incorporates the operation of decision tree together with ”bootstrapping” with replacement (Márquez-Neila et al., 2018). A decision tree is a basic building block of a random forest, since it is a way to divide the dataset in multiple subsets based on the similar characteristics of the branches (Márquez-Neila et al., 2018). Because decision tries are extremely responsive to changes in training set, the split is done in a way to accentuate the gain in information entropy (Márquez-Neila et al., 2018). Bootstrapping is a resampling method that is commonly adopted to estimate statistics on a population by sampling a database with replacement. In other words, in bootstrapping, the subsets created out of the training sample are independent and drawn at random with replacement. Each decision tree will have its own result and with the use of averaging of all of them or in some cases major-voting (Acquaviva, 2016), which is demonstrated in Figure 4.9. The combination of many trees solves bias-variance trade-off, and since each tree is independent, they can be constructed in parallel, making it a fast algorithm with reliable results (Miller, 2015).

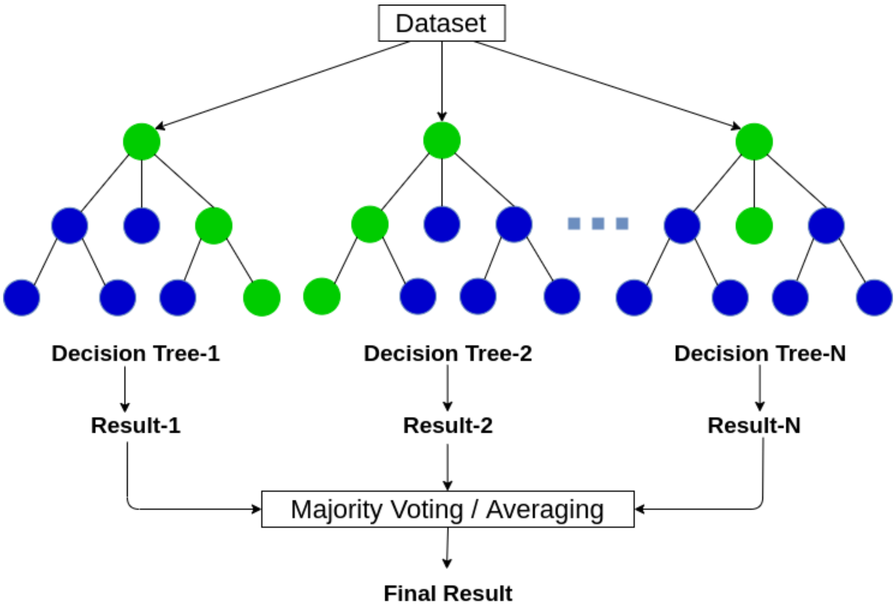

Figure 4.9: Example of what happens in a random forest algorithm. SOURCE: google images

4.2.2 Implementing RF in python

In order to create the model, we separate the data into features and targets, which correspond to the columns the model uses to make the prediction and the predictions, respectively.

In order to form the model, we are splitting the data into training and testing sets randomly. During the training process, the model is allowed to see the answers so it can predict accurately from the features. In training, we give the model any information relevant to the problem in order for the model to be able to learn the relationship between the data and what to predict. There are two key elements in connection to the split of the training and testing sets, the 'test size' which is the size of the data that is being tested and the 'random state' which is responsible for how the split is done to the dataset. If the test size is too big, the model will be a perfect fit to that dataset. However, when we applied values from a different dataset to the model the results will not be as accurate since it is following so closely the behavior of the first one. There must be a sufficient number of values to test that span the whole database's range. In other words, we must ensure that we do not leave any crucial data out of the test set while also ensuring that it is not excessively large and only suitable for that dataset's data. In order to do so, we need to try and find the best testing size and 'random state' for each dataset desired. The code used in this work was developed by Barbara Soares (private communications) as part of the Master thesis. The code already had these values perfected for the features and targets for two datasets that were used for training.

4.2.3 Databases

We then had two model databases that we could use, the HARPS model and the APOGEE one. The HARPS model was obtained from the Adibekyan et al. (2012) sample of FGK dwarf stars, with oxygen abundances from Bertran de Lis et al. (2015) and carbon abundances from Suárez-Andrés et al. (2017). The sample consists of 527 stars for which abundances of C, O, Mg, Si, and Fe are available. The APOGEE (Holtzman et al., 2015; Majewski et al., 2017) database was obtained from the 16th data release (Ahumada et al., 2020) of APOGEE-2 (Majewski et al., 2016), with abundances derived by Jönsson et al. (2020). By selecting only RGB (red-giant branch) stars with [Fe/H] $\geqslant$ -1 and SNR $\geqslant$ 300, that ended up being having a little over 15000 stars.

4.2.4 Improving the model to our input parameters

The original ML code made use of different input parameters to get the abundances. In this work our input parameters (features) are the [Si/H], [Mg/H] and [Fe/H], the first two derived in this work and the latter obtained from SWEET-Cat. The output parameters (targets) are abundances of [C/H] and [O/H]. Given that the input parameter were changed when compared with those in the original ML code, we tried to perfect the model before applying it to our data. In order to do so, we went by hand changing the 'random state' of the model and looked for the better values of a few statistic parameters (see next paragraph). Only these parameters needed to be checked because the 'test size' and the rest had been perfected for each database and were not heavily influenced by the change in the input parameters.

In order to test it, we created a model from a database and then we applied the same database to the model and checked some statistics as we changed the 'random state'. These parameters were the R^2 (coefficient of determination), the mean difference, standard deviation of the prediction and the true standard deviation of the true values. To verify if the model was good, we looked for a high value of R^2, since this parameter compares the true values with the prediction. For example, for a $R^2 = 0.92$ it means the model explains 92% of the variance in the output. We also looked for a small mean difference which would mean the values predicted were close to the real ones. And for the standard deviation of the prediction and standard deviation of the true values, we basically made sure they were similar, to make sure the model was neither making the output a much wider or smaller range of values than the reality.

4.2.5 Selecting the database

We ran two models using the HARPS and APOGEE databases and got our sample stars carbon and oxygen abundances following each model. We realise that the HARPS one fitted the expectation slightly better than the APOGEE (see Figure 4.10). For the APOGEE database, we see that the C abundances were systematically larger, and the O spread had a considerably narrower range of values compared to the other estimates. The HARPS model was eventually selected.

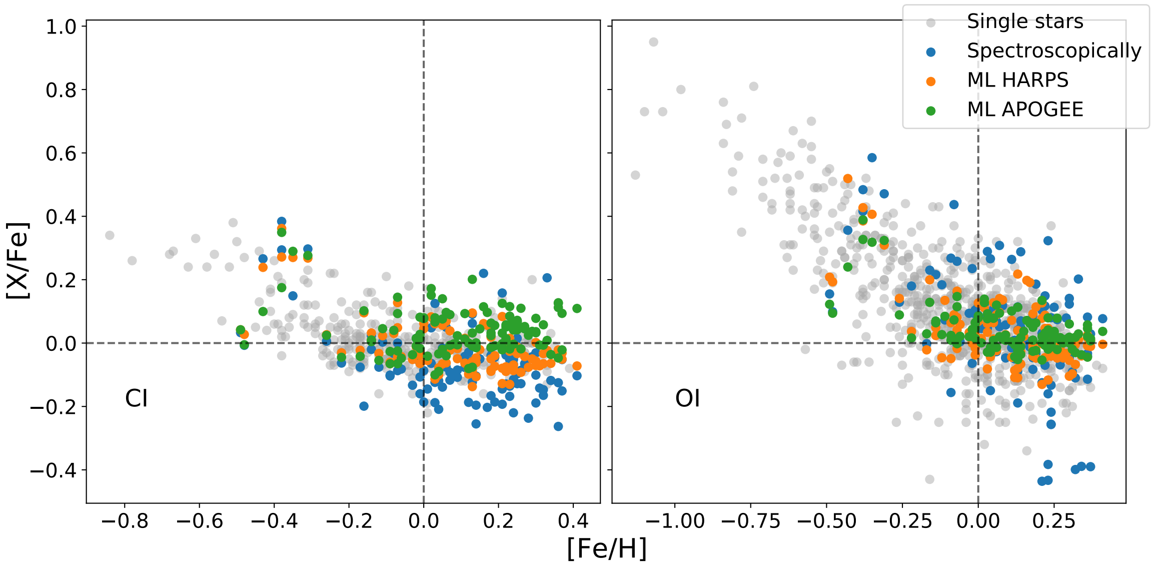

Figure 4.10: Carbon and oxygen abundances of the HARPS stars with no planets (grey), of our sample stars derived spectroscopically (blue) and of the abundances obtained with the machine learning trained with a HARPS database (orange) and the abundances obtained with machine learning trained using an APOGEE database (green).

4.2.6 Obtaining the final C and O abundances and errors

In pursuance of trying to get the most robust output, and to estimate the uncertainties of the abundance estimates we performed the following bootstrapping analysis. By considering a normal distribution for the input parameters (with a sigma equal to their uncertainties) we run the ML code 1000 times per star. We then calculated the mean and standard deviation of the output parameters. This allowed us to the get the abundances and the error that comes from the input parameters, but we still need to take into account the model error.

Random forest does not have a direct output of the error which makes it complicated to obtain a model error. The ML code was modified to force a change for the 'random state' parameter and create 100 different models for each set of input parameters. Thus now we are taking into account what would happen to the model if we had made a different decision to this 'random state' value. Having the model error and the input abundances error, the final error is simply the root sum of squares of the errors.

Finally, we now have all of the abundances needed for the main goal of this work, calculating the composition of planet building blocks.

4.3 Composition of planet building blocks

As we know, the study of stars hosting planets provides us with incredible information about the planetary formation and evolution processes (Mayor et al., 2014). More specifically the study of chemical abundances in the hosts is essential for comprehending the formation of planetary systems (Ida and Lin, 2004b; Mordasini et al., 2012; Adibekyan et al., 2021).

Several studies have shown similarities in the relative abundance of Fe, Mg and Si of the Sun, Venus, Mars, Earth and meteorites. These researches strongly suggest a relationship between the relative abundances of the star with rocky planets and bodies (e.g. meteorites) (e.g. Lodders, 2003; Drake and Righter, 2002; Khan and Connolly, 2008; Sanloup et al., 1999). Mercury does not follow the same bulk compositions, the reason for this most likely being that an external process could have significantly altered its composition (Benz et al., 1988). Nevertheless, Mercury is thought of as an exception, rather than the rule. Determining the abundance in the atmospheres of stars and link them with the properties of planets, may give us information about the internal structure and composition of planets, not only for rocky planets (e.g. Bond et al., 2010; Delgado Mena et al., 2010; Dorn et al., 2015; Thiabaud et al., 2015; Santos et al., 2015; Dorn et al., 2017), but also for giants planets (Guillot et al., 2006; Fortney et al., 2007).

Planetary building blocks are condensates from the stellar nebular that have experienced some fractionation processes (Santos et al., 2017a). In order words, planetary building blocks are primitive objects from which the planets and other bodies in the disk were formed. Given that the goal of this thesis is to get a view on the formation theory for giants and supermassive planets, it is very prevalent to obtain the planetary building blocks of our sample stars. Therefore, having information about the initial objects composition that led to their formation will evidently provide clues towards which theories is most likely correct.

When planet formation models account for equilibrium condensation models they predict a compositional correlation between planets and their hosts (Dressing et al., 2015). Previous studies have referred that the relative abundances do not change spatially or temporally significantly within the disk (Thiabaud et al., 2014; Johnson et al., 2012). This indicates that, regardless of the distance to the star, we may reasonably infer that the abundances in the star are connected to its rocky planets, and that they are also comparable to the composition of the proto-stellar disk in which the star and planets are formed. There are of course, exceptions, for instance, if the planet has undergone internal or external specific physical process, it is possible their initial composition to be different from the present one. There are some processes that can also modify the composition of stars. An example is planet engulfment that has been proposed to have an impact on particular stellar abundances (Israelian et al., 2001; Spina et al., 2021), nevertheless its uncommon.

4.3.1 Model

In this section we will be calculating the expected iron-to-silicate mass fraction - f_{iron}, the water mass fraction - w_f and the summed mass percentage of all heavy elements expected for the planetary building blocks - Z. The model used for this part of the work was the one introduced in Santos et al. (2015) and Santos et al. (2017a).

This model makes use of Fe, Si, Mg, C and O abundances together with H and He, because it assumes them as the most pertinent elements for controlling the species expected from equilibrium condensation models (Lodders, 2003; Seager et al., 2007). Some of these most relevant species are in fact H_2, He, H_2O, CH_4, Fe, $MgSiO_3$, Mg_2SiO_4 and SiO_2. The elements required (Fe, Si, Mg, C and O), are rocky-forming elements and the model includes their mineral phases that are thought to dominate the composition of the crust, mantle (upper and lower) and core of Earth-like planets (McDonough and Sun, 1995; Sotin et al., 2007).

Having said that, a simplified model that calculates the expected mass fractions of different compounds using these species is a justifiable procedure. From the atomic abundances we can easily calculate the molecular abundances and consequently the mass fractions, with simple stoichiometry. The simple stoichiometry equations presented in 4.2 and 4.3 (Santos et al., 2015, 2017a; Bond et al., 2010; Thiabaud et al., 2015; Unterborn and Panero, 2017), are the ones used for this work. The first set of equations 4.2 are for the case when ($N_{Mg} > N_{Si}$) and the second 4.3 for the opposite ($N_{Mg} \leqslant N_{Si}$). By performing an inversion to these equations together with the stellar abundances, it allows us to derive planetary building blocks as expressed in equations 4.4; 4.5; 4.6.

When $N_{Mg} > N_{Si}$ (but $N_{Mg}/N_{Si} < 2$):

$$\begin{aligned}
N_O &= N_{H_2O} + 3N_{MgSiO_3} + 4N_{Mg_2SiO_4} \\
N_{Mg} &= N_{MgSiO_3} + 2N_{Mg_2SiO_4} \\
N_{Si} &= N_{MgSiO_3} + N_{Mg_2SiO_4} \\
N_C &= N_{CH_4}
\end{aligned} \tag{4.2}$$

Contrarily, when $N_{Mg} \leqslant N_{Si}$:

$$\begin{aligned}
N_O &= N_{H_2O} + 3N_{MgSiO_3} + 2N_{SiO_2} \\
N_{Mg} &= N_{MgSiO_3} \\
N_{Si} &= N_{MgSiO_3} + N_{SiO_2} \\
N_C &= N_{CH_4}
\end{aligned} \tag{4.3}$$

The final parameters we intend to obtain are calculated using (4.4; 4.5; 4.6)

$$f_{iron} = m_{Fe}/(m_{Fe} + m_{MgSiO_3} + m_{Mg_2SiO_4} + m_{SiO_2}) \tag{4.4}$$

$$w_f = m_{H_2O}/(m_{H_2O} + m_{Fe} + m_{MgSiO_3} + m_{Mg_2SiO_4} + m_{SiO_2}) \tag{4.5}$$

$$Z = (m_{CH_4} + m_{H_2O} + m_{Fe} + m_{MgSiO_3} + m_{Mg_2SiO_4} + m_{SiO_2})/M_{tot} \tag{4.6}$$

Where $m_x = N_x \cdot \mu_x$ given that N_x corresponds to the number of atoms per species X, computed relative to H and μ_x is the mean molecular weight. Finally, $M_{tot} = N_H \cdot \mu_H + N_{He} \cdot \mu_{He} + N_c \cdot \mu_c + N_O \cdot \mu_O + N_{Fe} \cdot \mu_{Fe} + N_{Mg} \cdot \mu_{Mg} + N_{Si} \cdot \mu_{Si}$.

The results are presented in terms of mass fraction in percentages. It is relevant to reinforce the limitations of this model and the fact that there are some cases which the models does not take into account. An example of this is for when $N_{Mg}/N_{Si} > 2$, the Si is included in olivine and Mg is integrated in other minerals, most of them oxides. Another example of this is that mineralogy is expected to change (Bond et al., 2010) when N_C/N_O >0.8, were silicates are no longer formed and instead carbides are. This implies an enhancement in carbon for the planet building blocks. In other words, in order to get an extremely rigorous model, these cases would needed to be taken into account, nevertheless it does not take away from the model precision of the results, given that the examples above are rare. In our case, this is not a problem given that we do not have any star in those conditions.

The uncertainties of the compositions of the planet building blocks were estimated by performing 1000 Monte Carlo simulations. We varied the input abundances assuming a normal distribution with a sigma corresponding to the errors of the abundances.

4.3.2 Estimating the impact of C and O to the final Z

As we stressed earlier in the chapter, it was very relevant to obtain accurate and reliable results for the C and O abundances. In order to quantify the impact of C and O abundance on the determination of Z, we decided to introduce an offset to the C and O abundances separately and simultaneously, and determine the Z parameter. The results are shown in Figure 4.11.

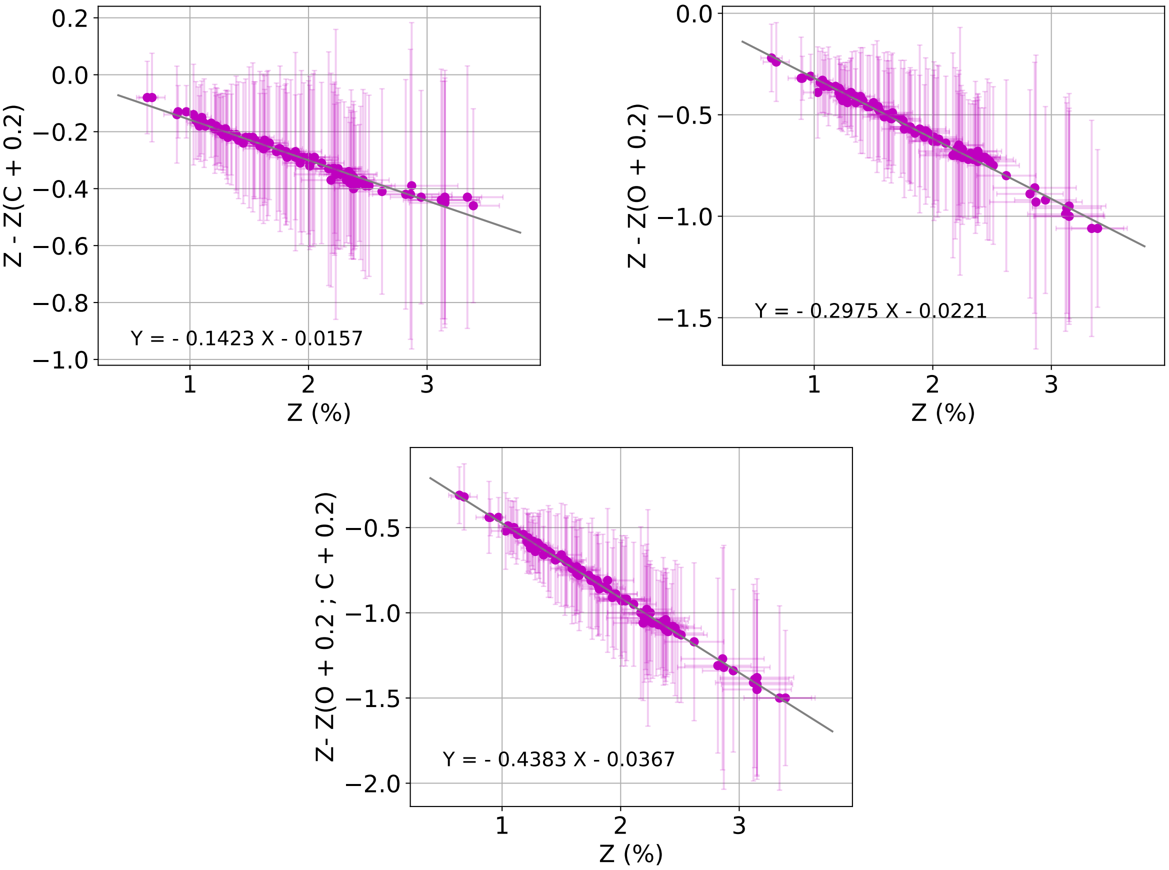

Figure 4.11: Difference in heavy element content Z when the abundance of C and O are increased by 0.2 dex as a function of Z.

Figure 4.11 clearly shows that the abundance of C and O have strong impact on the determination of Z. O abundance, however, has stronger impact than C by a factor of about 2. Increasing the abundance of O by 0.2 dex introduces an increase of Z of about 30%, while the average error for the Z is about 10% (see table C.1).

The main goal of this test was to understand and stress the importance of precise determination of the abundances of these two elements. Fortunately, the precision of our estimation of the abundances of C and O is significantly better than the offset introduced in this test.

Chapter 5

Results

In this chapter, we will report the outcomes of our research, following the same line of work as presented in the previous section. We will start by displaying all of the spectroscopically derived abundances, as well as the C and O predicted by ML. Finally, using comparisons to the Sun, we will provide several parameters linked to planetary building blocks for our sample, along with some statistical tests.

5.1 Composition of planet host stars

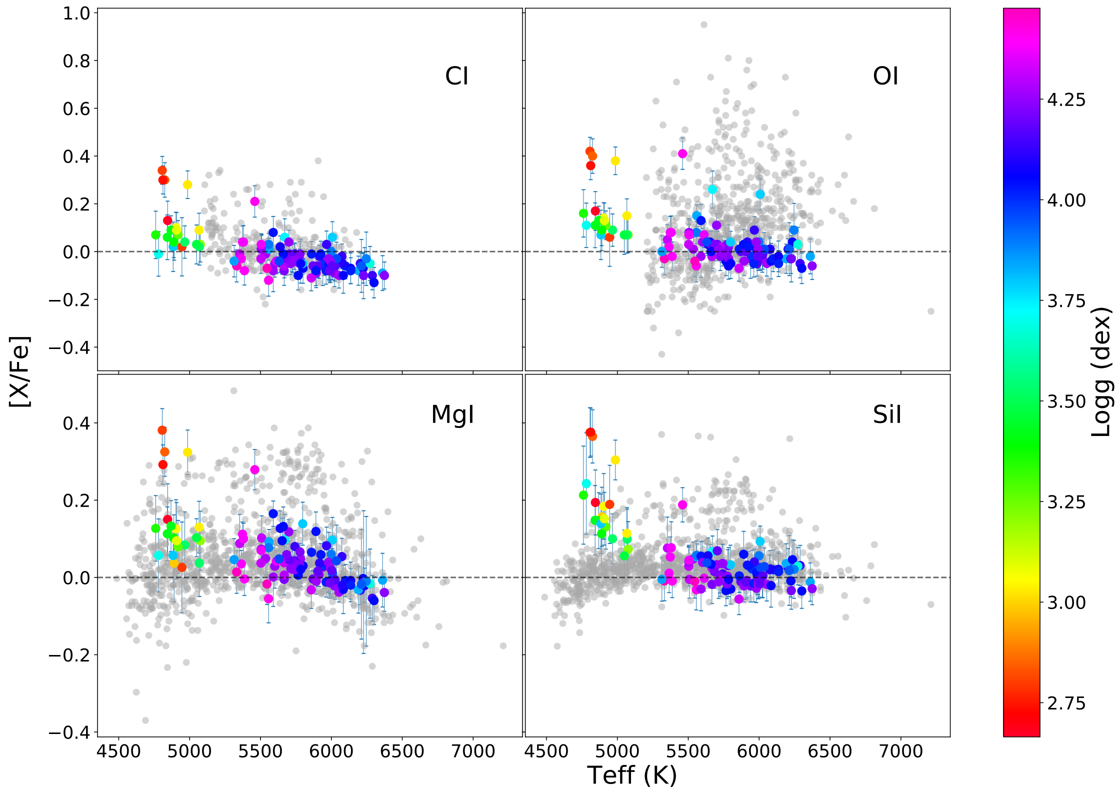

Figure 5.1: [X/Fe] vs Teff color coded to log g for our sample stars The HARPS stars without detected planets (Adibekyan et al., 2012; Delgado Mena et al., 2021; Bertran de Lis et al., 2015) are shown in grey. The abundances of C and O were predicted using ML and the abundances of Si and Mg were derived spectroscopically.

In Figures 5.1 and 5.2 we show the dependence of [C/Fe], [O/Fe], [Mg/Fe], and [Si/Fe] abundance ratios as a function of stellar parameters and metallicity. For comparison, the stars without detected planets from the HARPS sample are also shown. We remind that the abundances of C and O are predicted using a ML technique, while the abundance of Mg and Si are determined spectroscopically. The figures show that the coolest and evolved stars have slighter higher abundances relative to iron, when compared to the solar-temperature dwarfs. Some of these stars are metal-poor and their enhancement in these elements is expected from the Galactic chemical evolution (see e.g. Adibekyan et al., 2012; Delgado Mena et al., 2021). The aforementioned stars also have relatively large uncertainties in the abundances which could be due to unresolved blends or other difficulties (e.g. continuum normalization) related to the spectroscopic measurements (Sousa et al., 2008).

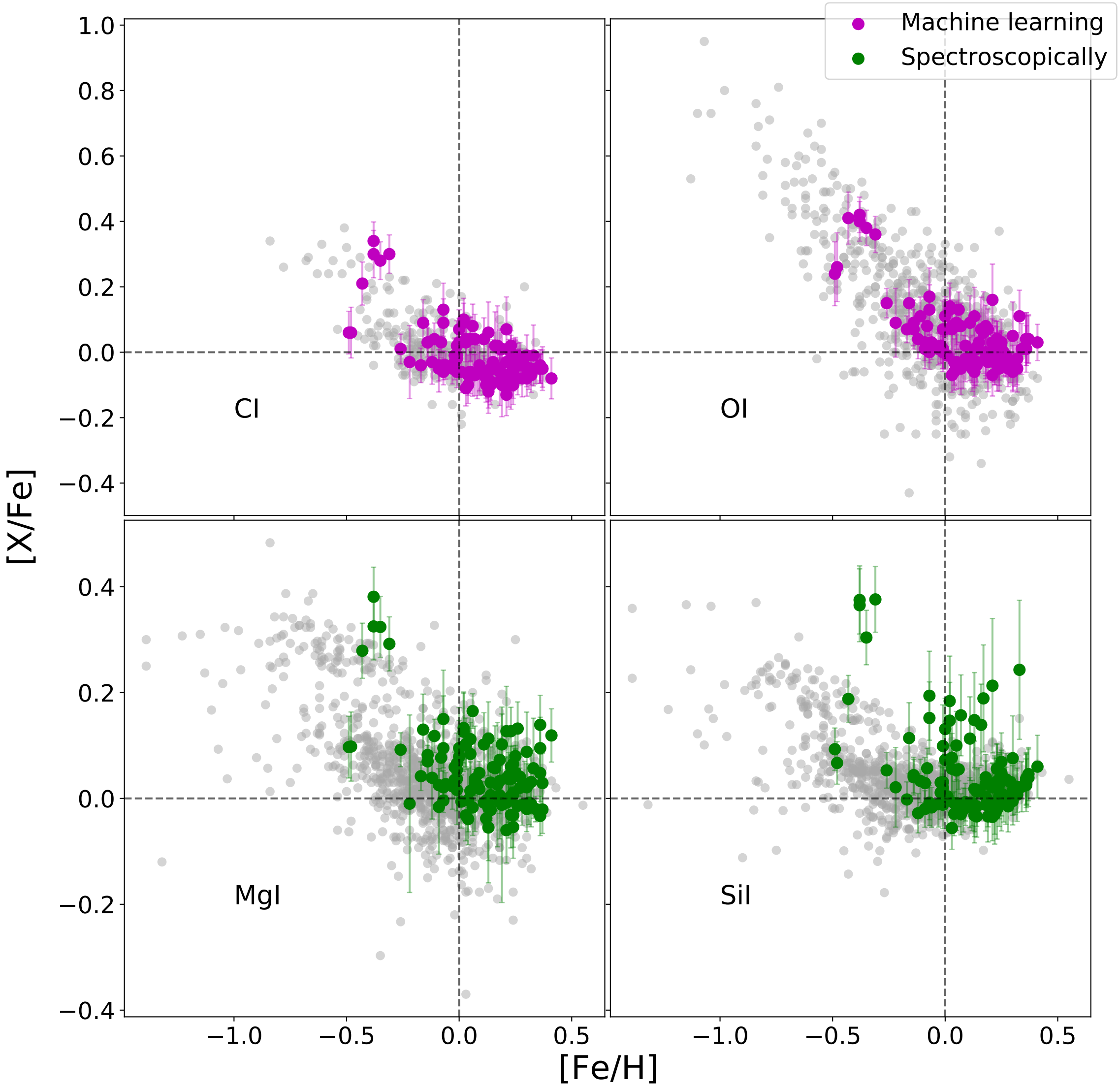

Figure 5.2: The final abundances of [X/Fe] (green) vs [Fe/H] The HARPS stars without detected planets are shown in grey.

5.2 Composition of planet building blocks and formation of giant planets

We can start by showing the water mass fraction and the iron mass fraction of the sample stars. These parameters provide us information on the potential composition of planets, especially the rocky ones. We cannot say that the giants planets are composed of the same amount of iron or water, but we can say, if there were to be Earth-like planets in the disk, their composition could likely follow those parameters. Therefore these parameters are not the upfront goal of this work, but do tell us useful and interesting information on the initial disk composition.

In Figure 5.3 we show the f_{iron} as a function of planetary mass. The symbols are color codded according to the metallicity of the stars. The dashed line shows the f_{iron} for our Solar system taken from Santos et al. (2017a), using the same model as the one used in the current work. The figure shows that the majority of sample disks have lower values when compared to the solar system. We also see that the lower the iron abundance is, the lower the iron-to-silicates mass fraction will be. On the other hand, the higher the iron content, the wider the range of f_{iron} values, which varies from 25% to 36% for [Fe/H]> -0.2.

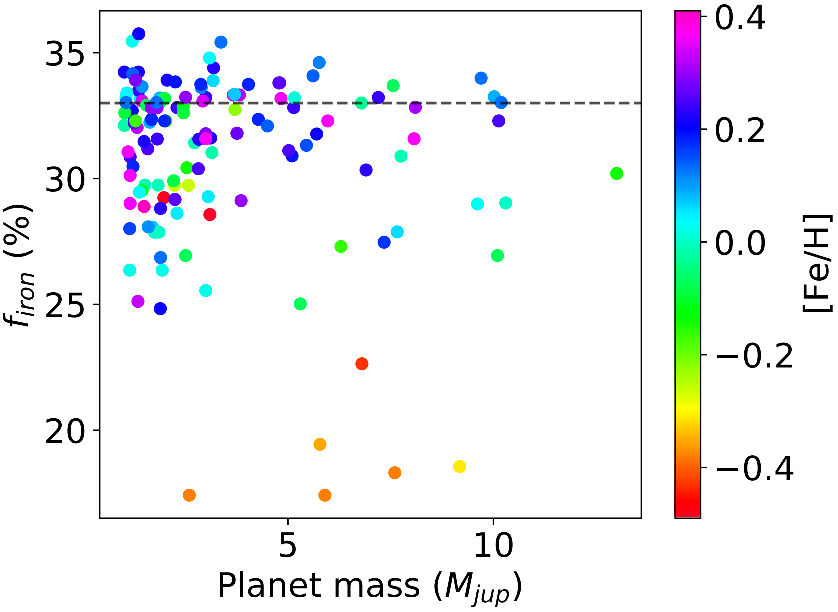

Figure 5.3: f_{iron} - iron-to-silicate mass fraction vs the planetary mass color coded to the metallicity [Fe/H]. The dashed line shows the f_{iron} value for the Solar System.

In Figure 5.4 we show the relation between f_{iron} and planetary mass where we show the giant and super-giant planets in different colors. By comparing the two planetary mass regimes (above and bellow $4M_{jup}$), we see that on average the f_{iron} spans a smaller range of values for Jupiter-like planets when compared with the distribution of f_{iron} of super-massive planets. Interestingly, almost all of the f_{iron} poor disks have super-Jupiters ($M_{pl} \geqslant 4M_{jup}$). The only Jupiter-like planet with a low f_{iron} is in a multi-planetary system with another massive-Jupiter planet. Table 5.1 presents the mean values and standard deviations of f_{iron} for both planetary mass regimes. Jupiter-like planets have slightly higher f_{iron} than their higher mass counterparts, although the difference is smaller than the standard deviations.

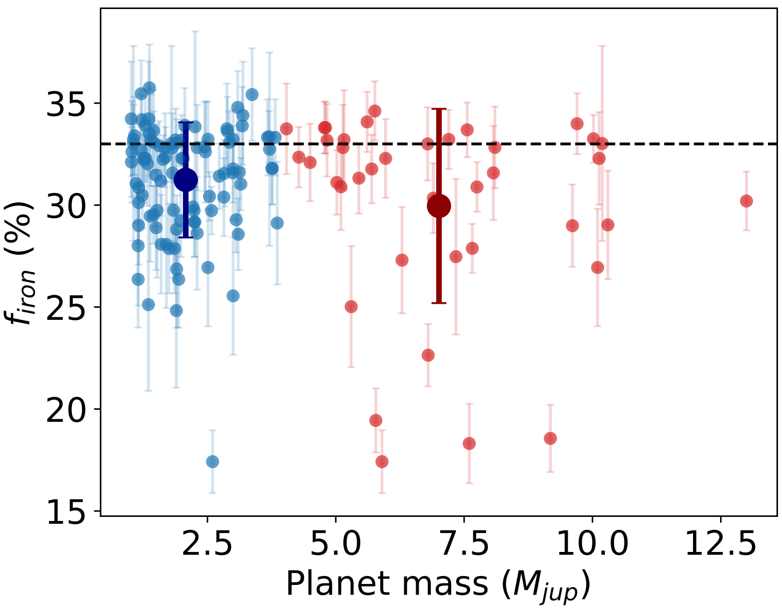

Figure 5.4: f_{iron} - iron-to-silicate mass fraction for each planetary mass regime ($M_{pl} < 4M_{jup}$) (blue) and ($M_{pl} > 4M_{jup}$) (red) vs the planetary mass. The mean and standard deviation of each group is shown in large symbols. The dashed line marks the f_{iron} value for our Solar System.

Similar to f_{iron}, in Figures 5.5 and 5.6 we show the dependence of water mass fraction as a function of planetary mass. In Figure 5.5 we observe a correlation between the iron content and w_f given that the lower iron content corresponds to the higher water mass fraction. This is because at low iron abundances the stars are enhanced in O which contributes to the w_f. Figure 5.6 and Table 5.1 show that the water mass fraction of the disks where the massive and super-massive planets are formed are similar, considering the dispersions of the distributions of w_f.

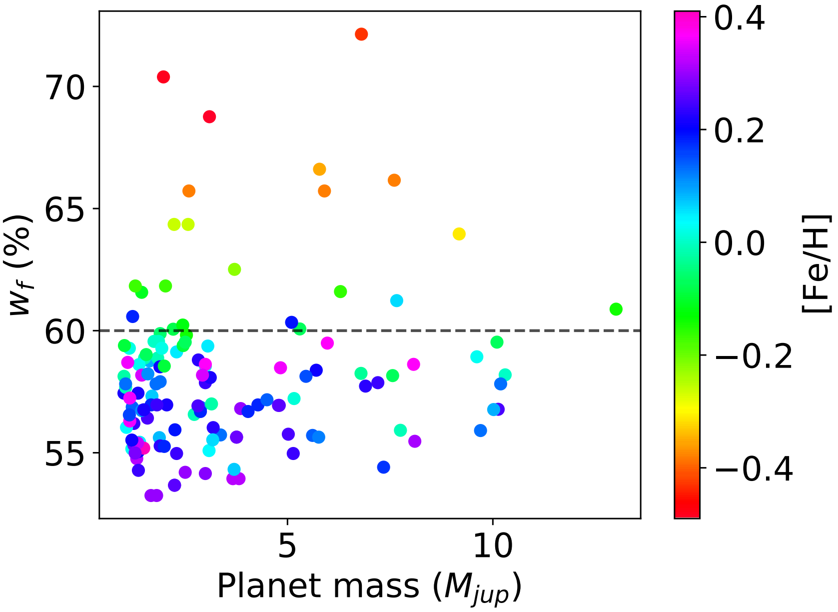

Figure 5.5: w_f - water mass fraction vs the planetary mass color coded to the metallicity [Fe/H]. The dashed line shows the w_f value for the Solar System.

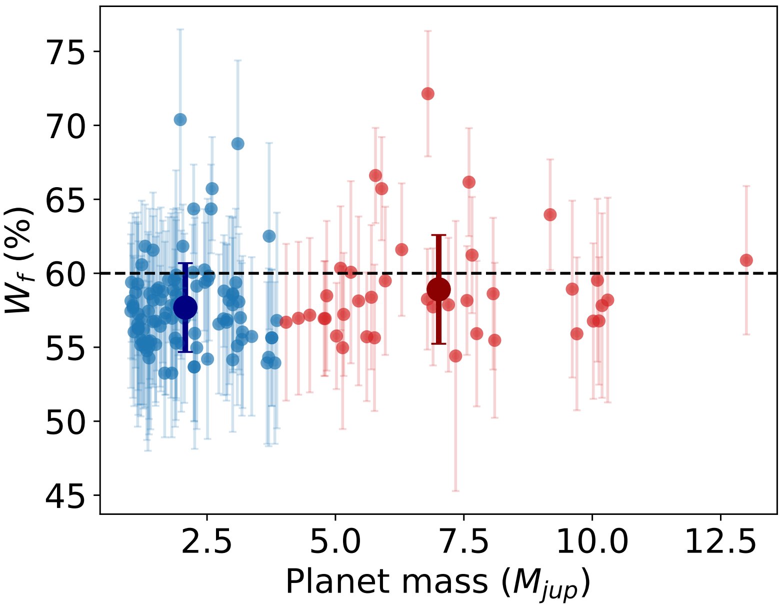

Figure 5.6: w_f - water mass fraction for each planetary mass regime ($M_{pl} < 4M_{jup}$) (blue) and ($M_{pl} > 4M_{jup}$) (red) vs the planetary mass. The mean and standard deviation of each group is shown in large symbols. The dashed line marks the w_f value for our Solar System.

In summary, despite these parameters not being the primary ones for our study, they give us interesting information about the potential composition of the disks where the giants and super-Jupiters of our sample were formed. We also learn that the iron and water mass fractions are not significantly different in the two planetary mass regimes studied.

Planetary mass regimes	**Average**	**Standard deviation**
f_{iron}		
$1 < M_{pl} < 13M_{Jup}$	30.866	3.524
$M_{pl} < 4M_{Jup}$	31.235	2.821
$M_{pl} \geqslant 4M_{Jup}$	29.958	4.763
w_f		
$1 < M_{pl} < 13M_{Jup}$	58.039	3.246
$M_{pl} < 4M_{Jup}$	57.684	3.002
$M_{pl} \geqslant 4M_{Jup}$	58.912	3.676
Z		
$1 < M_{pl} < 13M_{Jup}$	1.871	0.612
$M_{pl} < 4M_{Jup}$	1.887	0.634
$M_{pl} \geqslant 4M_{Jup}$	1.831	0.559
Z x $M_{\star}$		
$1 < M_{pl} < 13M_{Jup}$	2.339	0.909
$M_{pl} < 4M_{Jup}$	2.306	0.905
$M_{pl} \geqslant 4M_{Jup}$	2.421	0.925

Table 5.1: Average values and standard deviation for the iron-to-silicate mass fraction, water mass fractions and summed mass of all heavy metals relevant to planetary building blocks in different planetary masses regimes

Regarding the main objective of the study, we shall now evaluate the summed mass percentage of all heavy elements relevant for the planetary building blocks. In order to do so, we can examine the Figures 5.7 and 5.8 and Table 5.1 for a visual and quantitative analysis.

Starting with the visual representation, we see that almost all of the sample stars have Z values higher than the solar system (dashed lines). From Figure 5.7 we clearly see a stratification behaviour with metallicity, the higher the Z the higher the iron content. This dependence is seen, in both planetary mass regimes. The determination of Z takes into account the iron content, but also the rest of the metals, whose abundances also correlate, so the stratification is expected.

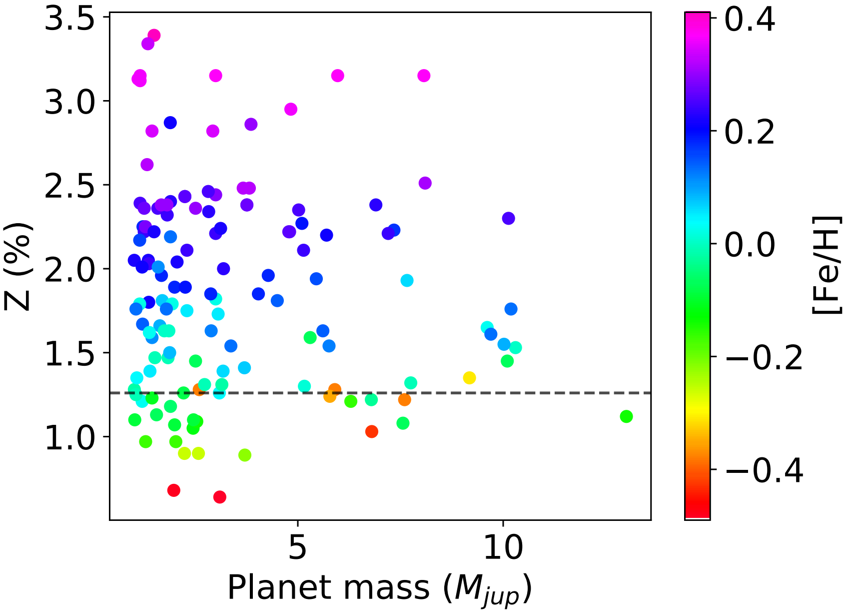

Figure 5.7: Z - the summed mass percent of all heavy elements expected for the planetary building blocks vs the planetary mass color coded to the metallicity [Fe/H]. The dashed line shows the Z value for the Solar System.

From figure 5.8, we notice that for the giant planets, the Z range is larger than for their higher mass counterparts ($M_{pl} \geqslant 4M_{jup}$). We also detect that the lower mass giant planets can start to form at Z $\sim$ 0.6% while super-Jupiters start at Z $\sim$ 1%, which may suggest that super-giants start to form in metal richer environments. This statement alone, points toward their formation scenario being CA, given that a certain amount of metals is needed to initiate their formation. We remind that, the CA paradigm suggests a correlation between giant planet formation and metallicity, as in, the more massive giants planets are formed in more metallic environments. However, we notice that there is not an increase in the Z as the planetary mass rises, for instance the highest mass planet in the sample actually has sob-solar metal content. It is perhaps important to note that while CA requires a minimum amount of metals for the giant plant formation to start, the model does not predict a strong correlation between the mass of planets and metallicity (e.g Mordasini et al., 2012). Table 5.1 shows that the mean Z content in the protoplanetary disks of giant and super-giant planets is similar.

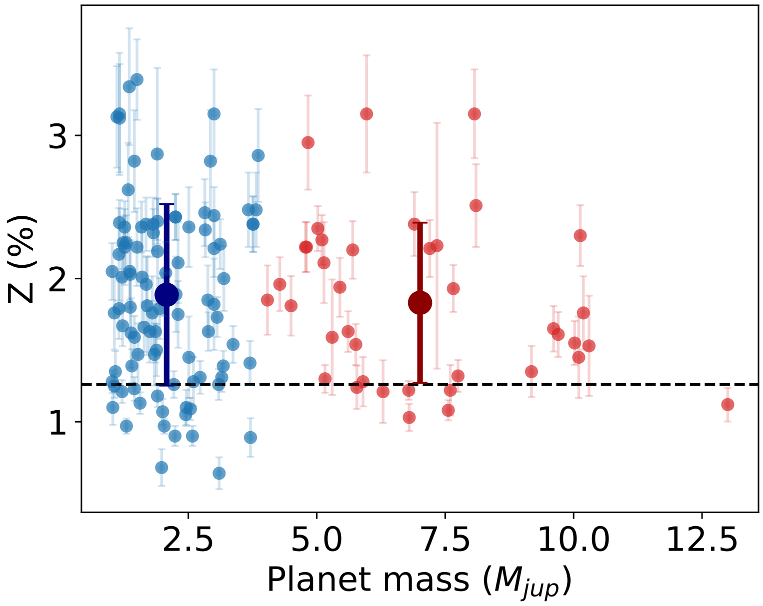

Figure 5.8: Z- the summed mass percent of all heavy elements expected for the planetary building blocks for each planetary mass regime ($M_{pl} < 4M_{jup}$) (blue) and ($M_{pl} > 4M_{jup}$) (red) vs the planetary mass. The mean and standard deviation of each group is shown in large symbols. The dashed line marks the Z value for our Solar System.

Because the disk mass (which correlates with the stellar mass) is also expected to play an important role for the formation of giant planets, in the Figure 5.9, we show dependence of the stellar masses as a function of planetary mass. We see that massive planets hosts are on average more massive than hosts of planets with masses below 4 M_{jup}. This plot is relevant given the fact that the total amount of metals in the disk depends on the mass of the disk.

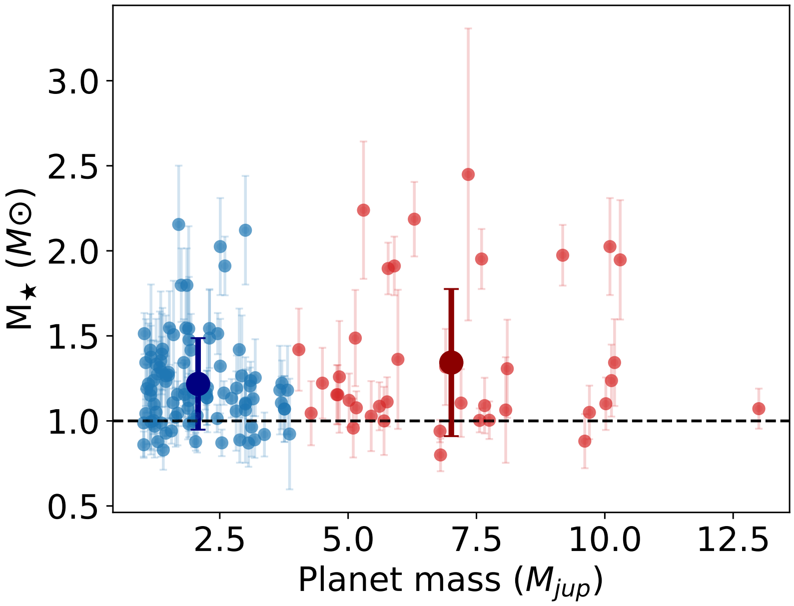

Figure 5.9: Masses of the planet hosts vs planet mass for giant ($M_{pl} < 4M_{jup}$) (blue) and super-giant ($M_{pl} > 4M_{jup}$) (red) planets. The blue and red large circles show the mean stellar masses of the two populations. The dashed line represents the solar mass.

Since both Z and stellar mass (as a proxy of disk mass) play a role for the formation of giant planets, in Figure 5.10 we show the dependence of $Z \times M_\star$ as a function of planetary mass. The multiplication of stellar mass and heavy element fraction should give a parameter proportional to the total amount of metals in the disks. We notice, that some of the planets that previously were below the solar system value, no longer are, given the high mass of their star. Analysing the mean $Z \times M_\star$ for each planetary mass regime, we realise they are similar. The mean values of the total amount of metals in the disk ($Z \times M_\star$) for super-Jupiters and Jupiter-like planets are very similar (see Table 5.1), being indistinguishable from statistical point of view.

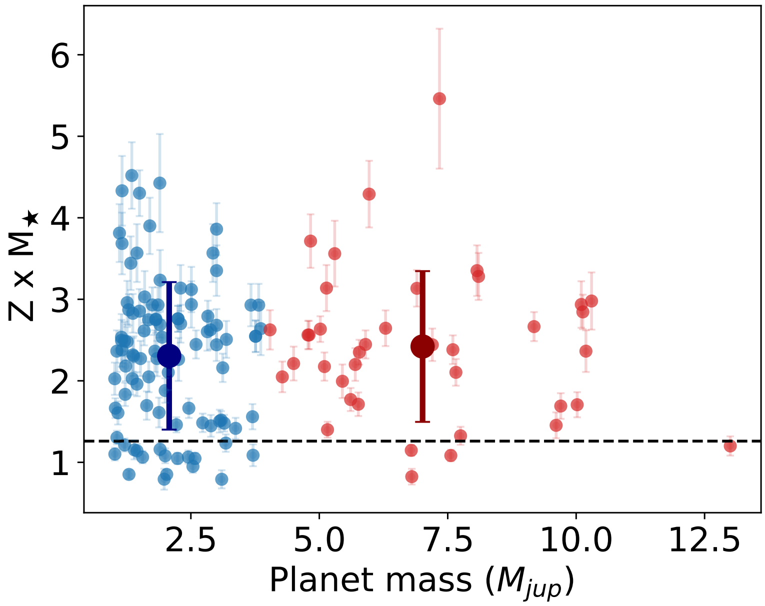

Figure 5.10: Total amount of metals ($Z \times M_\star$) in the protoplanetary disks as a function of planetary mass for giant ($M_{pl} < 4M_{jup}$) (blue) and super-giant planets ($M_{pl} > 4M_{jup}$) (red). The mean and standard deviation of each group is shown in large symbols. The dashed line marks the $Z \times M_\star$ value for our Solar System.

None of the characteristics examined above appear to demonstrate a significant variation in behavior across the planetary mass regimes examined, indicating that similar formation scenarios are likely. However, some super-massive planets appear to be formed in disks with less amount of metals than our Solar System planets. In the next section we analysed these systems further to understand whether there is something that distinguishes these planets from the rest of the sample.

5.2.1 Super-massive planets in disks with low metal content

Star HD	**Teff (K)**	**log g (dex)**	**[Fe/H] (dex)**	$\boldsymbol{V_{tur}}$ ($\boldsymbol{kms^{-1}}$)	**Z (%)**	$\boldsymbol{W_f}$ **(%)**	$\boldsymbol{f_{iron}}$ **(%)**	$\boldsymbol{m\sin(I)}$ ($\boldsymbol{M_{jup}}$)	$\boldsymbol{M_\star}$ ($\boldsymbol{M_\odot}$)	**orbital period (days)**	**Semi-Major Axis (AU)**	**Star type**
106252	5871	4.196	-0.07	1.10	1.08	58.16	33.69	7.56	1.003	1600	2.7	G0
111232	5460	4.406	-0.43	0.62	1.03	72.14	22.64	6.80	0.800	1143	1.97	G8V
11977	5067	3.039	-0.16	1.59	1.21	61.60	27.30	6.29	2.186	711	1.89	G8.5 III
217786A	5966	4.129	-0.14	1.12	1.12	60.88	30.20	13.0	1.072	1319	2.38	F8V
5583	4986	3.03	-0.35	1.62	1.24	66.61	19.44	5.78	1.896	139	0.53	K0
5891	4825	2.843	-0.38	1.69	1.22	66.16	18.31	7.60	1.952	177	0.76	G5D
98649	5714	4.247	-0.03	1.01	1.22	58.25	33.00	6.79	0.940	6023	6.57	G4V

Table 5.2: Properties of the systems containing super-massive planets ($M_{pl} > 4M_{jup}$) that have lower Z than the solar system.

In this section we examine the super-massive planets ($M_{pl} > 4M_{jup}$) host stars that have summed mass of all heavy elements relevant for planetary building blocks bellow the solar system value (Z = 1.26%). Some of the most prevalent characteristics are listed in Table 5.2. Below we provide some further discussion of each star and planet from literature. All of the planets in the Table 5.2 were detected through RV method.

HD 106252 is a yellow dwarf star. Since the inclination of the planetary orbit is known for the system, the true mass of the planet can be determined: $32.86^{+39.46}_{-25.3}$. Given the high mass of the object it is most likely a brown dwarf as expressed in the work of Reffert and Quirrenbach (2011).

HD 111232 is an G-type main sequence star that is iron-poor, giants planets surrounding such stars are remarkably uncommon. This star in the Hipparcos catalogue (E.S.A., 1997), is a suggested binary, however no stellar companion was discovered (Mayor et al., 2004).

HD 11977, also commonly known as Eta2 Hydri is a cool evolved giant star, that was probably an A type main sequence star (Setiawan et al., 2005).

HD 217786A belongs to a binary system where it is the primary star. It is an F-type main sequence star, and its orbiting planet minimum mass is 13 M_{jup}, which corresponds to the overlaping zone among giant planets and brown dwarfs (Moutou et al., 2011). The true mass of this planet is unknown and it is difficult to firmly conclude about the planetary nature of this object, although it is more probably a BD.

HD 5583 is an evolved metal-poor red giant and whose orbiting giant planet can be classified has a warm Jupiter (Huang et al., 2016) from its proximity to the host (Niedzielski et al., 2016). In the work of Andreasen et al. (2017) the $\log g$ obtained was higher that in the work of Niedzielski et al. (2016), which influences the mass derived by 15%, making the new minimum mass $m\sin(i) = 8.63M_{jup}$. The mass used for this work is the one listed in the Exoplanet.eu database of $m\sin(i) = 5.78M_{jup}$, as expressed in the Table 5.2. Regardless of the mass, almost all of the possible inclinations still leave the object within the planetary regime (Andreasen et al., 2017).

HD 5891 is a metal-poor giant star. HD 5891b orbital period is relatively small and has a short semi-major axis, which can be classified as a warm Jupiter (Huang et al., 2016). Interestingly, the metallicity estimation of this star by Johnson et al. (2011) is significantly different (-0.02 vs -0.38) from the one we extracted from SWEET-Cat. It is relevant to note that if the Mg, Si, C and O abundances were calculated from the aforementioned low metallicity, the results obtained would be different. In consequence, the Z calculated would also be influenced, most likely leaving the star above the solar system Z value.

HD 98649 is a solar-like dwarf star. The jupiter mass companion has a very eccentric orbit (e = 0.85) with a period of 14 years, this planet is one of the most eccentric planets known with a period larger than 600 days (Marmier et al., 2013).

5.2.2 Kolmogov-Smirkov test

The final step is to analyse statistically the sample. In order to do so, we will be preforming a Kolmogov-Smirkov (KS) test, that is a statistical test that allows for the comparison of two samples by quantifying the distance between their cumulative distribution functions. The closer to 1 the KS p-value is, the higher the probability the samples come from the same parent population. The p-values small than 0.05 is usually considered as a rejection of the null hypothesis that the two samples have the same parent distribution.

We compared the distributions of Z and $Z \times M_\bigstar$ of stars hosting massive and super-massive planets, as well as we compared their distributions with the HARPS field stars without planets (HSWNP) from Adibekyan et al. (2012). The KS statistics and p-values are displayed in the Table 5.3, for the Z values obtained for each set of data studied and for the $Z \times M_\bigstar$ for planet host stars only.

Samples	**KS statistic**	**KS p-value**
$M_{pl} \geqslant 4$ vs HSWNP (Z)	0.465	7.366e-08
$M_{pl} < 4$ vs HSWNP (Z)	0.419	4.885e-14
$M_{pl} < 4$ vs $M_{pl} \geqslant 4$ (Z)	0.143	0.568
$M_{pl} < 4M_{jup}$ vs $M_{pl} \geqslant 4M_{jup}$ $(Z \times M_\bigstar)$	0.133	0.652

Table 5.3: Results of the KS test comparing the Z and $Z \times M_\bigstar$ values obtained for our sample stars with planets above and below $4M_{jup}$ and stars without planets (HSWNP). The comparison of $Z \times M_\bigstar$ is done only for systems with detected planets.

From Table 5.3 we see that that the HARPS stars with no planets (HSWNP) and the hosts of massive-Jupiters ($M_{pl} \geqslant 4M_{jup}$) do not appear to come from the same parent distribution given such low p-value of the KS test. This KS p-value is even smaller when this HSWNP is compared with the giant planets hosts ($M_{pl} < 4M_{jup}$), once again reinforcing that they most likely come from different parent distribution. When the distribution of Z of giant planets is compared with the hosts of massive planets, the KS p-value is very high, giving us a greater evidence for one single population. Finally, when the metallicity $(Z \times M_\bigstar)$ is compared between our sample stars above and bellow $4M_{jup}$ we again obtain a large KS p-value, which lets us know, once again, that the populations are not statically different.

Chapter 6

Conclusion

In this thesis we intended to understand whether or not super-massive planets with masses above 4 M_{jup} could have been formed through core-accretion. The question came to be from the recent works which suggested a break-point mass at $4M_{jup}$ above which planet formation stopped being ruled by core-accretion and GI became the dominant process. In these studies they make use of the well-known relationship between giant planet occurrence and metallicity, where giant planets formation increases exponentially with the metallicity in the disk. This relation is predicted by CA. However in these works, the hosts of planets above $4M_{jup}$, were not as metal rich as predicted in CA. In fact, the most super-massive planets had metal-poor hosts, which is against the predictions of CA. Alternatively, GI paradigm of massive planet formation does not predict a clear relation between massive planet formation and metallicity, making it the favorable process for the formation of these planets. On the other hand, posterior works, that employed different analysis, did not support the previous claims that a separation in mass would reveal two different giant planet populations with different formation channels.

In all these aforementioned works, the iron content was used as a proxy for the overall metallicity of the stars. This approximation is valid for solar-type stars, but for metal-poor stars, there is usually an increase in α elements that needs to be taken into account. The enhancement in α elements could compensate for the lack of iron in the star, possibly being sufficient to have these planets being formed through CA.

In this thesis, we performed a spectroscopic analysis to overcome the aforementioned issues and determine the total amount of metals in the disks where the giant planets are formed. From the exoplanet.eu database we selected planets with masses between 1 and 13 M_{jup}. We then restricted the sample to hosts with temperatures between 4700K and 6400K. Then we selected those hosts for which there were publicly available HARPS or HARPS-N spectra with a signal-to-noise ratio greater than 200. Our sample consisted of 113 FGK-type stars hosting 39 planets with masses bellow $4M_{jup}$ and 96 planets with masses above $4M_{jup}$.

For the selected sample stars we derived spectroscopically the abundances of Mg and Si, used tabulated values of Fe from SWEET-Cat and adopted a ML algorithm for the prediction of the abundances of C and O. Based on these chemical abundances and using a simple stoichiometric model, we obtained the mass fraction of all the heavy elements (Z) relevant for the formation of planets.

We compared the distributions of Z of stars hosting massive and super-massive planets and found no significant different as evaluated by a KS statistical test. We found that almost all of the stars hosting super-massive planets in the sample have Z above the solar system value, which could imply that their formation is still possible to explain with CA. When we multiply the Z with the stellar mass, getting the percentage of heavy metals per solar mass, there remains fewer massive-Jupiters with sub-solar $Z \times M_\bigstar$ values. This $Z \times M_\bigstar$ parameter is thought to be proportional to the total metal content in the protoplanetary disks where the planets were formed. When this parameter is compared between Jupiter-like and super-Jupiters planets, there is no statistical difference.

We investigated all the super-massive planet hosting stars individually to understand whether these systems show any peculiarity when compared with the rest of the sample planets. No clear pattern was found. We suggest that these super-massive planets with sub-solar $Z \times M_\bigstar$, could have had different formation scenarios from the rest, but we do not disregard they might have had been formed via CA.

Unfortunately, currently there are no available models of massive planet formations around massive stars. The comparison of our results with the predictions of population synthesis based on the GI and CA models could help to conclude whether giant planet formation can be explained by any of these models for the whole spectrum of planetary masses.

Bibliography

Acquaviva, V. (2016). How to measure metallicity from five-band photometry with supervised machine learning algorithms. MNRAS, 456(2):1618–1626.

Adibekyan, V. (2019). Heavy Metal Rules. I. Exoplanet Incidence and Metallicity. *Geosciences*, 9(3):105.

Adibekyan, V., Delgado-Mena, E., Figueira, P., Sousa, S. G., Santos, N. C., González Hernández, J. I., Minchev, I., Faria, J. P., Israelian, G., Harutyunyan, G., Suárez-Andrés, L., and Hakobyan, A. A. (2016). Abundance trend with condensation temperature for stars with different Galactic birth places. A&A, 592:A87.

Adibekyan, V., Dorn, C., Sousa, S. G., Santos, N. C., Bitsch, B., Israelian, G., Mordasini, C., Barros, S. C. C., Delgado Mena, E., Demangeon, O. D. S., Faria, J. P., Figueira, P., Hakobyan, A. A., Oshagh, M., Soares, B. M. T. B., Kunitomo, M., Takeda, Y., Jofré, E., Petrucci, R., and Martioli, E. (2021). A compositional link between rocky exoplanets and their host stars. *arXiv e-prints*, page arXiv:2102.12444.

Adibekyan, V., Figueira, P., Santos, N. C., Sousa, S. G., Faria, J. P., Delgado-Mena, E., Oshagh, M., Tsantaki, M., Hakobyan, A. A., González Hernández, J. I., Suárez-Andrés, L., and Israelian, G. (2015a). Identifying the best iron-peak and α-capture elements for chemical tagging: The impact of the number of lines on measured scatter. A&A, 583:A94.

Adibekyan, V., Sousa, S. G., and Santos, N. C. (2018). Characterization of Exoplanet-Host Stars. In Campante, T. L., Santos, N. C., and Monteiro, M. J. P. F. G., editors, *Asteroseismology and Exoplanets: Listening to the Stars and Searching for New Worlds*, volume 49, page 225.

Adibekyan, V. Z., Benamati, L., Santos, N. C., Alves, S., Lovis, C., Udry, S., Israelian, G., Sousa, S. G., Tsantaki, M., Mortier, A., Sozzetti, A., and De Medeiros, J. R. (2015b). Chemical abundances and kinematics of 257 G-, K-type field giants. Setting a base for further analysis of giant-planet properties orbiting evolved stars. MNRAS, 450(2):1900–1915.

Adibekyan, V. Z., Figueira, P., Santos, N. C., Hakobyan, A. A., Sousa, S. G., Pace, G., Delgado Mena, E., Robin, A. C., Israelian, G., and González Hernández, J. I. (2013). Kinematics and chemical properties of the Galactic stellar populations. The HARPS FGK dwarfs sample. A&A, 554:A44.

Adibekyan, V. Z., Sousa, S. G., Santos, N. C., Delgado Mena, E., González Hernández, J. I., Israelian, G., Mayor, M., and Khachatryan, G. (2012). Chemical abundances of 1111 FGK stars from the HARPS GTO planet search program. Galactic stellar populations and planets. A&A, 545:A32.

BIBLIOGRAPHY

Ahumada, R., Prieto, C. A., Almeida, A., Anders, F., Anderson, S. F., Andrews, B. H., and et al. (2020). The 16th Data Release of the Sloan Digital Sky Surveys: First Release from the APOGEE-2 Southern Survey and Full Release of eBOSS Spectra. ApJS, 249(1):3.

Alibert, Y., Mordasini, C., Benz, W., and Winisdoerffer, C. (2005). Models of giant planet formation with migration and disc evolution. A&A, 434(1):343–353.

Allende Prieto, C. (2016). Solar and stellar photospheric abundances. *Living Reviews in Solar Physics*, 13(1):1.

Aller, L. H. and Greenstein, J. L. (1960). The Abundances of the Elements in G-Type Subdwarfs. ApJS, 5:139.

Alves, S., Benamati, L., Santos, N. C., Adibekyan, V. Z., Sousa, S. G., Israelian, G., De Medeiros, J. R., Lovis, C., and Udry, S. (2015). Determination of the spectroscopic stellar parameters for 257 field giant stars. MNRAS, 448(3):2749–2765.

Andreasen, D. T., Sousa, S. G., Tsantaki, M., Teixeira, G. D. C., Mortier, A., Santos, N. C., Suárez-Andrés, L., Delgado-Mena, E., and Ferreira, A. C. S. (2017). SWEET-Cat update and FASMA. A new minimization procedure for stellar parameters using high-quality spectra. A&A, 600:A69.

Asplund, M. (2005). New Light on Stellar Abundance Analyses: Departures from LTE and Homogeneity. ARA&A, 43(1):481–530.

Baraffe, I., Chabrier, G., and Barman, T. (2010). The physical properties of extra-solar planets. *Reports on Progress in Physics*, 73(1):016901.

Benz, W., Slattery, W. L., and Cameron, A. G. W. (1988). Collisional stripping of Mercury's mantle. Icarus, 74(3):516–528.

Bertran de Lis, S., Delgado Mena, E., Adibekyan, V. Z., Santos, N. C., and Sousa, S. G. (2015). Oxygen abundances in G- and F-type stars from HARPS. Comparison of [OI] 6300 Å and OI 6158 Å. A&A, 576:A89.

Bond, J. C., O'Brien, D. P., and Lauretta, D. S. (2010). The Compositional Diversity of Extrasolar Terrestrial Planets. I. In Situ Simulations. ApJ, 715(2):1050–1070.

Boss, A. P. (1998). Evolution of the Solar Nebula. IV. Giant Gaseous Protoplanet Formation. ApJ, 503(2):923–937.

Boss, A. P. (2002). Stellar Metallicity and the Formation of Extrasolar Gas Giant Planets. ApJ, 567(2):L149–L153.

Breiman, L. (2001). Random Forests. *Machine Learning*, 45:5–32.

Buchhave, L. A., Latham, D. W., Johansen, A., Bizzarro, M., Torres, G., Rowe, J. F., Batalha, N. M., Borucki, W. J., Brugamyer, E., Caldwell, C., Bryson, S. T., Ciardi, D. R., Cochran, W. D., Endl, M., Esquerdo, G. A., Ford, E. B., Geary, J. C., Gilliland, R. L., Hansen, T., Isaacson, H., Laird, J. B., Lucas, P. W., Marcy, G. W., Morse, J. A., Robertson, P., Shporer, A., Stefanik, R. P., Still, M., and Quinn, S. N. (2012). An abundance of small exoplanets around stars with a wide range of metallicities. Nature, 486(7403):375–377.

Caballero, J. A. (2018). A Review on Substellar Objects below the Deuterium Burning Mass Limit: Planets, Brown Dwarfs or What? *Geosciences*, 8(10):362.

Chabrier, G., Johansen, A., Janson, M., and Rafikov, R. (2014). Giant Planet and Brown Dwarf Formation. In Beuther, H., Klessen, R. S., Dullemond, C. P., and Henning, T., editors, *Protostars and Planets VI*, page 619.

Charbonneau, D., Brown, T. M., Latham, D. W., and Mayor, M. (2000). Detection of Planetary Transits Across a Sun-like Star. ApJ, 529(1):L45–L48.

Cosentino, R., Lovis, C., Pepe, F., Collier Cameron, A., Latham, D. W., Molinari, E., Udry, S., and et al. (2012). Harps-N: the new planet hunter at TNG. In McLean, I. S., Ramsay, S. K., and Takami, H., editors, *Ground-based and Airborne Instrumentation for Astronomy IV*, volume 8446 of *Society of Photo-Optical Instrumentation Engineers (SPIE) Conference Series*, page 84461V.

Cumming, A., Butler, R. P., Marcy, G. W., Vogt, S. S., Wright, J. T., and Fischer, D. A. (2008). The Keck Planet Search: Detectability and the Minimum Mass and Orbital Period Distribution of Extrasolar Planets. PASP, 120(867):531.

Deeg, H. and Garrido, R. (2002). Descubrir mundos en transito. *IAA: Información y Actualidade*, 7:3–5.

Delgado Mena, E., Adibekyan, V., Santos, N. C., Tsantaki, M., González Hernández, J. I., Sousa, S. G., and Bertrán de Lis, S. (2021). Chemical abundances of 1111 FGK stars from the HARPS GTO planet search program IV. Carbon and C/O ratios for Galactic stellar populations and planet hosts. *arXiv e-prints*, page arXiv:2109.04844.

Delgado Mena, E., Israelian, G., González Hernández, J. I., Bond, J. C., Santos, N. C., Udry, S., and Mayor, M. (2010). Chemical Clues on the Formation of Planetary Systems: C/O Versus Mg/Si for HARPS GTO Sample. ApJ, 725(2):2349–2358.

Dorn, C., Hinkel, N. R., and Venturini, J. (2017). Bayesian analysis of interiors of HD 219134b, Kepler-10b, Kepler-93b, CoRoT-7b, 55 Cnc e, and HD 97658b using stellar abundance proxies. A&A, 597:A38.

Dorn, C., Khan, A., Heng, K., Connolly, J. A. D., Alibert, Y., Benz, W., and Tackley, P. (2015). Can we constrain the interior structure of rocky exoplanets from mass and radius measurements? A&A, 577:A83.

Drake, M. J. and Righter, K. (2002). Determining the composition of the Earth. Nature, 416(6876):39–44.

Dressing, C. D., Charbonneau, D., Dumusque, X., Gettel, S., Pepe, F., Collier Cameron, A., Latham, D. W., Molinari, E., Udry, S., Affer, L., Bonomo, A. S., Buchhave, L. A., Cosentino, R., Figueira, P., Fiorenzano, A. F. M., Harutyunyan, A., Haywood, R. D., Johnson, J. A., Lopez-Morales, M., Lovis, C., Malavolta, L., Mayor, M., Micela, G., Motalebi, F., Nascimbeni, V., Phillips, D. F., Piotto, G., Pollacco, D., Queloz, D., Rice, K., Sasselov, D., Ségransan, D., Sozzetti, A., Szentgyorgyi, A., and Watson, C. (2015). The Mass of Kepler-93b and The Composition of Terrestrial Planets. ApJ, 800(2):135.

E.S.A. (1997). The hipparcos and tycho catalogues. *ESA SP-1200*.

Fischer, D. A. and Valenti, J. (2005). The Planet-Metallicity Correlation. ApJ, 622(2):1102–1117.

Fortney, J. J., Marley, M. S., and Barnes, J. W. (2007). Planetary Radii across Five Orders of Magnitude in Mass and Stellar Insolation: Application to Transits. ApJ, 659(2):1661–1672.

Fuhrmann, K. (1998). Nearby stars of the Galactic disk and halo. A&A, 338:161–183.

Gaia Collaboration, Prusti, T., de Bruijne, J. H. J., Brown, A. G. A., Vallenari, and et al. (2016). The Gaia mission. A&A, 595:A1.

Gonzalez, G. (1997). The stellar metallicity-giant planet connection. MNRAS, 285(2):403–412.

Guillot, T., Santos, N. C., Pont, F., Iro, N., Melo, C., and Ribas, I. (2006). A correlation between the heavy element content of transiting extrasolar planets and the metallicity of their parent stars. A&A, 453(2):L21–L24.

Gustafsson, B., Edvardsson, B., Eriksson, K., Jørgensen, U. G., Nordlund, Å., and Plez, B. (2008). A grid of MARCS model atmospheres for late-type stars. I. Methods and general properties. A&A, 486(3):951–970.

Hasegawa, Y. and Pudritz, R. E. (2014). Planet Traps and Planetary Cores: Origins of the Planet-Metallicity Correlation. ApJ, 794(1):25.

Henry, G. W., Marcy, G. W., Butler, R. P., and Vogt, S. S. (2000). A Transiting "51 Peg-like" Planet. ApJ, 529(1):L41–L44.

Holtzman, J. A., Shetrone, M., Johnson, J. A., Allende Prieto, C., Anders, F., Andrews, B., Beers, T. C., Bizyaev, D., Blanton, M. R., Bovy, J., Carrera, R., Chojnowski, S. D., Cunha, K., Eisenstein, D. J., Feuillet, D., Frinchaboy, P. M., Galbraith-Frew, J., García Pérez, A. E., García-Hernández, D. A., Hasselquist, S., Hayden, M. R., Hearty, F. R., Ivans, I., Majewski, S. R., Martell, S., Meszaros, S., Muna, D., Nidever, D., Nguyen, D. C., O'Connell, R. W., Pan, K., Pinsonneault, M., Robin, A. C., Schiavon, R. P., Shane, N., Sobeck, J., Smith, V. V., Troup, N., Weinberg, D. H., Wilson, J. C., Wood-Vasey, W. M., Zamora, O., and Zasowski, G. (2015). Abundances, Stellar Parameters, and Spectra from the SDSS-III/APOGEE Survey. AJ, 150(5):148.

Huang, C., Wu, Y., and Triaud, A. H. M. J. (2016). Warm Jupiters Are Less Lonely than Hot Jupiters: Close Neighbors. ApJ, 825(2):98.

Ida, S. and Lin, D. N. C. (2004a). Toward a Deterministic Model of Planetary Formation. I. A Desert in the Mass and Semimajor Axis Distributions of Extrasolar Planets. ApJ, 604(1):388–413.

Ida, S. and Lin, D. N. C. (2004b). Toward a Deterministic Model of Planetary Formation. II. The Formation and Retention of Gas Giant Planets around Stars with a Range of Metallicities. ApJ, 616(1):567–572.

Ikoma, M., Nakazawa, K., and Emori, H. (2000). Formation of Giant Planets: Dependences on Core Accretion Rate and Grain Opacity. ApJ, 537(2):1013–1025.

Israelian, G., Santos, N. C., Mayor, M., and Rebolo, R. (2001). Evidence for planet engulfment by the star HD82943. Nature, 411(6834):163–166.

Jofré, P., Heiter, U., and Soubiran, C. (2019). Accuracy and Precision of Industrial Stellar Abundances. ARA&A, 57:571–616.

Johnson, J. A., Aller, K. M., Howard, A. W., and Crepp, J. R. (2010). Giant Planet Occurrence in the Stellar Mass-Metallicity Plane. PASP, 122(894):905.

Johnson, J. A., Clanton, C., Howard, A. W., Bowler, B. P., Henry, G. W., Marcy, G. W., Crepp, J. R., Endl, M., Cochran, W. D., MacQueen, P. J., Wright, J. T., and Isaacson, H. (2011). Retired A Stars and Their Companions. VII. 18 New Jovian Planets. ApJS, 197(2):26.

Johnson, T. V., Mousis, O., Lunine, J. I., and Madhusudhan, N. (2012). Planetesimal Compositions in Exoplanet Systems. ApJ, 757(2):192.

Jönsson, H., Holtzman, J. A., Allende Prieto, C., Cunha, K., García-Hernández, D. A., Hasselquist, S., Masseron, T., Osorio, Y., Shetrone, M., Smith, V., Stringfellow, G. S., Bizyaev, D., Edvardsson, B., Majewski, S. R., Mészáros, S., Souto, D., Zamora, O., Beaton, R. L., Bovy, J., Donor, J., Pinsonneault, M. H., Poovelil, V. J., and Sobeck, J. (2020). APOGEE Data and Spectral Analysis from SDSS Data Release 16: Seven Years of Observations Including First Results from APOGEE-South. AJ, 160(3):120.

Khan, A. and Connolly, J. A. D. (2008). Constraining the composition and thermal state of Mars from inversion of geophysical data. *Journal of Geophysical Research (Planets)*, 113(E7):E07003.

Kuiper, G. P. (1951). On the Origin of the Solar System. *Proceedings of the National Academy of Science*, 37(1):1–14.

Kurucz, R. (1993). ATLAS9 Stellar Atmosphere Programs and 2 km/s grid. *ATLAS9 Stellar Atmosphere Programs and 2 km/s grid. Kurucz CD-ROM No. 13. Cambridge*, 13.

Lindegren, L. and Dravins, D. (2003). The fundamental definition of “radial velocity”. A&A, 401:1185–1201.

Lissauer, J. J. (1993). Planet formation. ARA&A, 31:129–174.

Lodders, K. (2003). Solar System Abundances and Condensation Temperatures of the Elements. ApJ, 591(2):1220–1247.

Majewski, S. R., APOGEE Team, and APOGEE-2 Team (2016). The Apache Point Observatory Galactic Evolution Experiment (APOGEE) and its successor, APOGEE-2. *Astronomische Nachrichten*, 337(8-9):863.

Majewski, S. R., Schiavon, R. P., Frinchaboy, P. M., Allende Prieto, C., Barkhouser, R., Bizyaev, D., Blank, B., Brunner, S., Burton, A., and et al. (2017). The Apache Point Observatory Galactic Evolution Experiment (APOGEE). AJ, 154(3):94.

Marmier, M., Ségransan, D., Udry, S., Mayor, M., Pepe, F., Queloz, D., Lovis, C., Naef, D., Santos, N. C., Alonso, R., Alves, S., Berthet, S., Chazelas, B., Demory, B. O., Dumusque, X., Eggenberger, A., Figueira, P., Gillon, M., Hagelberg, J., Lendl, M., Mardling, R. A., Mégevand, D., Neveu, M., Sahlmann, J., Sosnowska, D., Tewes, M., and Triaud, A. H. M. J. (2013). The CORALIE survey for southern extrasolar planets. XVII. New and updated long period and massive planets. A&A, 551:A90.

Marois, C., Zuckerman, B., Konopacky, Q. M., Macintosh, B., and Barman, T. (2010). Images of a fourth planet orbiting HR 8799. Nature, 468(7327):1080–1083.

Márquez-Neila, P., Fisher, C., Sznitman, R., and Heng, K. (2018). Supervised machine learning for analysing spectra of exoplanetary atmospheres. *Nature Astronomy*, 2:719–724.

Mayor, M., Lovis, C., and Santos, N. C. (2014). Doppler spectroscopy as a path to the detection of Earth-like planets. Nature, 513(7518):328–335.

Mayor, M., Pepe, F., Queloz, D., Bouchy, F., Rupprecht, G., Lo Curto, G., Avila, G., Benz, W., Bertaux, J. L., Bonfils, X., Dall, T., Dekker, H., Delabre, B., Eckert, W., Fleury, M., Gilliotte, A., Gojak, D., Guzman, J. C., Kohler, D., Lizon, J. L., Longinotti, A., Lovis, C., Megevand, D., Pasquini, L., Reyes, J., Sivan, J. P., Sosnowska, D., Soto, R., Udry, S., van Kesteren, A., Weber, L., and Weilenmann, U. (2003). Setting New Standards with HARPS. *The Messenger*, 114:20–24.

Mayor, M. and Queloz, D. (1995). A Jupiter-mass companion to a solar-type star. Nature, 378(6555):355–359.

Mayor, M., Udry, S., Naef, D., Pepe, F., Queloz, D., Santos, N. C., and Burnet, M. (2004). The CORALIE survey for southern extra-solar planets. XII. Orbital solutions for 16 extra-solar planets discovered with CORALIE. A&A, 415:391–402.

McDonough, W. F. and Sun, S. s. (1995). The composition of the Earth. *Chemical Geology*, 120(3-4):223–253.

McWilliam, A. (1997). Abundance Ratios and Galactic Chemical Evolution. ARA&A, 35:503–556.

Miller, A. A. (2015). VizieR Online Data Catalog: Machine learning metallicity predictions using SDSS (Miller, 2015). *VizieR Online Data Catalog*, page J/ApJ/811/30.

Mordasini, C., Alibert, Y., Benz, W., Klahr, H., and Henning, T. (2012). Extrasolar planet population synthesis . IV. Correlations with disk metallicity, mass, and lifetime. A&A, 541:A97.

Mordasini, C., Klahr, H., Alibert, Y., Miller, N., and Henning, T. (2014). Grain opacity and the bulk composition of extrasolar planets. I. Results from scaling the ISM opacity. A&A, 566:A141.

Mortier, A., Santos, N. C., Sousa, S., Israelian, G., Mayor, M., and Udry, S. (2013). On the functional form of the metallicity-giant planet correlation. A&A, 551:A112.

Mortier, A., Sousa, S. G., Adibekyan, V. Z., Brandão, I. M., and Santos, N. C. (2014). Correcting the spectroscopic surface gravity using transits and asteroseismology. No significant effect on temperatures or metallicities with ARES and MOOG in local thermodynamic equilibrium. A&A, 572:A95.

Moutou, C., Mayor, M., Lo Curto, G., Ségransan, D., Udry, S., Bouchy, F., Benz, W., Lovis, C., Naef, D., Pepe, F., Queloz, D., Santos, N. C., and Sousa, S. G. (2011). The HARPS search for southern extra-solar planets. XXVII. Seven new planetary systems. A&A, 527:A63.

Murray, N., Chaboyer, B., Arras, P., Hansen, B., and Noyes, R. W. (2001). Stellar Pollution in the Solar Neighborhood. ApJ, 555(2):801–815.

Nayakshin, S. (2014). Differentiation of silicates and iron during formation of Mercury and high-density exoplanets. MNRAS, 441(2):1380–1390.

Nayakshin, S. (2016). Tidal Downsizing model - IV. Destructive feedback in planets. MNRAS, 461(3):3194–3211.

Nayakshin, S. (2017). Dawes Review 7: The Tidal Downsizing Hypothesis of Planet Formation. PASA, 34:e002.

Nayakshin, S., Cha, S.-H., and Bridges, J. C. (2011). The tidal downsizing hypothesis for planet formation and the composition of Solar system comets. MNRAS, 416(1):L50–L54.

Nesvorný, D. and Morbidelli, A. (2008). Mass and Orbit Determination from Transit Timing Variations of Exoplanets. ApJ, 688(1):636–646.

Niedzielski, A., Villaver, E., Nowak, G., Adamów, M., Kowalik, K., Wolszczan, A., Deka-Szymankiewicz, B., Adamczyk, M., and Maciejewski, G. (2016). Tracking Advanced Planetary Systems (TAPAS) with HARPS-N. III. HD 5583 and BD+15 2375 - two cool giants with warm companions. A&A, 588:A62.

Nissen, P. E. and Gustafsson, B. (2018). High-precision stellar abundances of the elements: methods and applications. A&A Rev., 26(1):6.

Perryman, M., Hartman, J., Bakos, G. Á., and Lindegren, L. (2014). Astrometric Exoplanet Detection with Gaia. ApJ, 797(1):14.

Pollack, J. B., Hubickyj, O., Bodenheimer, P., Lissauer, J. J., Podolak, M., and Greenzweig, Y. (1996). Formation of the Giant Planets by Concurrent Accretion of Solids and Gas. Icarus, 124(1):62–85.

Rebolo, R., Zapatero Osorio, M. R., Béjar, V. J. S., Barrado Y Navascués, D., Bailer-Jones, C., Mundt, R., and Martín, E. L. (2000). Very Young Free-Floating Planets in the σ Orionis Star Cluster (Contributed Talk). In Garzón, G., Eiroa, C., de Winter, D., and Mahoney, T. J., editors, *Disks, Planetesimals, and Planets*, volume 219 of *Astronomical Society of the Pacific Conference Series*, page 515.

Recio-Blanco, A., de Laverny, P., Kordopatis, G., Helmi, A., Hill, V., Gilmore, G., Wyse, R., Adibekyan, V., Randich, S., Asplund, M., Feltzing, S., Jeffries, R., Micela, G., Vallenari, A., Alfaro, E., Allende Prieto, C., Bensby, T., Bragaglia, A., Flaccomio, E., Koposov, S. E., Korn, A., Lanzafame, A., Pancino, E., Smiljanic, R., Jackson, R., Lewis, J., Magrini, L., Morbidelli, L., Prisinzano, L., Sacco, G., Worley, C. C., Hourihane, A., Bergemann, M., Costado, M. T., Heiter, U., Joffre, P., Lardo, C., Lind, K., and Maiorca, E. (2014). The Gaia-ESO Survey: the Galactic thick to thin disc transition. A&A, 567:A5.

Reddy, B. E., Lambert, D. L., and Allende Prieto, C. (2006). Elemental abundance survey of the Galactic thick disc. MNRAS, 367(4):1329–1366.

Reffert, S. and Quirrenbach, A. (2011). Mass constraints on substellar companion candidates from the re-reduced Hipparcos intermediate astrometric data: nine confirmed planets and two confirmed brown dwarfs. A&A, 527:A140.

Russell, D. (2013). Geophysical Classification of Planets, Dwarf Planets, and Moons. *arXiv e-prints*, page arXiv:1308.0616.

Russell, D. G. (2021). On the Need for a Classification System for Consistent Characterization of the Composition of Planetary Bodies. *arXiv e-prints*, page arXiv:2108.03343.

Sanloup, C., Jambon, A., and Gillet, P. (1999). A simple chondritic model of Mars. *Physics of the Earth and Planetary Interiors*, 112(1-2):43–54.

Santos, N. C., Adibekyan, V., Dorn, C., Mordasini, C., Noack, L., Barros, S. C. C., Delgado-Mena, E., Demangeon, O., Faria, J. P., Israelian, G., and Sousa, S. G. (2017a). Constraining planet structure and composition from stellar chemistry: trends in different stellar populations. A&A, 608:A94.

Santos, N. C., Adibekyan, V., Figueira, P., Andreasen, D. T., Barros, S. C. C., Delgado-Mena, E., Demangeon, O., Faria, J. P., Oshagh, M., Sousa, S. G., Viana, P. T. P., and Ferreira, A. C. S. (2017b). Observational evidence for two distinct giant planet populations. A&A, 603:A30.

Santos, N. C., Adibekyan, V., Mordasini, C., Benz, W., Delgado-Mena, E., Dorn, C., Buchhave, L., Figueira, P., Mortier, A., Pepe, F., Santerne, A., Sousa, S. G., and Udry, S. (2015). Constraining planet structure from stellar chemistry: the cases of CoRoT-7, Kepler-10, and Kepler-93. A&A, 580:L13.

Santos, N. C., Israelian, G., and Mayor, M. (2001). The metal-rich nature of stars with planets. A&A, 373:1019–1031.

Santos, N. C., Israelian, G., and Mayor, M. (2004). Spectroscopic [Fe/H] for 98 extra-solar planet-host stars. Exploring the probability of planet formation. A&A, 415:1153–1166.

Santos, N. C., Sousa, S. G., Mortier, A., Neves, V., Adibekyan, V., Tsantaki, M., Delgado Mena, E., Bonfils, X., Israelian, G., Mayor, M., and Udry, S. (2013a). SWEET-Cat: A catalogue of parameters for Stars With ExoplanETs. I. New atmospheric parameters and masses for 48 stars with planets. A&A, 556:A150.

Santos, N. C., Sousa, S. G., Mortier, A., Neves, V., Adibekyan, V., Tsantaki, M., Delgado Mena, E., Bonfils, X., Israelian, G., Mayor, M., and Udry, S. (2013b). VizieR Online Data Catalog: SWEETCat I. Stellar parameters for host stars (Santos+, 2013). *VizieR Online Data Catalog*, pages J/A+A/556/A150.

Saumon, D., Hubbard, W. B., Burrows, A., Guillot, T., Lunine, J. I., and Chabrier, G. (1996). A Theory of Extrasolar Giant Planets. ApJ, 460:993.

Schlaufman, K. C. (2018). Evidence of an Upper Bound on the Masses of Planets and Its Implications for Giant Planet Formation. ApJ, 853(1):37.

Schneider, J., Dedieu, C., Le Sidaner, P., Savalle, R., and Zolotukhin, I. (2011). Defining and cataloging exoplanets: the exoplanet.eu database. A&A, 532:A79.

Seager, S., Kuchner, M., Hier-Majumder, C. A., and Militzer, B. (2007). Mass-Radius Relationships for Solid Exoplanets. ApJ, 669(2):1279–1297.

Setiawan, J., Rodmann, J., da Silva, L., Hatzes, A. P., Pasquini, L., von der Lühe, O., de Medeiros, J. R., Döllinger, M. P., and Girardi, L. (2005). A substellar companion around the intermediate-mass giant star HD 11977. A&A, 437(2):L31–L34.

Sneden, C. A. (1973). *Carbon and nitrogen abundances in metal-poor stars.* PhD dissertation, The University of Texas at Austin.

Sotin, C., Grasset, O., and Mocquet, A. (2007). Mass radius curve for extrasolar Earth-like planets and ocean planets. Icarus, 191(1):337–351.

Sousa, S. G. (2014). *ARES + MOOG: A Practical Overview of an Equivalent Width (EW) Method to Derive Stellar Parameters*, pages 297–310.

Sousa, S. G., Adibekyan, V., Delgado-Mena, E., Santos, N. C., Andreasen, D. T., Ferreira, A. C. S., Tsantaki, M., Barros, S. C. C., Demangeon, O., Israelian, G., Faria, J. P., Figueira, P., Mortier, A., Brandão, I., Montalto, M., Rojas-Ayala, B., and Santerne, A. (2018). SWEET-Cat updated. New homogenous spectroscopic parameters. A&A, 620:A58.

Sousa, S. G., Adibekyan, V., Delgado-Mena, E., Santos, N. C., Rojas-Ayala, B., Soares, B. M. T. B., Legoinha, H., Ulmer-Moll, S., Camacho, J. D., Barros, S. C. C., Demangeon, O. D. S., Hoyer, S., Israelian, G., Mortier, A., Tsantaki, M., and Monteiro, M. (2021). SWEET-Cat 2.0: The Cat just got SWEETer; Higher quality spectra and precise parallaxes from GAIA eDR3. *arXiv e-prints*, page arXiv:2109.04781.

Sousa, S. G. and Andreasen, D. T. (2018). Tutorial: Measuring Stellar Atmospheric Parameters with ARES+MOOG. In Campante, T. L., Santos, N. C., and Monteiro, M. J. P. F. G., editors, *Asteroseismology and Exoplanets: Listening to the Stars and Searching for New Worlds*, volume 49, page 275.

Sousa, S. G., Santos, N. C., Adibekyan, V., Delgado-Mena, E., and Israelian, G. (2015). ARES v2: new features and improved performance. A&A, 577:A67.

Sousa, S. G., Santos, N. C., Israelian, G., Mayor, M., and Monteiro, M. J. P. F. G. (2007a). A new code for automatic determination of equivalent widths: Automatic Routine for line Equivalent widths in stellar Spectra (ARES). A&A, 469(2):783–791.

Sousa, S. G., Santos, N. C., Israelian, G., Mayor, M., and Monteiro, M. J. P. F. G. (2007b). VizieR Online Data Catalog: Code for automatic determination of EW (ARES) (Sousa+, 2007). *VizieR Online Data Catalog*, pages J/A+A/469/783.

Sousa, S. G., Santos, N. C., Israelian, G., Mayor, M., and Udry, S. (2011). Spectroscopic stellar parameters for 582 FGK stars in the HARPS volume-limited sample. Revising the metallicity-planet correlation. A&A, 533:A141.

Sousa, S. G., Santos, N. C., Mayor, M., Udry, S., Casagrande, L., Israelian, G., Pepe, F., Queloz, D., and Monteiro, M. J. P. F. G. (2008). Spectroscopic parameters for 451 stars in the HARPS GTO planet search program. Stellar [Fe/H] and the frequency of exo-Neptunes. A&A, 487(1):373–381.

Spiegel, D. S., Burrows, A., and Milsom, J. A. (2011). The Deuterium-burning Mass Limit for Brown Dwarfs and Giant Planets. ApJ, 727(1):57.

Spina, L., Sharma, P., Meléndez, J., Bedell, M., Casey, A. R., Carlos, M., Franciosini, E., and Vallenari, A. (2021). Chemical evidence for planetary ingestion in a quarter of Sun-like stars. *Nature Astronomy*.

Suárez-Andrés, L., Israelian, G., González Hernández, J. I., Adibekyan, V. Z., Delgado Mena, E., Santos, N. C., and Sousa, S. G. (2017). CNO behaviour in planet-harbouring stars. II. Carbon abundances in stars with and without planets using the CH band. A&A, 599:A96.

Thiabaud, A., Marboeuf, U., Alibert, Y., Cabral, N., Leya, I., and Mezger, K. (2014). From stellar nebula to planets: The refractory components. A&A, 562:A27.

Thiabaud, A., Marboeuf, U., Alibert, Y., Leya, I., and Mezger, K. (2015). Elemental ratios in stars vs planets. A&A, 580:A30.

Torres, G., Andersen, J., and Giménez, A. (2010). Accurate masses and radii of normal stars: modern results and applications. A&A Rev., 18(1-2):67–126.

Udry, S., Mayor, M., and Santos, N. C. (2003). Statistical properties of exoplanets. I. The period distribution: Constraints for the migration scenario. A&A, 407:369–376.

Udry, S. and Santos, N. C. (2007). Statistical Properties of Exoplanets. ARA&A, 45(1):397–439.

Unterborn, C. T. and Panero, W. R. (2017). The Effects of Mg/Si on the Exoplanetary Refractory Oxygen Budget. ApJ, 845(1):61.

Vorobyov, E. I. and Elbakyan, V. G. (2018). Gravitational fragmentation and formation of giant protoplanets on orbits of tens of au. A&A, 618:A7.

Wallerstein, G. (1962). Abundances in G. Dwarfs.VI. a Survey of Field Stars. ApJS, 6:407.

Wetherill, G. W. and Stewart, G. R. (1989). Accumulation of a swarm of small planetesimals. Icarus, 77(2):330–357.

Wittenmyer, R. A., O'Toole, S. J., Jones, H. R. A., Tinney, C. G., Butler, R. P., Carter, B. D., and Bailey, J. (2010). The Frequency of Low-mass Exoplanets. II. The "Period Valley". ApJ, 722(2):1854–1863.

Wright, J. T. (2018). *Radial Velocities as an Exoplanet Discovery Method*, page 4.

Wright, J. T. and Gaudi, B. S. (2013). *Exoplanet Detection Methods*, page 489.

Yi, S., Demarque, P., Kim, Y.-C., Lee, Y.-W., Ree, C. H., Lejeune, T., and Barnes, S. (2001). Toward Better Age Estimates for Stellar Populations: The Y^2 Isochrones for Solar Mixture. ApJS, 136(2):417–437.

Appendix A

Final Sample

A. FINAL SAMPLE

star	**Teff (K)**	$\log g_{cor}$ **(dex)**	V_{tur} **(km/s)**	**[Fe/H] (dex)**	$m \sin(i)$ (M_{jup})	$M_\star(M\odot)$	**SNR**
16CygB	5783.0±19	4.27±0.03	0.96±0.03	0.09±0.01	$1.64^{+0.08}_{-0.08}$	1.022±0.007	949
18Del	5076.0±38	3.205±0.1	1.32±0.04	0.0±0.03	$10.3^{+0.36}_{-0.36}$	1.947±0.013	932
24Sex	5069.0±62	3.528±0.13	1.27±0.07	-0.01±0.05	$1.84^{+0.11}_{-0.11}$	1.546±0.008	364
24Sex	5069.0±62	3.528±0.13	1.27±0.07	-0.01±0.05	$1.52^{+0.2}_{-0.2}$	1.546±0.008	364
55Cnc	5353.0±62	4.318±0.14	1.01±0.1	0.3±0.04	$3.86^{+0.6}_{-0.15}$	0.923±0.014	512
7CMa	4761.0±79	3.358±0.22	1.19±0.08	0.21±0.05	$1.895^{+0.06}_{-0.04}$	1.542±0.012	370
75Cet	4904.0±47	3.062±0.14	1.41±0.05	0.02±0.04	3.0	2.121±0.016	221
81Cet	4845.0±51	2.665±0.19	1.58±0.05	-0.07±0.04	5.3	2.239±0.017	726
epsTau	4946.0±70	2.796±0.15	1.48±0.07	0.17±0.06	$7.34^{+0.5}_{-0.4}$	2.449±0.022	408
GJ3021	5557.0±36	4.408±0.07	1.05±0.06	0.13±0.03	$3.37^{+0.09}_{-0.09}$	0.92±0.008	415
HAT-P-17	5332.0±55	4.476±0.13	0.82±0.1	0.05±0.03	1.4	0.829±0.006	288
HD100655	4891.0±46	2.987±0.11	1.37±0.04	0.07±0.03	$1.7^{+0.1}_{-0.2}$	2.155±0.015	666
HD100777	5536.0±26	4.276±0.05	0.81±0.04	0.25±0.02	$1.16^{+0.03}_{-0.03}$	0.995±0.008	387
HD102272	4807.0±34	2.8±0.13	1.53±0.04	-0.38±0.03	$5.9^{+0.2}_{-0.2}$	1.911±0.013	457
HD102272	4807.0±34	2.8±0.13	1.53±0.04	-0.38±0.03	$2.6^{+0.4}_{-0.4}$	1.911±0.013	457
HD106252	5871.0±15	4.196±0.03	1.1±0.02	-0.07±0.01	7.56	1.003±0.004	2166
HD106515A	5380.0±31	4.377±0.05	0.81±0.05	0.03±0.02	$9.61^{+0.14}_{-0.14}$	0.881±0.009	698
HD108874	5590.0±60	4.265±0.09	0.91±0.09	0.22±0.04	$1.36^{+0.13}_{-0.13}$	0.988±0.008	865
HD108874	5590.0±60	4.265±0.09	0.91±0.09	0.22±0.04	$1.018^{+0.3}_{-0.3}$	0.988±0.008	865
HD111232	5460.0±21	4.406±0.03	0.62±0.04	-0.43±0.02	6.8	0.8±0.004	1284
HD11506	6204.0±27	4.127±0.06	1.32±0.03	0.36±0.02	$4.83^{+0.52}_{-0.52}$	1.259±0.01	1392
HD117207	5667.0±21	4.216±0.04	1.01±0.02	0.22±0.02	2.06	1.031±0.007	1260
HD11977	5067.0±42	3.039±0.15	1.59±0.05	-0.16±0.04	$6.29^{+0.7}_{-0.7}$	2.186±0.013	941
HD121504	6022.0±11	4.247±0.03	1.12±0.01	0.14±0.01	1.22	1.098±0.005	1439
HD125612	5913.0±17	4.23±0.03	1.02±0.02	0.24±0.01	3.0	1.105±0.005	581
HD125612	5913.0±17	4.23±0.03	1.02±0.02	0.24±0.01	7.2	1.105±0.005	581
HD130322	5365.0±29	4.383±0.05	0.9±0.04	-0.02±0.02	1.02	0.86±0.007	684

star	**Teff (K)**	$\log g_{cor}$ **(dex)**	V_{tur} **(km/s)**	**[Fe/H] (dex)**	$m \sin(i)$ (M_{jup})	$M_\star(M\odot)$	**SNR**
HD132406	5766.0±23	4.047±0.03	1.05±0.03	0.14±0.02	5.61	1.086±0.005	1129
HD134987	5740.0±23	4.167±0.04	1.08±0.02	0.25±0.02	$1.59^{+0.02}_{-0.02}$	1.107±0.008	1315
HD13931	5940.0±31	4.209±0.07	1.19±0.04	0.08±0.02	$1.88^{+0.15}_{-0.15}$	1.074±0.005	2070
HD141937	5893.0±18	4.258±0.03	1.0±0.02	0.13±0.01	9.7	1.05±0.004	540
HD142022A	5508.0±32	4.307±0.05	0.83±0.04	0.19±0.03	$5.1^{+2.6}_{-1.5}$	0.958±0.007	351
HD142245	4843.0±66	3.426±0.14	1.18±0.07	0.13±0.04	$1.9^{+0.2}_{-0.2}$	1.477±0.009	354
HD143361	5503.0±36	4.319±0.06	0.9±0.06	0.22±0.03	$3.12^{+1.44}_{-1.44}$	0.964±0.007	530
HD145377	6054.0±16	4.275±0.03	1.11±0.02	0.12±0.01	$5.76^{+0.1}_{-0.1}$	1.112±0.006	669
HD147513	5858.0±18	4.321±0.03	1.03±0.02	0.03±0.01	1.21	1.002±0.004	1314
HD147873	6191.0±30	3.832±0.04	1.71±0.04	0.24±0.02	$5.14^{+0.34}_{-0.34}$	1.487±0.007	719
HD147873	6191.0±30	3.832±0.04	1.71±0.04	0.24±0.02	$2.3^{+0.18}_{-0.18}$	1.487±0.007	719
HD149143	5950.0±21	3.995±0.04	1.25±0.03	0.32±0.02	1.33	1.314±0.007	675
HD152079	5785.0±28	4.23±0.05	1.09±0.03	0.29±0.02	$3.0^{+2.0}_{-2.0}$	1.099±0.008	597
HD153950	6074.0±15	4.127±0.03	1.23±0.01	-0.01±0.01	$2.73^{+0.05}_{-0.05}$	1.133±0.005	575
HD154672	5743.0±23	4.136±0.04	1.08±0.03	0.25±0.02	$5.02^{+0.17}_{-0.17}$	1.121±0.007	609
HD154857	5560.0±12	3.837±0.02	1.13±0.02	-0.26±0.01	$2.24^{+0.05}_{-0.05}$	1.164±0.004	301
HD154857	5560.0±12	3.837±0.02	1.13±0.02	-0.26±0.01	$2.58^{+0.16}_{-0.16}$	1.164±0.004	301
HD159868	5558.0±15	3.898±0.02	1.02±0.01	-0.08±0.01	$2.218^{+0.059}_{-0.059}$	1.159±0.005	650
HD165155	5387.0±31	4.394±0.05	0.81±0.05	0.12±0.02	$2.89^{+0.23}_{-0.23}$	0.888±0.007	371
HD168443	5590.0±17	4.035±0.03	1.05±0.02	0.06±0.01	$7.659^{+0.098}_{-0.098}$	1.09±0.005	677
HD169830	6361.0±25	3.836±0.03	1.56±0.02	0.18±0.02	2.88	1.419±0.007	1633
HD169830	6361.0±25	3.836±0.03	1.56±0.02	0.18±0.02	4.04	1.419±0.007	1633
HD171028	5671.0±16	3.734±0.03	1.24±0.02	-0.48±0.01	1.98	1.166±0.004	1202
HD17156	6084.0±29	4.063±0.05	1.47±0.05	0.23±0.04	$3.191^{+0.033}_{-0.033}$	1.254±0.009	1118
HD183263	5986.0±21	4.161±0.04	1.11±0.03	0.32±0.02	$3.67^{+0.3}_{-0.3}$	1.181±0.008	604
HD183263	5986.0±21	4.161±0.04	1.11±0.03	0.32±0.02	$3.82^{+0.59}_{-0.59}$	1.181±0.008	604
HD188015	5726.0±28	4.223±0.06	1.05±0.04	0.27±0.02	1.26	1.051±0.008	903

A. FINAL SAMPLE

star	**Teff (K)**	$\log g_{cor}$ **(dex)**	V_{tur} **(km/s)**	**[Fe/H] (dex)**	$m\sin(i)$ (M_{jup})	$M_\star(M\odot)$	**SNR**
HD190647	5639.0±24	4.086±0.04	0.99±0.02	0.23±0.02	$1.9^{+0.06}_{-0.06}$	1.12±0.008	812
HD190984	6007.0±25	3.783±0.03	1.58±0.03	-0.49±0.02	3.1	1.237±0.006	834
HD195019	5800.0±14	4.054±0.03	1.08±0.02	0.07±0.01	$3.7^{+0.3}_{-0.3}$	1.106±0.005	1035
HD196050	5917.0±23	4.118±0.02	1.21±0.02	0.23±0.02	2.83	1.193±0.008	1192
HD196067	5999.0±34	3.896±0.04	1.3±0.03	0.23±0.02	$6.9^{+3.9}_{-1.1}$	1.317±0.004	687
HD19994A	6289.0±46	4.134±0.05	1.72±0.05	0.24±0.03	$1.37^{+0.12}_{-0.12}$	1.393±0.007	2060
HD204313	5776.0±22	4.233±0.02	1.0±0.02	0.18±0.02	$4.28^{+0.3}_{-0.3}$	1.045±0.007	1319
HD204313	5776.0±22	4.233±0.02	1.0±0.02	0.18±0.02	$1.68^{+0.3}_{-0.3}$	1.045±0.007	1319
HD205739	6301.0±25	4.049±0.04	1.42±0.03	0.21±0.02	$1.37^{+0.07}_{-0.09}$	1.288±0.012	856
HD20782	5774.0±14	4.224±0.01	1.0±0.01	-0.06±0.01	$1.9^{+0.5}_{-0.5}$	0.982±0.004	1754
HD210277	5505.0±27	4.259±0.04	0.86±0.04	0.18±0.02	$1.23^{+0.03}_{-0.03}$	0.969±0.007	1029
HD213240	5982.0±17	4.043±0.03	1.25±0.02	0.14±0.01	4.5	1.222±0.005	353
HD216435	6008.0±36	3.963±0.05	1.34±0.03	0.24±0.03	$1.26^{+0.13}_{-0.13}$	1.333±0.004	1538
HD216437	5860.0±19	4.03±0.03	1.24±0.02	0.24±0.02	1.82	1.188±0.008	1392
HD217786A	5966.0±19	4.129±0.04	1.12±0.02	-0.14±0.01	$13.0^{+0.8}_{-0.8}$	1.072±0.004	344
HD220689	5904.0±26	4.183±0.05	1.13±0.03	-0.01±0.02	$1.06^{+0.09}_{-0.09}$	1.043±0.004	905
HD220773	5995.0±34	4.028±0.07	1.33±0.04	0.11±0.03	$1.45^{+0.3}_{-0.3}$	1.232±0.009	2283
HD221287	6374.0±29	4.241±0.03	1.29±0.03	0.04±0.02	$3.09^{+0.79}_{-0.79}$	1.205±0.009	434
HD222582	5779.0±16	4.222±0.03	1.0±0.02	-0.01±0.01	$7.75^{+0.65}_{-0.65}$	1.004±0.003	1028
HD224538	6235.0±24	4.045±0.04	1.34±0.03	0.37±0.02	$5.97^{+0.42}_{-0.42}$	1.362±0.007	776
HD23079	5980.0±12	4.254±0.02	1.12±0.01	-0.12±0.01	$2.45^{+0.21}_{-0.21}$	1.014±0.004	1183
HD23127	5891.0±33	4.038±0.05	1.26±0.04	0.41±0.03	$1.5^{+0.2}_{-0.2}$	1.269±0.01	550
HD231701	6224.0±27	4.049±0.03	1.35±0.03	0.04±0.02	1.08	1.19±0.005	584
HD23596	6099.0±33	4.027±0.06	1.29±0.04	0.31±0.03	8.1	1.307±0.009	1296
HD27442	4781.0±76	3.7±0.19	1.09±0.11	0.33±0.05	$1.35^{+0.11}_{-0.11}$	1.353±0.013	366
HD27631	5700.0±20	4.253±0.05	1.0±0.03	-0.11±0.02	$1.45^{+0.14}_{-0.14}$	0.928±0.003	660
HD28185	5667.0±23	4.316±0.04	0.94±0.03	0.21±0.02	5.7	1.0±0.007	684

star	**Teff (K)**	**$\log g_{cor}$ (dex)**	**V_{tur} (km/s)**	**[Fe/H] (dex)**	**$m \sin(i)$ (M_{jup})**	**$M_\star (M\odot)$**	**SNR**
HD28254	5653.0±33	4.051±0.05	1.08±0.04	0.36±0.02	$1.16^{+0.1}_{-0.06}$	1.181±0.009	529
HD290327	5505.0±20	4.369±0.03	0.73±0.03	-0.14±0.01	$2.54^{+0.17}_{-0.14}$	0.871±0.003	370
HD30177	5601.0±42	4.261±0.05	0.89±0.05	0.37±0.03	$8.07^{+0.12}_{-0.12}$	1.064±0.011	622
HD30177	5601.0±42	4.261±0.05	0.89±0.05	0.37±0.03	$3.0^{+0.3}_{-0.3}$	1.064±0.011	622
HD30562	5963.0±24	4.02±0.05	1.28±0.03	0.28±0.02	$1.29^{+0.08}_{-0.08}$	1.276±0.006	386
HD33142	5049.0±41	3.476±0.14	1.17±0.04	0.03±0.03	$1.385^{+0.064}_{-0.064}$	1.422±0.009	741
HD38801	5314.0±43	3.853±0.08	1.29±0.06	0.25±0.03	$10.13^{+0.23}_{-0.23}$	1.237±0.011	522
HD4313	4966.0±40	3.528±0.17	1.17±0.05	0.05±0.03	$2.3^{+0.2}_{-0.2}$	1.543±0.01	551
HD47366	4919.0±37	3.267±0.08	1.26±0.04	0.0±0.03	$1.75^{+0.2}_{-0.2}$	1.798±0.009	318
HD47366	4919.0±37	3.267±0.08	1.26±0.04	0.0±0.03	$1.86^{+0.16}_{-0.16}$	1.798±0.009	318
HD48265	5798.0±29	3.795±0.14	1.36±0.03	0.36±0.02	$1.16^{+0.38}_{-0.38}$	1.375±0.009	911
HD50499	6077.0±19	4.096±0.04	1.27±0.02	0.34±0.01	$1.45^{+0.08}_{-0.08}$	1.265±0.009	1000
HD50499	6077.0±19	4.096±0.04	1.27±0.02	0.34±0.01	$2.93^{+0.73}_{-0.18}$	1.265±0.009	1000
HD50554	6026.0±30	4.166±0.13	1.11±0.06	0.01±0.04	5.16	1.077±0.005	2099
HD52265	6136.0±31	4.073±0.03	1.32±0.03	0.21±0.02	$1.21^{+0.05}_{-0.05}$	1.238±0.009	1361
HD5319	4869.0±51	3.426±0.1	1.11±0.05	0.02±0.03	1.94	1.416±0.009	201
HD5319	4869.0±51	3.426±0.1	1.11±0.05	0.02±0.03	$1.15^{+0.08}_{-0.08}$	1.416±0.009	201
HD5583	4986.0±35	3.03±0.09	1.62±0.04	-0.35±0.03	$5.78^{+0.53}_{-0.53}$	1.896±0.01	380
HD5891	4825.0±47	2.843±0.1	1.69±0.05	-0.38±0.04	$7.6^{+0.4}_{-0.4}$	1.952±0.013	554
HD60532	6273.0±37	3.68±0.04	1.88±0.05	-0.09±0.02	$1.03^{+0.05}_{-0.05}$	1.513±0.007	1931
HD60532	6273.0±37	3.68±0.04	1.88±0.05	-0.09±0.02	$2.46^{+0.09}_{-0.09}$	1.513±0.007	1931
HD65216	5612.0±16	4.357±0.02	0.78±0.03	-0.17±0.01	$1.295^{+0.062}_{-0.062}$	0.878±0.003	688
HD65216	5612.0±16	4.357±0.02	0.78±0.03	-0.17±0.01	$2.03^{+0.11}_{-0.11}$	0.878±0.003	688
HD66428	5705.0±27	4.191±0.06	0.96±0.03	0.25±0.02	$2.82^{+0.027}_{-0.027}$	1.058±0.008	587
HD6718	5723.0±15	4.314±0.02	0.84±0.02	-0.07±0.01	$1.56^{+0.11}_{-0.1}$	0.941±0.003	480
HD70642	5668.0±22	4.295±0.04	0.82±0.03	0.18±0.01	2.0	0.995±0.007	996
HD72659	5926.0±12	4.035±0.01	1.13±0.01	-0.02±0.01	$3.15^{+0.14}_{-0.14}$	1.13±0.005	610

A. FINAL SAMPLE

star	**Teff (K)**	$\log g_{cor}$ **(dex)**	V_{tur} **(km/s)**	**[Fe/H] (dex)**	$m \sin(i)$ (M_{jup})	$M_\star(M\odot)$	**SNR**
HD72892	5685.0±29	4.219±0.04	0.95±0.04	0.15±0.02	$5.45^{+0.37}_{-0.37}$	1.028±0.007	276
HD73267	5373.0±30	4.38±0.05	0.66±0.06	0.05±0.02	$3.06^{+0.07}_{-0.07}$	0.87±0.008	575
HD73526	5661.0±25	4.048±0.04	1.1±0.03	0.26±0.02	$2.25^{+0.12}_{-0.12}$	1.136±0.005	236
HD73526	5661.0±25	4.048±0.04	1.1±0.03	0.26±0.02	$2.25^{+0.13}_{-0.13}$	1.136±0.005	236
HD73534	4884.0±63	3.79±0.2	1.0±0.08	0.16±0.04	1.15	1.15±0.013	486
HD75898	6137.0±29	4.023±0.05	1.36±0.03	0.3±0.02	2.51	1.322±0.007	1001
HD82943	5989.0±20	4.2±0.02	1.1±0.02	0.26±0.01	4.8	1.154±0.008	1753
HD82943	5989.0±20	4.2±0.02	1.1±0.02	0.26±0.01	4.78	1.154±0.008	1753
HD86081	6036.0±23	3.962±0.04	1.34±0.03	0.22±0.02	1.5	1.286±0.008	383
HD89307	5992.0±17	4.259±0.03	1.06±0.03	-0.09±0.01	$2.0^{+0.4}_{-0.4}$	1.009±0.004	1115
HD9174	5631.0±30	3.96±0.04	1.12±0.03	0.36±0.02	$1.11^{+0.14}_{-0.14}$	1.218±0.012	467
HD92788	5744.0±24	4.256±0.04	0.95±0.03	0.27±0.02	$3.76^{+0.16}_{-0.16}$	1.07±0.008	852
HD92788	5744.0±24	4.256±0.04	0.95±0.03	0.27±0.02	$3.76^{+0.16}_{-0.16}$	1.07±0.008	852
HD98649	5714.0±22	4.247±0.05	1.01±0.03	-0.03±0.02	$6.79^{+0.5}_{-0.3}$	0.94±0.003	271
HIP63242	4812.0±37	2.738±0.09	1.68±0.04	-0.31±0.03	9.18	1.974±0.013	490
HR810	6227.0±26	4.208±0.06	1.29±0.03	0.19±0.02	$2.26^{+0.18}_{-0.18}$	1.197±0.009	1947
kappaCrB	4889.0±48	3.398±0.11	1.13±0.04	0.11±0.03	1.6	1.507±0.012	443
KELT-6	6246.0±88	3.89±0.09	1.66±0.13	-0.22±0.06	$3.71^{+0.21}_{-0.21}$	1.221±0.008	579
muAra	5784.0±21	4.07±0.04	1.07±0.03	0.3±0.02	1.676	1.155±0.008	1381
muAra	5784.0±21	4.07±0.04	1.07±0.03	0.3±0.02	1.814	1.155±0.008	1381
piMen	6003.0±17	4.185±0.03	1.12±0.02	0.09±0.01	$10.02^{+0.15}_{-0.15}$	1.101±0.005	1537
TYC+1422-614-1	4908.0±41	3.091±0.12	1.57±0.05	-0.07±0.03	$2.51^{+0.12}_{-0.12}$	2.025±0.021	265
TYC+1422-614-1	4908.0±41	3.091±0.12	1.57±0.05	-0.07±0.03	$10.1^{+0.14}_{-0.14}$	2.025±0.021	265
upsAnd	6212.0±64	3.944±0.13	1.69±0.16	0.13±0.08	$1.8^{+0.26}_{-0.26}$	1.343±0.007	987
upsAnd	6212.0±64	3.944±0.13	1.69±0.16	0.13±0.08	10.19	1.343±0.007	987
upsAnd	6212.0±64	3.944±0.13	1.69±0.16	0.13±0.08	$1.059^{+0.028}_{-0.028}$	1.343±0.007	987
WASP-41	5546.0±33	4.473±0.07	1.08±0.05	0.06±0.02	$3.18^{+0.2}_{-0.2}$	0.889±0.004	248

star	**Teff (K)**	$\log g_{cor}$ **(dex)**	V_{tur} **(km/s)**	**[Fe/H] (dex)**	$m \sin(i)$ (M_{jup})	$M_{\star}(M\odot)$	**SNR**

Table A.1: Table with the final sample with stellar parameters, the planetary mass and the SNR of the spectra

Appendix B

Final abundances

B. FINAL ABUNDANCES

star	**[Mg/H] (dex)**	**[Si/H] (dex)**	**[Fe/H] (dex)**	**[C/H] (dex)**	**[O/H] (dex)**	**[Ti/H] (dex)**	**[Ni/H] (dex)**
16CygB	0.138±0.014	0.083±0.018	0.09±0.01	0.05±0.088	0.11±0.061	0.117±0.026	0.092±0.024
18Del	0.095±0.069	0.073±0.058	0.0±0.03	0.03±0.062	0.07±0.081	0.06±0.059	0.01±0.045
24Sex	0.027±0.069	0.089±0.052	-0.01±0.05	0.01±0.052	0.06±0.064	0.059±0.078	-0.018±0.049
55Cnc	0.388±0.062	0.376±0.063	0.3±0.04	0.29±0.041	0.35±0.091	0.432±0.08	0.375±0.066
7CMa	0.337±0.067	0.423±0.113	0.21±0.05	0.28±0.082	0.37±0.092	0.188±0.119	0.32±0.092
75Cet	0.146±0.062	0.204±0.069	0.02±0.04	0.12±0.044	0.16±0.051	0.056±0.067	0.05±0.055
81Cet	0.08±0.082	0.124±0.068	-0.07±0.04	0.06±0.066	0.1±0.071	-0.06±0.084	-0.072±0.068
epsTau	0.196±0.1	0.359±0.076	0.17±0.06	0.19±0.103	0.23±0.105	0.212±0.1	0.222±0.088
GJ3021	0.075±0.053	0.098±0.031	0.13±0.03	0.01±0.054	0.07±0.062	0.178±0.053	0.094±0.03
HAT-P-17	0.064±0.044	0.041±0.03	0.05±0.03	-0.01±0.054	0.02±0.071	0.177±0.072	0.034±0.036
HD100655	0.107±0.094	0.227±0.064	0.07±0.03	0.11±0.065	0.15±0.055	0.081±0.079	0.084±0.056
HD100777	0.299±0.035	0.298±0.025	0.25±0.02	0.24±0.039	0.26±0.041	0.3±0.049	0.341±0.032
HD102272	0.001±0.045	-0.005±0.049	-0.38±0.03	-0.04±0.043	0.04±0.033	-0.119±0.058	-0.265±0.045
HD106252	-0.074±0.015	-0.081±0.026	-0.07±0.01	-0.13±0.029	-0.07±0.041	-0.098±0.018	-0.11±0.016
HD106515A	0.13±0.032	0.107±0.057	0.03±0.02	0.07±0.061	0.11±0.07	0.196±0.042	0.066±0.031
HD108874	0.221±0.063	0.19±0.027	0.22±0.04	0.14±0.074	0.2±0.062	0.25±0.077	0.227±0.039
HD111232	-0.151±0.046	-0.242±0.027	-0.43±0.02	-0.22±0.057	-0.02±0.071	-0.158±0.036	-0.4±0.021
HD11506	0.327±0.028	0.385±0.035	0.36±0.02	0.31±0.031	0.37±0.061	0.357±0.042	0.386±0.026
HD117207	0.215±0.032	0.202±0.035	0.22±0.02	0.14±0.052	0.2±0.07	0.223±0.037	0.236±0.026
HD11977	-0.03±0.052	-0.046±0.045	-0.16±0.04	-0.07±0.053	-0.01±0.051	-0.109±0.065	-0.191±0.045
HD121504	0.118±0.01	0.125±0.022	0.14±0.01	0.05±0.05	0.11±0.052	0.117±0.019	0.112±0.013
HD125612	0.247±0.025	0.232±0.033	0.24±0.01	0.18±0.045	0.24±0.051	0.259±0.026	0.253±0.022
HD130322	0.015±0.025	-0.009±0.036	-0.02±0.02	-0.05±0.044	0.0±0.041	0.025±0.037	-0.017±0.023
HD132406	0.146±0.022	0.106±0.017	0.14±0.02	0.04±0.051	0.1±0.051	0.133±0.032	0.075±0.021
HD134987	0.293±0.033	0.286±0.036	0.25±0.02	0.23±0.044	0.26±0.041	0.278±0.037	0.32±0.028
HD13931	0.107±0.019	0.058±0.022	0.08±0.02	0.02±0.076	0.05±0.073	0.096±0.032	0.068±0.025
HD141937	0.12±0.028	0.108±0.027	0.13±0.01	0.04±0.055	0.09±0.061	0.106±0.023	0.116±0.019

Table B.1 continued from previous page

star	**[Mg/H] (dex)**	**[Si/H] (dex)**	**[Fe/H] (dex)**	**[C/H] (dex)**	**[O/H] (dex)**	**[Ti/H] (dex)**	**[Ni/H] (dex)**
HD142022A	0.292±0.047	0.185±0.025	0.19±0.03	0.2±0.048	0.26±0.045	0.277±0.053	0.213±0.026
HD142245	0.243±0.055	0.278±0.075	0.13±0.04	0.19±0.081	0.24±0.072	0.16±0.104	0.203±0.069
HD143361	0.257±0.037	0.249±0.03	0.22±0.03	0.19±0.047	0.25±0.051	0.296±0.051	0.27±0.032
HD145377	0.082±0.019	0.102±0.03	0.12±0.01	0.02±0.045	0.07±0.062	0.132±0.024	0.078±0.018
HD147513	-0.002±0.045	-0.026±0.026	0.03±0.01	-0.08±0.047	-0.04±0.041	0.042±0.027	-0.047±0.016
HD147873	0.208±0.055	0.276±0.037	0.24±0.02	0.16±0.052	0.21±0.062	0.215±0.035	0.211±0.032
HD149143	0.351±0.055	0.342±0.033	0.32±0.02	0.27±0.039	0.3±0.071	0.313±0.027	0.354±0.024
HD152079	0.318±0.034	0.321±0.03	0.29±0.02	0.25±0.033	0.26±0.051	0.309±0.039	0.346±0.029
HD153950	0.044±0.044	0.01±0.023	-0.01±0.01	-0.03±0.044	-0.0±0.052	0.022±0.021	-0.018±0.017
HD154672	0.33±0.034	0.259±0.023	0.25±0.02	0.24±0.033	0.25±0.031	0.299±0.033	0.288±0.029
HD154857	-0.168±0.027	-0.207±0.014	-0.26±0.01	-0.25±0.037	-0.11±0.031	-0.224±0.027	-0.286±0.015
HD159868	-0.003±0.019	-0.023±0.022	-0.08±0.01	-0.05±0.038	0.0±0.031	-0.02±0.026	-0.065±0.017
HD165155	0.116±0.035	0.111±0.025	0.12±0.02	0.04±0.051	0.1±0.062	0.176±0.043	0.14±0.029
HD168443	0.225±0.028	0.115±0.022	0.06±0.01	0.14±0.061	0.19±0.044	0.166±0.028	0.072±0.022
HD169830	0.173±0.065	0.168±0.035	0.18±0.02	0.09±0.066	0.16±0.061	0.135±0.027	0.142±0.023
HD171028	-0.382±0.063	-0.413±0.026	-0.48±0.01	-0.42±0.073	-0.22±0.1	-0.457±0.03	-0.528±0.019
HD17156	0.199±0.046	0.209±0.026	0.23±0.04	0.13±0.057	0.19±0.061	0.196±0.033	0.23±0.022
HD183263	0.309±0.035	0.327±0.036	0.32±0.02	0.25±0.042	0.27±0.061	0.314±0.033	0.366±0.024
HD188015	0.311±0.028	0.275±0.041	0.27±0.02	0.24±0.05	0.25±0.042	0.282±0.037	0.321±0.026
HD190647	0.357±0.038	0.286±0.03	0.23±0.02	0.25±0.032	0.26±0.031	0.353±0.042	0.287±0.034
HD190984	-0.393±0.053	-0.397±0.019	-0.49±0.02	-0.43±0.057	-0.25±0.09	-0.41±0.033	-0.517±0.027
HD195019	0.1±0.018	0.04±0.024	0.07±0.01	0.0±0.057	0.02±0.072	0.052±0.022	0.02±0.017
HD196050	0.267±0.024	0.262±0.027	0.23±0.02	0.21±0.032	0.27±0.04	0.256±0.03	0.286±0.024
HD196067	0.29±0.03	0.286±0.032	0.23±0.02	0.23±0.041	0.27±0.041	0.261±0.032	0.29±0.026
HD19994A	0.186±0.049	0.271±0.031	0.24±0.03	0.14±0.045	0.19±0.053	0.261±0.045	0.256±0.034
HD204313	0.213±0.022	0.183±0.019	0.18±0.02	0.13±0.051	0.18±0.061	0.197±0.033	0.218±0.022

Table B.1 continued from previous page

star	[Mg/H] (dex)	[Si/H] (dex)	[Fe/H] (dex)	[C/H] (dex)	[O/H] (dex)	[Ti/H] (dex)	[Ni/H] (dex)
HD205739	0.15±0.057	0.175±0.028	0.21±0.02	0.08±0.055	0.14±0.052	0.165±0.031	0.178±0.022
HD20782	-0.033±0.013	-0.077±0.022	-0.06±0.01	-0.1±0.033	-0.03±0.042	-0.048±0.023	-0.109±0.02
HD210277	0.253±0.032	0.22±0.025	0.18±0.02	0.19±0.048	0.26±0.052	0.282±0.04	0.208±0.03
HD213240	0.17±0.065	0.153±0.03	0.14±0.01	0.09±0.061	0.15±0.062	0.141±0.021	0.161±0.019
HD216435	0.251±0.054	0.266±0.032	0.24±0.03	0.19±0.056	0.23±0.061	0.23±0.038	0.272±0.029
HD216437	0.305±0.024	0.244±0.024	0.24±0.02	0.23±0.041	0.25±0.032	0.23±0.028	0.258±0.024
HD217786A	-0.058±0.045	-0.1±0.014	-0.14±0.01	-0.11±0.049	-0.05±0.062	-0.131±0.027	-0.143±0.016
HD220689	0.006±0.031	-0.022±0.028	-0.01±0.02	-0.07±0.036	-0.01±0.032	-0.061±0.023	-0.043±0.02
HD220773	0.102±0.023	0.102±0.022	0.11±0.03	0.04±0.044	0.09±0.051	0.081±0.039	0.1±0.026
HD221287	0.001±0.042	0.011±0.022	0.04±0.02	-0.06±0.047	-0.02±0.042	0.033±0.037	-0.034±0.023
HD222582	0.056±0.014	0.021±0.027	-0.01±0.01	-0.02±0.045	0.0±0.061	0.016±0.018	-0.007±0.016
HD224538	0.349±0.038	0.416±0.036	0.37±0.02	0.32±0.059	0.41±0.061	0.339±0.031	0.404±0.022
HD23079	-0.081±0.076	-0.148±0.021	-0.12±0.01	-0.15±0.062	-0.08±0.05	-0.113±0.019	-0.174±0.015
HD23127	0.529±0.038	0.47±0.042	0.41±0.03	0.33±0.049	0.44±0.034	0.451±0.046	0.537±0.038
HD231701	0.037±0.055	0.031±0.022	0.04±0.02	-0.03±0.053	0.01±0.06	0.008±0.031	0.002±0.021
HD23596	0.302±0.025	0.33±0.029	0.31±0.03	0.25±0.037	0.28±0.061	0.258±0.035	0.342±0.029
HD27442	0.387±0.079	0.573±0.118	0.33±0.05	0.32±0.074	0.44±0.054	0.325±0.132	0.431±0.086
HD27631	0.008±0.02	-0.077±0.021	-0.11±0.02	-0.07±0.038	0.0±0.046	0.005±0.027	-0.154±0.018
HD28185	0.248±0.033	0.234±0.025	0.21±0.02	0.18±0.046	0.24±0.062	0.254±0.044	0.275±0.027
HD28254	0.455±0.053	0.396±0.034	0.36±0.02	0.31±0.031	0.4±0.072	0.391±0.048	0.433±0.04
HD290327	-0.07±0.025	-0.096±0.014	-0.14±0.01	-0.11±0.036	-0.07±0.051	-0.076±0.033	-0.125±0.022
HD30177	0.399±0.046	0.409±0.035	0.37±0.03	0.32±0.041	0.41±0.061	0.434±0.057	0.472±0.039
HD30562	0.268±0.03	0.265±0.033	0.28±0.02	0.2±0.046	0.23±0.041	0.26±0.03	0.288±0.026
HD33142	0.133±0.036	0.086±0.052	0.03±0.03	0.06±0.072	0.1±0.07	0.093±0.072	0.031±0.043
HD38801	0.296±0.043	0.245±0.038	0.25±0.03	0.21±0.053	0.25±0.041	0.308±0.07	0.249±0.054
HD4313	0.134±0.079	0.15±0.049	0.05±0.03	0.09±0.055	0.14±0.051	0.08±0.067	0.092±0.057

Table B.1 continued from previous page

star	**[Mg/H] (dex)**	**[Si/H] (dex)**	**[Fe/H] (dex)**	**[C/H] (dex)**	**[O/H] (dex)**	**[Ti/H] (dex)**	**[Ni/H] (dex)**
HD47366	0.079±0.06	0.131±0.04	0.0±0.03	0.07±0.045	0.11±0.042	0.049±0.061	0.014±0.054
HD48265	0.499±0.05	0.393±0.036	0.36±0.02	0.31±0.031	0.4±0.072	0.402±0.041	0.454±0.036
HD50499	0.32±0.017	0.362±0.036	0.34±0.01	0.29±0.037	0.35±0.071	0.314±0.028	0.389±0.024
HD50554	0.004±0.027	0.014±0.026	0.01±0.04	-0.05±0.042	-0.0±0.043	-0.029±0.031	-0.058±0.024
HD52265	0.202±0.041	0.231±0.028	0.21±0.02	0.14±0.056	0.19±0.061	0.168±0.033	0.211±0.026
HD5319	0.153±0.057	0.167±0.059	0.02±0.03	0.11±0.045	0.15±0.051	0.065±0.078	0.105±0.057
HD5583	-0.026±0.047	-0.046±0.03	-0.35±0.03	-0.07±0.043	0.03±0.033	-0.064±0.065	-0.291±0.037
HD5891	-0.055±0.047	-0.015±0.048	-0.38±0.04	-0.08±0.055	0.02±0.034	-0.16±0.075	-0.294±0.053
HD60532	-0.106±0.086	-0.061±0.033	-0.09±0.02	-0.14±0.064	-0.06±0.041	-0.087±0.039	-0.159±0.035
HD65216	-0.128±0.021	-0.172±0.013	-0.17±0.01	-0.21±0.045	-0.1±0.025	-0.128±0.022	-0.215±0.017
HD66428	0.295±0.043	0.319±0.042	0.25±0.02	0.24±0.045	0.28±0.06	0.3±0.04	0.332±0.029
HD6718	-0.049±0.026	-0.078±0.01	-0.07±0.01	-0.11±0.035	-0.05±0.041	-0.066±0.023	-0.085±0.016
HD70642	0.186±0.03	0.208±0.03	0.18±0.01	0.12±0.042	0.16±0.051	0.197±0.032	0.221±0.026
HD72659	0.039±0.023	0.01±0.021	-0.02±0.01	-0.03±0.046	0.0±0.042	-0.014±0.019	-0.023±0.015
HD72892	0.209±0.044	0.165±0.025	0.15±0.02	0.12±0.061	0.18±0.071	0.179±0.036	0.165±0.03
HD73267	0.162±0.02	0.103±0.038	0.05±0.02	0.09±0.059	0.13±0.061	0.208±0.052	0.074±0.03
HD73526	0.392±0.044	0.294±0.025	0.26±0.02	0.25±0.021	0.26±0.031	0.335±0.035	0.291±0.032
HD73534	0.217±0.068	0.299±0.059	0.16±0.04	0.18±0.092	0.23±0.084	0.19±0.097	0.245±0.061
HD75898	0.28±0.035	0.315±0.031	0.3±0.02	0.22±0.044	0.25±0.061	0.291±0.037	0.343±0.025
HD82943	0.246±0.023	0.252±0.02	0.26±0.01	0.18±0.042	0.24±0.041	0.228±0.028	0.281±0.022
HD86081	0.263±0.089	0.248±0.033	0.22±0.02	0.19±0.062	0.23±0.06	0.204±0.028	0.258±0.031
HD89307	-0.065±0.026	-0.11±0.016	-0.09±0.01	-0.13±0.039	-0.08±0.051	-0.093±0.023	-0.151±0.015
HD9174	0.408±0.048	0.398±0.034	0.36±0.02	0.32±0.035	0.4±0.061	0.373±0.042	0.433±0.045
HD92788	0.29±0.028	0.306±0.034	0.27±0.02	0.23±0.038	0.26±0.051	0.315±0.037	0.332±0.029
HD98649	-0.007±0.036	-0.041±0.025	-0.03±0.02	-0.08±0.034	-0.02±0.032	-0.032±0.027	-0.068±0.018
HIP63242	-0.018±0.039	0.066±0.046	-0.31±0.03	-0.01±0.044	0.05±0.035	-0.148±0.063	-0.238±0.041

Table B.1 continued from previous page

star	**[Mg/H] (dex)**	**[Si/H] (dex)**	**[Fe/H] (dex)**	**[C/H] (dex)**	**[O/H] (dex)**	**[Ti/H] (dex)**	**[Ni/H] (dex)**
HR810	0.178±0.183	0.156±0.033	0.19±0.02	0.09±0.092	0.16±0.083	0.166±0.032	0.163±0.019
kappaCrB	0.212±0.05	0.223±0.067	0.11±0.03	0.15±0.052	0.2±0.07	0.184±0.087	0.168±0.061
KELT-6	-0.23±0.156	-0.199±0.035	-0.22±0.06	-0.25±0.091	-0.13±0.08	-0.238±0.072	-0.342±0.053
muAra	0.321±0.037	0.295±0.028	0.3±0.02	0.25±0.045	0.24±0.043	0.324±0.035	0.331±0.031
piMen	0.108±0.017	0.074±0.017	0.09±0.01	0.03±0.052	0.07±0.062	0.057±0.019	0.086±0.017
TYC+1422-614-1	0.025±0.093	0.082±0.054	-0.07±0.03	0.02±0.062	0.06±0.063	-0.018±0.087	-0.033±0.051
upsAnd	0.112±0.116	0.148±0.03	0.13±0.08	0.07±0.072	0.14±0.071	0.094±0.064	0.091±0.052
WASP-41	0.043±0.047	0.05±0.025	0.06±0.02	-0.01±0.056	0.02±0.061	0.096±0.043	0.027±0.024

Table B.1: Table with the final abundances of our sample, where Mg, Si, Ti and Ni were derived using ARES + MOOG, the C and O were derived using machine learning and Fe was obtained from the SWEET-Cat database.

Appendix C

Planetary building blocks

star	**Z** (%)	f_{iron} (%)	w_f (%)	$m \sin(i)$ (M_{jup})	$M_\star$ ($M\odot$)
16CygB	1.66±0.17	32.24±1.19	58.76±4.8	$1.64^{+0.08}_{-0.08}$	1.022±0.007
18Del	1.53±0.18	29.03±2.66	58.19±6.92	$10.3^{+0.36}_{-0.36}$	1.947±0.013
24Sex	1.47±0.14	29.74±3.3	58.88±5.46	$1.84^{+0.11}_{-0.11}$	1.546±0.008
24Sex	1.47±0.14	29.74±3.3	58.88±5.46	$1.52^{+0.2}_{-0.2}$	1.546±0.008
55Cnc	2.86±0.35	29.12±3.01	56.81±7.29	$3.86^{+0.6}_{-0.15}$	0.923±0.014
7CMa	2.87±0.39	24.83±3.78	58.52±8.44	$1.895^{+0.06}_{-0.04}$	1.542±0.012
75Cet	1.82±0.15	25.55±2.89	58.55±5.27	3.0	2.121±0.016
81Cet	1.59±0.18	25.02±2.97	60.07±6.16	5.3	2.239±0.017
epsTau	2.23±0.35	27.47±3.82	54.41±9.13	$7.34^{+0.5}_{-0.4}$	2.449±0.022
GJ3021	1.54±0.14	35.42±2.27	55.73±5.36	$3.37^{+0.09}_{-0.09}$	0.92±0.008
HAT-P-17	1.39±0.14	33.18±2.24	55.43±5.98	1.4	0.829±0.006
HD100655	1.81±0.16	28.07±3.12	57.32±5.53	$1.7^{+0.1}_{-0.2}$	2.155±0.015
HD100777	2.39±0.16	30.86±1.71	56.24±4.14	$1.16^{+0.03}_{-0.03}$	0.995±0.008
HD102272	1.28±0.09	17.42±1.54	65.72±3.49	$5.9^{+0.2}_{-0.2}$	1.911±0.013
HD102272	1.28±0.09	17.42±1.54	65.72±3.49	$2.6^{+0.4}_{-0.4}$	1.911±0.013
HD106252	1.08±0.07	33.69±1.34	58.16±3.68	7.56	1.003±0.004
HD106515A	1.65±0.18	28.99±2.02	58.93±5.98	$9.61^{+0.14}_{-0.14}$	0.881±0.009
HD108874	2.05±0.2	34.23±2.81	57.44±5.19	$1.36^{+0.13}_{-0.13}$	0.988±0.008
HD108874	2.05±0.2	34.23±2.81	57.44±5.19	$1.018^{+0.3}_{-0.3}$	0.988±0.008
HD111232	1.03±0.12	22.64±1.53	72.14±4.24	6.8	0.8±0.004
HD11506	2.95±0.26	33.18±1.78	58.48±5.06	$4.83^{+0.52}_{-0.52}$	1.259±0.01
HD117207	2.04±0.21	33.91±1.83	56.96±5.72	2.06	1.031±0.007
HD11977	1.21±0.1	27.3±2.61	61.6±4.48	$6.29^{+0.7}_{-0.7}$	2.186±0.013
HD121504	1.67±0.13	34.16±1.21	56.87±4.31	1.22	1.098±0.005
HD125612	2.21±0.18	33.22±1.45	57.87±4.53	3.0	1.105±0.005
HD125612	2.21±0.18	33.22±1.45	57.87±4.53	7.2	1.105±0.005
HD130322	1.28±0.09	32.11±1.72	58.13±3.88	1.02	0.86±0.007
HD132406	1.63±0.13	34.08±1.48	55.71±4.35	5.61	1.086±0.005
HD134987	2.36±0.16	31.18±1.71	56.42±4.09	$1.59^{+0.02}_{-0.02}$	1.107±0.008
HD13931	1.5±0.17	33.2±1.53	55.62±6.0	$1.88^{+0.15}_{-0.15}$	1.074±0.005

C. PLANETARY BUILDING BLOCKS

star	**Z** (%)	f_{iron} (%)	w_f (%)	$m\sin(i)$ (M_{jup})	$M_\star$ ($M\odot$)
HD141937	1.61±0.15	33.99±1.49	55.91±5.17	9.7	1.05±0.004
HD142022A	2.27±0.18	30.9±2.12	60.34±4.19	$5.1^{+2.6}_{-1.5}$	0.958±0.007
HD142245	2.19±0.25	26.86±2.87	57.91±6.5	$1.9^{+0.2}_{-0.2}$	1.477±0.009
HD143361	2.24±0.18	31.61±2.09	58.08±4.59	$3.12^{+1.44}_{-1.44}$	0.964±0.007
HD145377	1.54±0.13	34.61±1.46	55.64±4.95	$5.76^{+0.1}_{-0.1}$	1.112±0.006
HD147513	1.21±0.08	35.46±1.64	55.16±4.04	1.21	1.002±0.004
HD147873	2.11±0.19	32.82±2.1	54.97±5.5	$5.14^{+0.34}_{-0.34}$	1.487±0.007
HD147873	2.11±0.19	32.82±2.1	54.97±5.5	$2.3^{+0.18}_{-0.18}$	1.487±0.007
HD149143	2.62±0.25	32.03±2.07	54.76±6.03	1.33	1.314±0.007
HD152079	2.44±0.18	31.78±1.66	54.15±4.87	$3.0^{+2.0}_{-2.0}$	1.099±0.008
HD153950	1.31±0.1	31.42±1.61	56.57±4.71	$2.73^{+0.05}_{-0.05}$	1.133±0.005
HD154672	2.35±0.14	31.11±1.58	55.76±3.59	$5.02^{+0.17}_{-0.17}$	1.121±0.007
HD154857	0.9±0.06	29.73±1.17	64.35±3.0	$2.24^{+0.05}_{-0.05}$	1.164±0.004
HD154857	0.9±0.06	29.73±1.17	64.35±3.0	$2.58^{+0.16}_{-0.16}$	1.164±0.004
HD159868	1.26±0.08	29.91±1.17	60.06±3.23	$2.218^{+0.059}_{-0.059}$	1.159±0.005
HD165155	1.63±0.15	33.62±1.69	56.86±5.07	$2.89^{+0.23}_{-0.23}$	0.888±0.007
HD168443	1.93±0.15	27.88±1.2	61.23±3.93	$7.659^{+0.098}_{-0.098}$	1.09±0.005
HD169830	1.85±0.17	33.74±2.22	56.69±5.3	2.88	1.419±0.007
HD169830	1.85±0.17	33.74±2.22	56.69±5.3	4.04	1.419±0.007
HD171028	0.68±0.11	29.24±1.78	70.39±6.1	1.98	1.166±0.004
HD17156	2.0±0.18	34.4±2.63	56.03±5.14	$3.191^{+0.033}_{-0.033}$	1.254±0.009
HD183263	2.48±0.22	33.32±1.87	53.94±5.47	$3.67^{+0.3}_{-0.3}$	1.181±0.008
HD183263	2.48±0.22	33.32±1.87	53.94±5.47	$3.82^{+0.59}_{-0.59}$	1.181±0.008
HD188015	2.36±0.17	32.21±1.76	55.32±4.19	1.26	1.051±0.008
HD190647	2.4±0.14	28.81±1.67	55.28±3.72	$1.9^{+0.06}_{-0.06}$	1.12±0.008
HD190984	0.64±0.09	28.57±1.76	68.76±5.63	3.1	1.237±0.006
HD195019	1.41±0.14	33.35±1.26	54.32±6.01	$3.7^{+0.3}_{-0.3}$	1.106±0.005
HD196050	2.34±0.16	31.56±1.63	58.8±3.78	2.83	1.193±0.008
HD196067	2.38±0.17	30.34±1.71	57.73±3.96	$6.9^{+3.9}_{-1.1}$	1.317±0.004
HD19994A	2.03±0.17	33.5±2.22	54.28±5.17	$1.37^{+0.12}_{-0.12}$	1.393±0.007
HD204313	1.96±0.18	32.35±1.48	56.96±5.17	$4.28^{+0.3}_{-0.3}$	1.045±0.007
HD204313	1.96±0.18	32.35±1.48	56.96±5.17	$1.68^{+0.3}_{-0.3}$	1.045±0.007
HD205739	1.8±0.16	35.75±2.12	55.05±4.9	$1.37^{+0.07}_{-0.09}$	1.288±0.012
HD20782	1.18±0.08	33.05±1.16	59.88±3.71	$1.9^{+0.5}_{-0.5}$	0.982±0.004
HD210277	2.25±0.19	30.48±1.63	60.58±4.33	$1.23^{+0.03}_{-0.03}$	0.969±0.007
HD213240	1.81±0.17	32.09±1.9	57.17±5.22	4.5	1.222±0.005
HD216435	2.22±0.2	32.3±2.18	56.2±5.35	$1.26^{+0.13}_{-0.13}$	1.333±0.004
HD216437	2.32±0.14	31.57±1.55	56.96±3.45	1.82	1.188±0.008
HD217786A	1.12±0.11	30.2±1.44	60.88±5.02	$13.0^{+0.8}_{-0.8}$	1.072±0.004
HD220689	1.25±0.08	33.21±1.72	57.68±3.51	$1.06^{+0.09}_{-0.09}$	1.043±0.004
HD220773	1.59±0.12	33.65±1.99	56.73±4.43	$1.45^{+0.3}_{-0.3}$	1.232±0.009
HD221287	1.26±0.09	34.79±1.79	55.09±4.01	$3.09^{+0.79}_{-0.79}$	1.205±0.009
HD222582	1.32±0.11	30.89±1.22	55.92±4.92	$7.75^{+0.65}_{-0.65}$	1.004±0.003

star	**Z** (%)	$\boldsymbol{f_{iron}}$ (%)	$\boldsymbol{w_f}$ (%)	$\boldsymbol{m}\,\mathbf{sin}\,(\boldsymbol{i})$ (M_{jup})	$\boldsymbol{M_\star}$ $(M\odot)$
HD224538	3.15±0.3	32.29±1.93	59.49±5.01	$5.97^{+0.42}_{-0.42}$	1.362±0.007
HD23079	1.05±0.08	32.86±2.18	60.23±4.11	$2.45^{+0.21}_{-0.21}$	1.014±0.004
HD23127	3.39±0.22	28.89±2.07	55.19±3.9	$1.5^{+0.2}_{-0.2}$	1.269±0.01
HD231701	1.35±0.12	33.4±1.92	56.04±5.02	1.08	1.19±0.005
HD23596	2.51±0.22	32.83±2.0	55.47±5.24	8.1	1.307±0.009
HD27442	3.34±0.3	25.12±4.23	55.4±7.4	$1.35^{+0.11}_{-0.11}$	1.353±0.013
HD27631	1.23±0.09	29.52±1.41	61.57±3.89	$1.45^{+0.14}_{-0.14}$	0.928±0.003
HD28185	2.2±0.2	31.77±1.68	58.38±4.88	5.7	1.0±0.007
HD28254	3.12±0.32	30.12±2.0	57.24±6.11	$1.16^{+0.1}_{-0.06}$	1.181±0.009
HD290327	1.09±0.09	30.43±1.19	59.82±4.37	$2.54^{+0.17}_{-0.14}$	0.871±0.003
HD30177	3.15±0.29	31.58±2.31	58.62±5.13	$8.07^{+0.12}_{-0.12}$	1.064±0.011
HD30177	3.15±0.29	31.58±2.31	58.62±5.13	$3.0^{+0.3}_{-0.3}$	1.064±0.011
HD30562	2.25±0.15	33.91±1.74	54.99±4.05	$1.29^{+0.08}_{-0.08}$	1.276±0.006
HD33142	1.62±0.17	29.46±2.24	58.61±5.76	$1.385^{+0.064}_{-0.064}$	1.422±0.009
HD38801	2.3±0.17	32.29±2.27	56.78±4.31	$10.13^{+0.23}_{-0.23}$	1.237±0.011
HD4313	1.75±0.15	28.62±2.77	59.13±5.11	$2.3^{+0.2}_{-0.2}$	1.543±0.01
HD47366	1.63±0.12	27.87±2.2	59.56±4.24	$1.75^{+0.2}_{-0.2}$	1.798±0.009
HD47366	1.63±0.12	27.87±2.2	59.56±4.24	$1.86^{+0.16}_{-0.16}$	1.798±0.009
HD48265	3.15±0.31	29.01±1.93	56.3±5.87	$1.16^{+0.38}_{-0.38}$	1.375±0.009
HD50499	2.82±0.28	33.08±1.51	58.18±5.68	$1.45^{+0.08}_{-0.08}$	1.265±0.009
HD50499	2.82±0.28	33.08±1.51	58.18±5.68	$2.93^{+0.73}_{-0.18}$	1.265±0.009
HD50554	1.3±0.09	33.21±2.42	57.22±4.16	5.16	1.077±0.005
HD52265	2.01±0.19	32.7±1.78	55.52±5.19	$1.21^{+0.05}_{-0.05}$	1.238±0.009
HD5319	1.79±0.15	26.36±2.37	59.28±4.83	1.94	1.416±0.009
HD5319	1.79±0.15	26.36±2.37	59.28±4.83	$1.15^{+0.08}_{-0.08}$	1.416±0.009
HD5583	1.24±0.08	19.44±1.57	66.61±3.22	$5.78^{+0.53}_{-0.53}$	1.896±0.01
HD5891	1.22±0.09	18.31±1.95	66.16±3.65	$7.6^{+0.4}_{-0.4}$	1.952±0.013
HD60532	1.1±0.08	32.61±2.49	59.39±4.03	$1.03^{+0.05}_{-0.05}$	1.513±0.007
HD60532	1.1±0.08	32.61±2.49	59.39±4.03	$2.46^{+0.09}_{-0.09}$	1.513±0.007
HD65216	0.97±0.06	32.29±1.14	61.83±2.82	$1.295^{+0.062}_{-0.062}$	0.878±0.003
HD65216	0.97±0.06	32.29±1.14	61.83±2.82	$2.03^{+0.11}_{-0.11}$	0.878±0.003
HD66428	2.46±0.22	30.39±1.91	56.92±5.16	$2.82^{+0.027}_{-0.027}$	1.058±0.008
HD6718	1.13±0.08	32.91±1.2	59.02±3.72	$1.56^{+0.11}_{-0.1}$	0.941±0.003
HD70642	1.89±0.15	32.29±1.43	55.26±4.62	2.0	0.995±0.007
HD72659	1.31±0.09	31.03±1.28	57.0±3.85	$3.15^{+0.14}_{-0.14}$	1.13±0.005
HD72892	1.94±0.2	31.32±1.73	58.13±5.71	$5.45^{+0.37}_{-0.37}$	1.028±0.007
HD73267	1.73±0.16	29.28±1.6	59.37±5.0	$3.06^{+0.07}_{-0.07}$	0.87±0.008
HD73526	2.43±0.14	29.17±1.71	53.67±3.67	$2.25^{+0.12}_{-0.12}$	1.136±0.005
HD73526	2.43±0.14	29.17±1.71	53.67±3.67	$2.25^{+0.13}_{-0.13}$	1.136±0.005
HD73534	2.17±0.28	28.01±2.94	56.55±6.92	1.15	1.15±0.013
HD75898	2.36±0.21	33.23±1.84	54.2±5.4	2.51	1.322±0.007
HD82943	2.22±0.15	33.8±1.27	56.94±3.88	4.8	1.154±0.008
HD82943	2.22±0.15	33.8±1.27	56.94±3.88	4.78	1.154±0.008

C. PLANETARY BUILDING BLOCKS

star	**Z** (%)	$\boldsymbol{f_{iron}}$ (%)	$\boldsymbol{w_f}$ (%)	$\boldsymbol{m\sin(i)}$ (M_{jup})	$\boldsymbol{M_\star}$ ($M\odot$)
HD86081	2.22±0.21	31.47±2.51	56.76±5.72	1.5	1.286±0.008
HD89307	1.07±0.09	33.18±1.23	58.55±4.34	$2.0^{+0.4}_{-0.4}$	1.009±0.004
HD9174	3.13±0.29	31.06±1.95	58.7±5.09	$1.11^{+0.14}_{-0.14}$	1.218±0.012
HD92788	2.38±0.18	31.8±1.77	55.64±4.61	$3.76^{+0.16}_{-0.16}$	1.07±0.008
HD92788	2.38±0.18	31.8±1.77	55.64±4.61	$3.76^{+0.16}_{-0.16}$	1.07±0.008
HD98649	1.22±0.07	33.0±1.79	58.25±3.41	$6.79^{+0.5}_{-0.3}$	0.94±0.003
HIP63242	1.35±0.09	18.56±1.65	63.96±3.74	9.18	1.974±0.013
HR810	1.89±0.22	33.84±4.68	55.94±7.81	$2.26^{+0.18}_{-0.18}$	1.197±0.009
kappaCrB	2.01±0.21	28.08±2.42	58.23±6.22	1.6	1.507±0.012
KELT-6	0.89±0.11	32.74±4.74	62.51±6.3	$3.71^{+0.21}_{-0.21}$	1.221±0.008
muAra	2.38±0.16	32.81±1.69	53.25±4.34	1.676	1.155±0.008
muAra	2.38±0.16	32.81±1.69	53.25±4.34	1.814	1.155±0.008
piMen	1.55±0.14	33.25±1.17	56.77±5.26	$10.02^{+0.15}_{-0.15}$	1.101±0.005
TYC+1422-614-1	1.45±0.14	26.94±2.88	59.53±5.51	$2.51^{+0.12}_{-0.12}$	2.025±0.021
TYC+1422-614-1	1.45±0.14	26.94±2.88	59.53±5.51	$10.1^{+0.14}_{-0.14}$	2.025±0.021
upsAnd	1.76±0.19	33.02±4.78	57.82±6.24	$1.8^{+0.26}_{-0.26}$	1.343±0.007
upsAnd	1.76±0.19	33.02±4.78	57.82±6.24	10.19	1.343±0.007
upsAnd	1.76±0.19	33.02±4.78	57.82±6.24	$1.059^{+0.028}_{-0.028}$	1.343±0.007
WASP-41	1.39±0.12	33.89±1.91	55.53±5.16	$3.18^{+0.2}_{-0.2}$	0.889±0.004

Table C.1: Table with the iron-to-silicate mass fraction - f_{iron}, the water mass fraction - w_f and the summed mass percentage of all heavy elements expected for the planetary building blocks - Z for the sample stars.